An Electromagnetic Model for Thermal Emission

Characterization of Thermal Radiation from Ohmic Media

by

Yanwen Chen

to obtain the degree of Master of Science
at the Delft University of Technology,
to be defended publicly on Thursday August 24, 2023 at 13:30.

Student number:	5477018	
Project duration:	September, 2022 – August, 2023	
Thesis committee:	Prof. dr. A. Neto,	TU Delft (THz Sensing), supervisor
	Dr. ir. B. J. Kooij,	TU Delft (MS3)
	Dr. J. Bueno,	TU Delft (THz Sensing & ELCA)

Preface

A rigorous model based on classic electromagnetism to characterize the thermal radiation of real ohmic media is presented in this thesis. This model explains the available energy due to thermal agitation inside ohmic material based on Johnson's theory of thermal noise in electric circuits. The field is expanded in a finite number of modes (degrees of freedom per unit of volume), which are all independent and orthogonal from each other and are eigenvectors of Maxwell's Equations. The minimum distance for two eigenvectors to be independent is found as $\lambda_\beta/2$ (where λ_β is the real effective wavelength in the medium), based on which an analytical expression of the total energy available by thermal agitation in the finite volume is given. Integrating Poynting vectors of sources over the entire object volume, an analytical expression to estimate the total spectral power radiated out by a real ohmic material body is derived, which does not utilize Planck's law of black body radiation as an intermediary. Finally, a measurement campaign is proposed aiming at providing accurate measurements of the thermal radiation from silicon samples of small dimensions in the mm and sub-mm wave range.

Acknowledgment

First and foremost, I would like to express my gratitude to my supervisor, prof.dr. Andrea Neto. Andrea, it is your enthusiasm for electromagnetism that encouraged me to take all the TeraHertz Sensing courses in the first place. Throughout this project, you have unveiled the beauty of electromagnetism for me, which is usually buried under cumbersome mathematics and abstract ideas. I really learned a lot working with you.

I would also like to thank dr.ir. Bert Jan Kooij and dr. Juan Bueno for being my thesis committee member. For Juan, I really appreciate your guidance and help regarding all the lab work. It is really a pleasure to work with you.

I would like to thank all my colleagues in the TeraHertz Sensing Group. You guys have really created a cozy working atmosphere. Every lunch, coffee chat, birthday cake, Friday drink and group event is memorable. Academic people can also be super fun.

For all my friends, whether back in China or here in Europe, thank you all for bringing me countless confidence and joy through this two-year journey. I do not have a lot of friends, but each one of you is whom I can have deep conversations with.

Finally, huge thanks to my parents, who always supported me, both mentally and financially. I would not be who I am today without you.

Yanwen Chen
陈彦文
Den Haag, The Netherlands
August 2023

P.S. Special acknowledgements to Rotterdams Philharmonisch Orkest who offered top-level classical music performances at a really affordable price. Workdays just fly when a Friday evening concert is added to my agenda.

Contents

1

Introduction

1.1. Background

The universal absorption of solar energy, whether through natural processes like photosynthesis or artificial systems like photovoltaics, is undeniably one of the fundamental elements for the very existence of our human civilization. The absorbed electromagnetic (EM) energy by a certain medium, in the absence of other mechanisms, is then transformed into thermal energy, resulting in the rising of the temperature of the medium. The mechanism of thermal emission, on the other hand, indicates the radiating EM energy from the medium to counteract the continuous energy absorption[1]. This energy radiation is also universal, from the thermal noises in electronic systems to the intensifying global warming. Radiometry is a field of science and engineering focused on modelling and measuring this type of energy thermally radiated by material bodies.

The theoretical foundation of thermal radiation dates back to 1860, when Kirchhoff first established the famous Kirchhoff's law of thermal radiation [2], claiming the equality of absorptivity and emissivity of material bodies under thermal equilibrium. He also proposed the idea of the black body, which is an ideal body that absorbs all the EM radiation incident upon it. It is noteworthy that black bodies do not naturally exist and can only be artificially synthesised. Nonetheless, the idea of the black body has become an intermediate agent to characterize the emissivity of real bodies in this field of science ever since. Decades later, based on thermodynamics and statistical physics, i.e. equipartition theorem, the empirically derived Rayleigh-Jeans [3], [4] law was established around the 1900s to describe the spectral radiation of the black body. However, this model had a lethal problem in that the brightness it predicted kept rising with respect to frequency, which contradicted the energy conservation law. Also, with the development of instrumentation, Rayleigh-Jeans law failed to predict the experimental results of radiation of the artificially engineered black bodies at high frequency, leading to the ultraviolet catastrophe. Groundbreakingly, Planck [5] solved this crisis by establishing the famous Planck's law of radiation. The brightness of black bodies predicted by Planck's law is shown in Figure 1.1 for various temperatures. Instead of treating the EM radiation as a continuous quantity from a classic point of view, he heuristically assumed that EM energy can be radiated in a discrete way. These discrete packets of energy, called *quanta* by Planck and later *photons* by Einstein [6], set the very basis for today's soaring skyscraper of quantum physics.

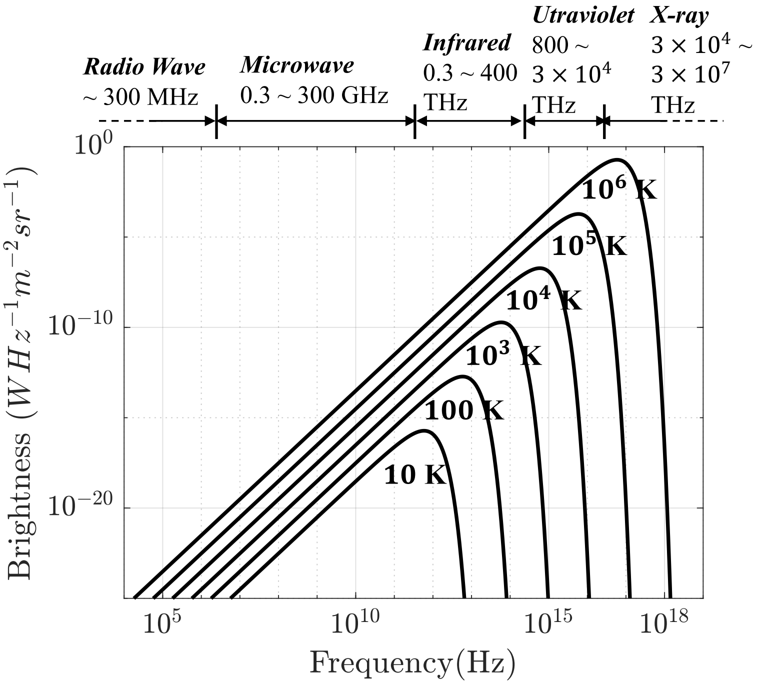

Figure 1.1: Planck's law of black body brightness at different temperatures.

In 1928, Johnson [7] successfully characterised the thermal noises in electrical circuits caused by the thermal agitation of charge carriers. His colleague Nyquist [8] demonstrated Jonson's discovery in a theoretical way, which was later called Fluctuation Dissipation Theorem (FDT). Without any EM argument or experimental results, Nyquist replaced the classically derived average energy of one degree of freedom with a quantum correction term. This noise model is generally referred to as the Johnson-Nyquist noise nowadays and is widely used by the microwave community.

The relationship between classic Maxwell's equations and quantum field theory has kept puzzling electrical engineers. The first and most widely accepted tool to connect the two fields is represented by Rytov's current model. Based on Nyquist's model, Rytov [9] in 1953 first tried to model thermal radiation from an emissive perspective. He proposed a hybrid classic-quantum model, computing the thermal radiation by solving Maxwell's equations with a set of impressed current sources which are forced by a quantum oscillator (same as Nyquist's correction term). However, by taking a closer look, there are two problems with Rytov's currents. On one side, the demonstration of this hybrid model [10] presents some mathematical criticalities. On the other side, the entire procedure is much less experimentally verified than one would think [11], given how long it has been accepted. Some of these aspects will be discussed in detail in Section 2.3. Another important drawback of Rytov's currents is that it was not clear how to mathematically implement them in a simulation tool. [12] is possibly the only numerical attempt at calculating the radiation directly from Rytov's currents, but without presenting any experimental verification. Indeed, the majority of work regarding emissivity in the radiometry community is achieved by evaluating absorptivity, which is equal to emissivity after the establishment of thermal equilibrium according to generalized Kirchhoff's law [10].

1.2. Motivation

Thermal noise has long been impacting the electrical engineering community, since it is often the dominant term in the signal-to-noise ratio of communication and sensing systems. With the trend in the industry going towards higher and higher frequencies due to the scarcity of spectrum resources, there is an interest in figuring out if the thermal radiation remains well represented by Planck's law or Rytov's currents in the THz bands. This is important especially because of the near availability of very sensitive, thousands of pixels thermal cameras in the THz range [13]–[15] that will fulfil the requirements of passive imaging. However, the availability of such cameras does not correspond to a wealth of information about the thermal radiation from known real material bodies kept at certain temperatures. Actually, there are no measurements of thermal radiation from known materials at known temperatures in the sub-THz frequency range. As [11](page 1) suggests the only strong evidence of Plank's law in the mm-wave range is from the satellite-based campaign, to investigate cosmic background [16]. However, by definition, we do not know what is the radiation source of the cosmic background.

Another specific issue of interest to microelectronic engineers is the Drude model's impacts on the conductivities of semi-conductors, rendering their imaginary part non-negligible already in the sub-THz range [17], where the advanced front-ends for communications and sensing are being developed. However, the impact of the Drude model on thermal radiation has not been investigated in the literature. It is our conviction that including the frequency-dependent properties of the Drude model for the conductivity of the radiating materials will provide a decrease of the radiated spectral energy at frequencies above the inverse of the scattering time of the free electrons. It is worth noticing that this is not an exotic far-fetched phenomenon, but depending on the doping levels of the materials, this frequency transition could already be occurring at 100 GHz.

Motivated by the lack of experimental evidence of thermal radiation and the prospects of identifying a big role for Drude-like dispersion characteristics, this thesis aims to model the thermal radiation of real material bodies electromagnetically in a rigorous way. The model should be purely based on classic EM theory so that its consequences and terminologies can be well-understood by electric engineers. Thermal radiation energy predicted by this model should directly come from the characteristics of the ohmic material of the real body, without the need of introducing black bodies as an intermediary reference. After the establishment of the model, a measurement campaign should also be proposed in order to fill the blank of thermal radiated power by real bodies at certain temperatures and frequency bands, as well as to test the validity of our model.

1.3. Outline of the Thesis

The main part of this thesis is divided into seven chapters.

Some fundamental concepts of modern radiometry are explained in Chapter 2. First, some radiometric quantities are introduced. Then, the hybrid classic-quantum model developed by Rytov is presented in Section 2.2. Some of its inherent problems are then discussed. Some works regarding coherence theory and radiometry are introduced in Section 2.4, pointing out that the general assumption of incoherent sources of radiometry is not always true.

Next, Drude model is explained in Chapter 3 as a tool to characterize the behaviour of plane waves interacting with ohmic media. Then, Johson-Nyquist noise caused by thermally agitated electrons in electrical circuits is explained. A Norton-type and a Thevenin-type equivalent circuit are presented and analysed.

In Chapter 4, our EM model to characterize the thermal radiation of real ohmic media is proposed. Degrees of freedom in the EM field, each being the eigenvectors of Maxwell's equation and orthogonal to each other, comprise the total EM field in the emissive body. The eigenvectors and their corresponding eigen-currents are given in an explicit way. The total number of degrees of freedom inside a certain volume is given in Section 4.3. A Johnson-like circuit is established in Section 4.4 to estimate the amount of energy each of the degrees of freedom can deliver.

In the proceeding Chapter 5, two important issues are resolved. Self-impedance of the eigenvector is derived analytically to serve as internal impedance and the load in the Johnson-like circuit. Then, the mutual impedance of two eigenvectors is also asymptotically derived. The minimum distance for two eigenvectors to be uncoupled is found. Based on these two findings, the total energy available within the medium is expressed analytically in Section 5.3.

Subsequently, by calculating the Poynting vectors from every independent generating source, Chapter 6 addresses the power that actually leaves the radiating body. An analytical expression is derived and verified by numerical results as a quick tool to estimate the spectral power radiated by a real finite ohmic body.

Based on the model introduced in previous chapters, Chapter 7 proposed an experiment campaign to accurately measure the radiated power from real material bodies in the mm and sub-mm wave range. The material selection process is introduced in Section 7.1 along with its characterization process in Section 7.2. The detectors are then introduced in Section 7.3. A cavity on the waveguide short is designed to host the measurement samples. Finally, possible measurement set-ups are described in Section 7.6.

Chapter 8 concludes the work of this thesis and discusses possible future works on this project.

This thesis is supplemented by several appendices to provide some additional information regarding each topic.

2

Basics of Radiometry

Radiometry is a school of science intended to measure incoherent radiant EM energy from all kinds of media [1]. Some basic knowledge of radiometry is introduced and explained in this chapter. Section 2.1 first introduces some basic radiometric quantities, including brightness, radiation intensity, absorptivity and emissivity. Then, a hybrid classic-quantum model proposed by Rytov in 1953 [9] explaining the thermal radiation from material objects is presented in Section 2.2. This model proposed a set of current basis that can be used as current sources in Maxwell's equations. Based on this model, Kirchhoff's radiation law can also be generalized, which allows scientists ever since to study the emission of thermal energy in a reciprocal way: from energy absorption. Using this reciprocity, the total power radiated by a bulk object over a certain bandwidth can be calculated. However, Rytov's current falls on several problems, some of which are quite fundamental, as explained in Section 2.3. Finally, Section 2.4 presents some work on the coherence of the field in thermal radiating sources, which are traditionally considered as incoherent.

2.1. Radiometric Quantities

A basic quantity in radiometry is *brightness* $B(\Omega, A)$, also known as *radiance*, which represents the radiated power per unit solid angle per unit area ($W sr^{-1} m^{-2}$ for example). It is calculated from dividing the *radiation intensity* $I(\Omega)$ (radiated power per unit solid angle) by the effective area of the source normal to the radiation. In intensity $I(\Omega)$, the sources are treated as point sources [1]. Brightness provides us with a tool to describe the radiation from an extended incoherent source, which is a common assumption for sources in radiometric applications.

Absorptivity a_{bs} is defined as the ratio of the power absorbed by the entire volume of the object and the total power going through the surface of the object. Ideally, the absorptivity of a black body is 1, which means all the power impinging on it will be absorbed. According to Kirchhoff's law of thermal radiation [2], absorptivity a_{bs} is equal to *emissivity* e_{msi} after the establishment of thermal equilibrium. Emissivity reflects how much energy is radiated by a real body with respect to the black body under the same temperature:

$$e_{msi}(T) = \frac{B(T)}{B_{BB}(T)}, \tag{2.1}$$

where $B(T)$ represents the brightness of the real body, $B_{BB}(T)$ represents the brightness of the black body, both under the same temperature T. The spectral brightness of the black body, considering two polarizations, is given by Planck [5] as:

$$B_{BB}^{Plk}\left(f,T\right)=\frac{2hf^3}{c_0^2}\frac{1}{e^{\frac{hf}{k_BT}}-1}, \tag{2.2}$$

where k_B is the Boltzmann constant ($1.38\times10^{-23}J\cdot K^{-1}$), T is the temperature in Kalvin, h is Planck constant ($6.626\times10^{-34}J\cdot Hz^{-1}$), hf indicates the energy of single photon at frequency f, and c_0 is the propagation speed in free space. At low frequencies, this brightness can be approximated by Rayleigh-Jeans [3], [4] Law:

$$B_{BB}^{RJ}\left(f,T\right)=\frac{2k_BTf^2}{c_0^2}. \tag{2.3}$$

2.2. The Hybrid Classic-Quantum Model

Rytov [9] in 1953 first extend the Johnson-Nyquist noise model (which will be explained in detail in Section 3.2) to the thermal radiation of large dissipative systems. He proposed a set of current densities that can be used as impressed current in Maxwell's equations. This is given by the conjugate correlation function of one elementary current density $\vec{J}_R\left(\vec{r}_i\right)$ and its neighbouring element $\vec{J}_R\left(\vec{r}_j\right)$:

$$<\vec{J}_R\left(\vec{r}_i\right),\vec{J}_R^*\left(\vec{r}_j\right)>=\frac{4hf}{e^{\frac{hf}{k_BT}}-1}Re\{\sigma\}\delta\left(\vec{r}_i-\vec{r}_j\right). \tag{2.4}$$

Notice that the frequency-dependent term $4hf/(e^{\frac{hf}{k_BT}}-1)$ is inherited from the quantum correction of the noise model proposed by Nyquist [8]. In (2.4), σ represents the complex conductivity of the medium hosting these currents (see (3.3)). Here, only the real part of σ is considered. $\delta\left(\vec{r}_i-\vec{r}_j\right)$ indicates the orthogonality of these current. In other words, the cross-correlation between any two of these neighbouring elementary currents is always zero, no matter how they are close to each other physically. The problem of this counter-intuitive postulation will be analysed in the next section.

Based on the proposed current (2.4), Rytov also generalized [9], [10], [18], [19] the Kirchhoff's law, stating that the local absorptivity and emissivity is equal after the establishment of thermal equilibrium. The absorptivity per unit of solid angle Ω and per frequency can be written as:

$$a_{bs}\left(\Omega,f\right)=\frac{P_{abs}\left(\Omega,f,\ Volume\right)}{P_{in}\left(\Omega,\ f,\ Area\right)}, \tag{2.5}$$

with $P_{in}\left(\Omega,f,Area\right)$ indicates the power going through the surface area of the object and $P_{abs}\left(\Omega,f,\ Volume\right)$ indicates the power absorbed by the volume of the object, per unit of solid angle Ω and per frequency. Based on generalized Kirchhoff's law, we can have $a_{bs}\left(\Omega,f\right)=e_{mis}\left(\Omega,f\right)$, as shown in Figure 2.1.

Bekefi [20] first introduced Rytov's work to the Western scientific community in a clear manner. He pointed out that, although in theory using Rytov's current and Maxwell's equations, together with appropriate boundary conditions applied on the surface of the object, leads to a complete solution of the thermal emission of the object by calculating all the Poynting vectors, the calculation itself is rather cumbersome for that one should sum up the contributions from all the elementary currents. Bekefi suggested using the absorptivity

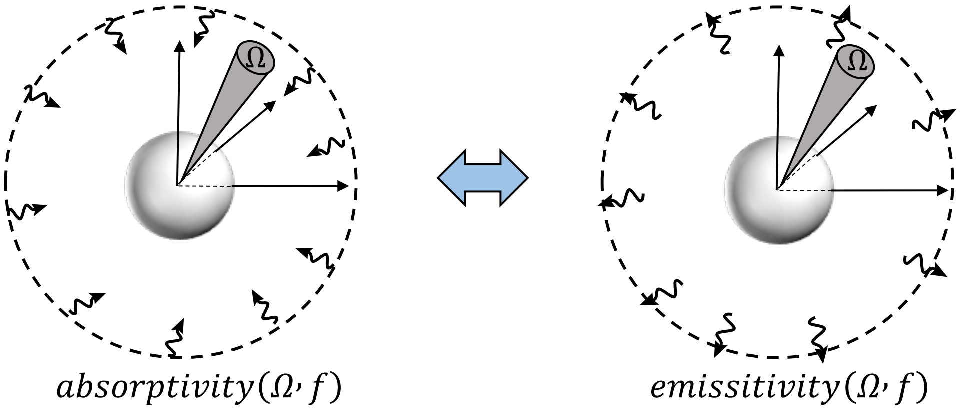

Figure 2.1: Generalized Kirchhoff's law: Reciprocity between local absorptivity and emissivity.

of the object to calculate the emissivity, which is the reciprocity property given by generalized Kirchhoff's law. Using spectral brightness given by Planck in (2.2), the spectral power radiated by material objects can be written analytically as:

$$P_{Plk}(f) = \frac{hf^3}{c_0^2} \frac{1}{e^{\frac{hf}{k_B T}} - 1} \left[1 - |\Gamma|^2\right] \left[1 - e^{-2k_\alpha L}\right] \cdot SA, \tag{2.6}$$

where L represents the total path the Poynting vector traversed in the object, $|\Gamma|^2$ refers to the power reflection coefficient, k_α is the imaginary part of the propagation constant (see (3.11)), and SA refers to the surface area of the radiating object. Then the power radiated over a certain bandwidth BW can be represented as:

$$P = \left[1 - |\Gamma|^2\right] \left[1 - e^{-2k_\alpha L}\right] \cdot SA \int_{BW} \frac{hf^3}{c_0^2} \frac{1}{e^{\frac{hf}{k_B T}} - 1} df. \tag{2.7}$$

The details of this derivation process are given in Appendix A.

2.3. The Problems of Rytov's Current

Thanks to the reciprocity between the absorptivity and emissivity given by generalized Kirchhoff's law, scientists over the years, to name a few [21]–[23], have bypassed the problem caused by Rytov's ill-posted currents. Only recently, [12] has attempted to use Rytov's current in emission mode to evaluate the power radiated outside an ideal silicon cube, with a relative permittivity of $\varepsilon_r = (12 - j)$ and no dispersion. The result was later verified in our group [24] using the tool of volumetric method of moments [25]. In [12], the finite body (the bulk cube with side length L) has been discretized into N small cubes, each with side length Δ, as shown in Figure 2.2. Rytov's current is flowing volumetrically over the entire small cube. The total current inside the body can be represented by the summation of all volumetric currents as:

$$\vec{J}_{R_{tot}}(\vec{r}) = \lim_{\Delta \to 0} \sum_{i=1}^{N} I_R^i \frac{1}{\Delta^2}\, rect\left(\vec{r} - \vec{r}_i, \Delta^3\right) \hat{p}_i, \tag{2.8}$$

where the current amplitude I_R^i is expressed as:

$$I_R^i = \sqrt{\frac{4hf}{e^{\frac{hf}{k_B T}} - 1} Re\{\sigma\} \Delta e^{j\phi_i}}. \tag{2.9}$$

This volumetric current is essentially the same as the elementary current given in (2.4) and also obeys the orthogonality proposed by Rytov [10], i.e. each of the elementary volumetric currents is uncoupled from its neighbouring element. $\hat{p}_i$ in (2.8) represents the polarization of the current and $\vec{r}_i$ represent the centre of the i^{th} elementary cube. The term $\frac{1}{\Delta^2}$ is to compensate for the 3D volumetric distribution of $rect\left(\vec{r}-\vec{r}_i,\Delta^3\right)$, to ensure the unity of the current amplitude I_R^i. $Re\{\sigma\}$ in (2.9) can also be represented by the frequency-dependent conductivity of Drude's model, which will be introduced in Chapter 3. Notice that the phase term $e^{j\phi_i}$ in (2.9) can be considered as random, consistent with the assumption of orthogonality and can be summed up when we consider the energy it radiates out. However, as suggested by the limitation $\Delta \to 0$, the side length Δ of the elementary cube can be infinitesimally small. This essentially means that an *infinite* number of elementary currents can exist in a finite object. In this way, the amount of energy inside the object is then infinite, which, of course, contradicts the energy conservation law. Rytov[10], along with fellow Soviet scientists like Landau[18], was aware of this problem, arguing that the model is still valid as long as the radiated power is calculated outside the object from a macroscopic sense.

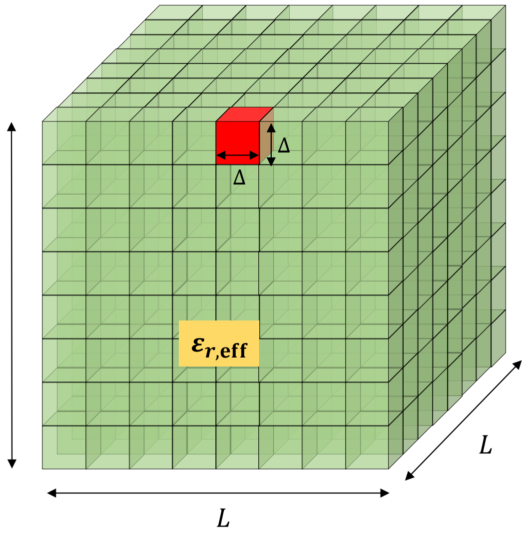

Figure 2.2: Discretization of a bulk object from Rytov's current.

As mentioned before, the correlation in Rytov's current (2.4) only exists when two element coincide, $\vec{r}_i = \vec{r}_j$. To prove this, Rytov gave a demonstration in his 1989 book [10] by proposing a set of orthogonal basis functions $\phi_j^R(\vec{r})$, which is uncorrelated to each other and should be the solution of Maxwell's equations. He used this set of functions to expand the field as (eq.(3.12) of [10]):

$$e(\vec{r}) = \sum_j^{\infty} \alpha_j(f,\vec{r})\phi_j^R(\vec{r}), \tag{2.10}$$

where $\alpha_j\left(f,\vec{r}\right)$ is an infinite set of the expansion coefficients applied to the orthogonal basis functions $\phi_j^R(\vec{r})$. This essentially represents the field by an infinite superstition of modal functions. Then Rytov shows that the cross conjugate correlation of two field positions $\vec{r}$

and $\vec{r}'$ could be represented as (eq.(3.19) of [10]):

$$< e(\vec{r}), e^*\left(\vec{r}'\right) > \propto \sum_j^{\infty} \phi_j^R(\vec{r}) \phi_j^R\left(\vec{r}'\right) \propto \delta\left(\vec{r}-\vec{r}'\right), \tag{2.11}$$

using properties of the orthonormal modal expansions. However, Rytov failed to give the exact form of these modal functions, simply suggesting their existence. However, their existence is highly arguable [26].

Furthermore, as inherited from Nyquist's correction of Johnson's current in FDT, the Plank-like frequency dependence term in Rytov's current (2.9) also lacks EM arguments.

2.4. Coherence and Radiometry

The fairly puzzling relationship between classic radiometry theory (i.e. the EM theory based on Maxwell's equations) and modern theories of radiation (Planck's radiation law and quantum radiation theory) had induced some critics by scientists [27], pointing out that the energy transfer mechanism within the thermal radiative body remains an open question. Wolf [27] tried to connect classic radiometry with the coherence theory of physical optics, in order to see to what extent can traditional radiometry concepts and laws, which are based on the assumption of incoherence of the thermal sources, can be applied to highly coherent optic sources such as lasers.

In [27], Wolf pointed out that for a planar Lambertian source, which is typically regarded as spatially incoherent (see Appendix A), the spectral degree of spatial coherence for two points $\vec{r}_1$ and $\vec{r}_2$ of the field in the source plane can be expressed as a *sinc* function, if the non-radiating (reactive) part is ignored, as:

$$\rho\left(\vec{r}'\right) = \frac{\sin\left(k\left|\vec{r}'\right|\right)}{k\left|\vec{r}'\right|} = \operatorname{sinc}\left(k\left|\vec{r}'\right|\right), \tag{2.12}$$

where k is the propagation constant and $\vec{r}' = \vec{r}_1 - \vec{r}_2$. This spatial coherence function is defined as the conjugate spatial correlation of the electric (or magnetic) field in the aforementioned two points normalized by the average intensity at these two points as [27], [28]:

$$\rho\left(\vec{r}'\right) = \frac{< \vec{E}(\vec{r}_1), \vec{E}^*(\vec{r}_2) >}{\sqrt{I(\vec{r}_1)\, I(\vec{r}_2)}}, \tag{2.13}$$

where $< \vec{E}(\vec{r}_1), \vec{E}^*(\vec{r}_2) >$ denotes the spatial correlation and $I(\vec{r})$ denotes the intensity distribution across the planar source. As we can see from (2.12) that Lambertian sources are not completely spatially incoherent as assumed by classic radiometry, but rather correlated as suggested by the *sinc* function over the distance in terms of wavelength λ within the medium. Only when $\left|\vec{r}'\right| = n\frac{\lambda}{2}$, where n is a positive integer, the two points $\vec{r}_1$ and $\vec{r}_2$ are then uncorrelated. The *sinc* relation is in agreement with correlation properties of black body radiation [28]. Similar results of this *sinc* relation can also be seen in EM compatibility theories to describe the correlation of the field in a reverberation chamber [29], [30].

It is worth noticing that the field correlation (coherence) mentioned above is derived outside the source region, assuming a plane wave expansion of the field.

3

The Medium and the Thermal Noise

From a classic point of view, the thermal radiation of an ohmic medium comes from the agitation of electrons by heat, which causes a fluctuation of electric charges [8]. In order to study this thermal radiation, one fundamental thing is to have knowledge of the EM characteristics of this medium, e.g. conductivity and permittivity. At high frequencies, the traditional quasi-static model for conductivity is not accurate anymore due to the lack of frequency dependence. In this chapter, Drude model [31], a classic EM model used for material characterization, is introduced in Section 3.1, which will be used throughout this thesis.

The fluctuation dissipation theorem (FDT) is then introduced in Section 3.2 to calculate the observed current generated by thermal agitation of electric charges in conductors. Instead of tracking the behaviour of each microscopic particle, this theorem provides us with a method to analyse the thermal noise in electric circuits from a macroscopic point of view.

3.1. Drude Model

Drude Model [17], [31] is a classic EM model to characterize the behaviour of plane waves interacting with ohmic media. It describes the interactions between electrons and ions with the presence of an external electric field. In Drude model, the conductive behaviour of the material is frequency dependent. This frequency dependence is modelled via the electrons in the material body, which are treated as classical point charges, accelerated by the presence of an electric field and randomly hitting ions which, being much heavier than electrons, can be assumed as stand still, as shown in Figure 3.1. Kinetic energy is then transferred from the jittering electrons to the ions, which then creates heat. To characterize this phenomenon, τ is defined as the average time between two consecutive hits, which is called the scattering time. This is an intrinsic property of the material and is not subjected to change by the variation of the external electric field.

The classical quasi-static limit of the conductivity relates the electric field $\vec{E}(\omega)$ and electric current density $\vec{J}(\omega)$ at low frequencies as:

$$\lim_{\omega\to 0}\frac{\left|\vec{J}(\omega)\right|}{\left|\vec{E}(\omega)\right|}=\sigma_{qs}. \tag{3.1}$$

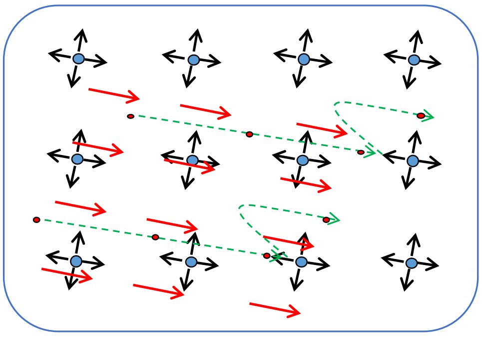

Figure 3.1: Kinetic energy is transferred from the accelerated electrons to the ions, which then creates heat.

This quasi-static limit can be represented as:

$$\sigma_{qs} = \frac{ne^2\tau}{m_e}, \tag{3.2}$$

where $m_e = 9.1 \ \times 10^{-31}\ kg$ is the mass of an electron, $e = 1.6 \times 10^{-19}\ C$ is the charge of an electron and n is the number of free electrons per cubic meter in the material.

Drude upgraded this quasi-static model to include frequency dependencies. In Drude model, the frequency-dependent conductivity is given as:

$$\sigma(\omega) = \frac{\sigma_{qs}}{1 + j\omega\tau} = \frac{\sigma_{qs}}{1+\omega^2\tau^2} - j\frac{\sigma_{qs}\omega\tau}{1+\omega^2\tau^2}, \tag{3.3}$$

where ω is the angular frequency. Hence, the frequency-dependent resistivity is:

$$\rho(\omega) = \frac{1}{\sigma(\omega)}. \tag{3.4}$$

To define the permittivity of the material, we can start from Maxwell's equations, which in frequency domain [32] can be written as:

$$\nabla \times \vec{E}(\omega) = -j\omega\mu\vec{H}(\omega) - \vec{M}(\omega), \tag{3.5a}$$

$$\nabla \times \vec{H}(\omega) = j\omega\varepsilon\vec{E}(\omega) + \vec{J}(\omega), \tag{3.5b}$$

$$\nabla \cdot \vec{E}(\omega) = \frac{\rho_e(\omega)}{\varepsilon}, \tag{3.5c}$$

$$\nabla \cdot \vec{H}(\omega) = \frac{\rho_m(\omega)}{\mu}, \tag{3.5d}$$

where $\vec{E}(\omega)$ and $\vec{H}(\omega)$ are the frequency domain electric and magnetic field, $\vec{J}(\omega)$ and $\vec{M}(\omega)$ are electric and magnetic current sources, ε and μ are the permittivity and permeability of the medium, and $\rho_e(\omega)$ and $\rho_m(\omega)$ are the electric and magnetic charge densities, respectively. Notice that $\vec{J}(\omega)$ and $\vec{M}(\omega)$ in (3.5) are current densities with units A/m^2 and V/m^2. In an ideal lossless medium, the permittivity ε is purely real. While a real lossy medium has a complex permittivity, $\varepsilon = \left(\varepsilon' - j\varepsilon''\right)$, where the imaginary part accounts for the losses in the medium. The imaginary part of the permittivity should always be negative to guarantee energy conservation. This loss in the dielectric medium can also be considered as an equivalent conductor loss, and can be represented by Ohm's law:

$$\vec{J}(\omega) = \sigma(\omega)\vec{E}(\omega). \tag{3.6}$$

In the absence of sources or out of the source region, $\vec{J}(\omega)$ in (3.5b) can be replaced by (3.6):

$$\nabla \times \vec{H}(\omega) = j\omega\varepsilon\vec{E}(\omega) + \sigma(\omega)\vec{E}(\omega) = j\omega\left(\varepsilon - \frac{j\sigma(\omega)}{\omega}\right)\vec{E}(\omega) = j\omega\varepsilon_{eff}(\omega)\vec{E}(\omega). \tag{3.7}$$

From (3.7), the effective permittivity of the material can be represented as:

$$\varepsilon_{eff}(\omega) = \left(\varepsilon - \frac{j\sigma(\omega)}{\omega}\right) = \varepsilon_0\varepsilon_{r,eff} = \varepsilon_0\varepsilon_{r\infty}\left(1 - \frac{j\sigma(\omega)}{\omega\varepsilon_0\varepsilon_{r\infty}}\right), \tag{3.8}$$

where $\varepsilon_0 = 8.854 \times 10^{-12}\ F/m$ is the permittivity constant in free space and $\varepsilon_{r\infty}$ is the relative permittivity saturation of the material at a very high frequency. The characteristic impedance and the propagation constant can then be expressed as:

$$\zeta(\omega) = \frac{\zeta_0}{\sqrt{\varepsilon_{r,eff}(\omega)}}, \tag{3.9}$$

$$k(\omega) = k_0\sqrt{\varepsilon_{r,eff}(\omega)}. \tag{3.10}$$

Notice that we can express the complex propagation constant k with its real and imaginary part as:

$$k = k_\beta - jk_\alpha. \tag{3.11}$$

There are two noteworthy frequencies in this frequency-dependent model. One is the transitional frequency:

$$\omega_\tau = \frac{1}{\tau}, \tag{3.12}$$

which depends on the scattering time τ. At this frequency, the real and imaginary part of the resistivity are the same. After this frequency point, the imaginary part becomes dominant. This means that now the scattering time τ is longer than the period of which the electric field changes sign. Under this circumstance the electrons are forced to change sign with the electric field before reaching to the ions, thus causing the free electrons to keep oscillating, as shown in Figure 3.2, and not to transfer their kinetic energy to the ions.

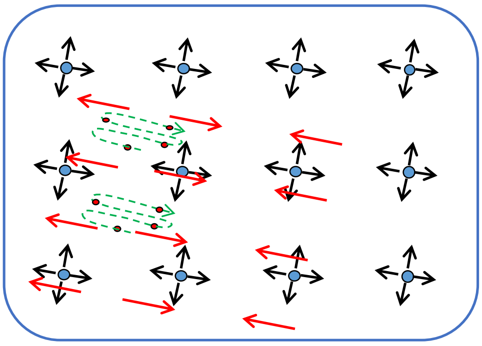

Figure 3.2: Electrons are forced to change sign with the electric field before reaching to the ions, thus causing the free electrons to keep oscillating.

Another frequency of interest is the plasma frequency, which corresponds to the plasma oscillations:

$$\omega_p = \sqrt{\frac{ne^2}{\varepsilon_{r\infty}\varepsilon_0 m_e}}. \tag{3.13}$$

After introducing the plasma frequency, we can then rewrite the effective permittivity (3.8) as:

$$\varepsilon_{r,eff}(\omega) = \varepsilon_{r\infty}\left[1-\omega_p^2\tau^2\left(\frac{1}{1+\omega^2\tau^2}\right)\right] - j\varepsilon_{r\infty}\omega_p^2\frac{\tau^2}{\tau\omega}\left(\frac{1}{1+\omega^2\tau^2}\right). \tag{3.14}$$

The plasma frequency is usually a lot higher than the transition frequency for metals. For frequencies lower than the plasma frequency, where $\omega_p^2\tau^2 > \omega^2\tau^2$, it is apparent that the real part of the effective permittivity is negative. The distance between each electron is small compared to the wavelength. As the frequency increases, the size of the electrons becomes larger compared with the wavelength. They thus become more reluctant to the change of the external field and radiate less scattered field. When the frequency is high enough, specifically after the plasma frequency, the medium begins to behave as "*transparent*" to the incoming wave, meaning that the wave can propagate through the material without any obstruction.

Using the representation of effective permittivity in (3.14), we can write characteristic impedance in (3.9) as:

$$\zeta(\omega) = e^{\frac{j\pi}{4}}\sqrt{\frac{\mu_0\omega}{\sigma_{qs}}}\sqrt{\frac{1+\omega^2\tau^2}{1+j\gamma(\omega)}}, \tag{3.15}$$

where we define the variable $\gamma(\omega)$ as:

$$\gamma(\omega) = \frac{\omega}{\omega_p^2\tau}\left(1+\left(\omega^2-\omega_p^2\right)\tau^2\right). \tag{3.16}$$

At low frequencies, (3.16) is negligible and can be viewed as 0. Then, the characteristic impedance is simplified as:

$$\zeta\left(\omega \ll \omega_p\right) = \sqrt{\frac{\mu_0\omega}{2\sigma_{qs}}}\left(1+j\right), \tag{3.17}$$

where the real and imaginary part are more or less the same. This corresponds to Leontovich [33] method, an approximation widely used in the microwave community for good conductors. For frequencies much higher than the plasma frequency, $\gamma(\omega)$ can be expressed as:

$$\gamma(\omega) = \frac{\omega}{\sigma_{qs}}\left(1+\omega^2\tau^2\right). \tag{3.18}$$

This results in the characteristic impedance to have an asymptotic behaviour as:

$$\zeta\left(\omega \gg \omega_p\right) = \sqrt{\frac{\mu_0}{\varepsilon_0\varepsilon_{r,\infty}}}. \tag{3.19}$$

3.1.1. Metal

Drude model accurately describes the dispersion of EM waves in materials with low resistivities [17], namely metals. To give a specific example, consider gold, whose electron density is $n = 5.9\times10^{28}$ electrons$/m^2$, and scattering time is $\tau = 27fs$. The relative permittivity at high frequency $\varepsilon_{r\infty}$ is 1 for gold. Using (3.12) and (3.13), the transition frequency is calculated as 5.89 THz, and the plasma frequency is around 2180 THz.

Figure 3.3 shows the resistivity of gold, with the transition frequency marked in a black dashed line. As we can see from the figure, it is clear that for the frequencies lower than

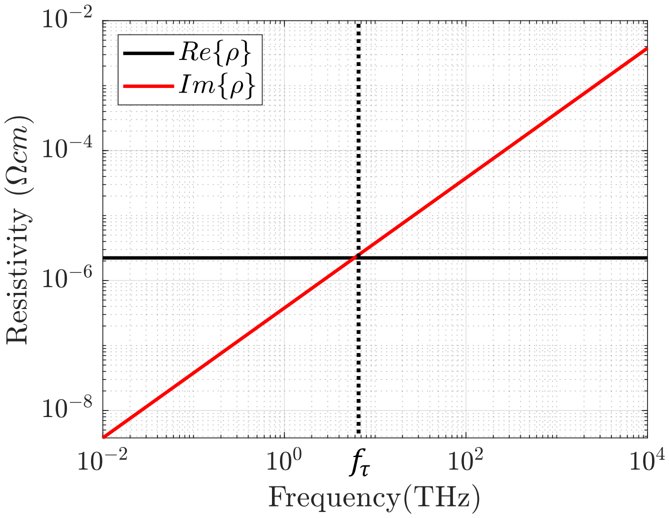

Figure 3.3: Frequency dependent resistivity of gold, with the transition frequency marked in black dashed line.

f_τ the imaginary part of resistivity is smaller than the real part. It continues to rise until intersecting with the real part at f_τ and becomes larger than the real part for frequencies higher than f_τ.

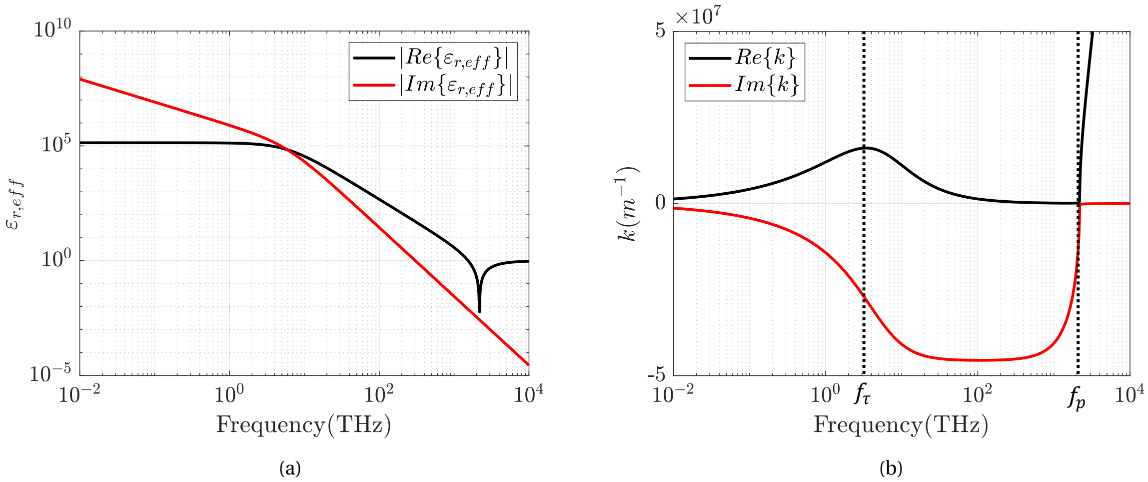

Figure 3.4: (a)The absolute value of the effective permittivity (b)The propagation constant

Figure 3.4 shows the absolute value of the effective permittivity and the propagation constant, with frequency in logarithmic scale. Two frequencies of interest: the transition frequency f_τ and the plasma frequency f_p, are marked in black dashed lines. The two frequencies can be clearly seen in the figure from the transition of the curves. As we can see from Figure 3.4b that for frequencies higher than f_p, the imaginary part of k is 0, which means the wave can propagate through the medium without any attenuation. The real part of the propagation constant continues to grow until f_τ. Between f_τ and f_p, when the electrons in the material are excited by the external wave, they also radiate a scattered field. This field is opposite to the direction of the external field, thus causing destructive effects on the propagation of the wave in the medium, similar to the scenario of waveguide cut-off

[17].

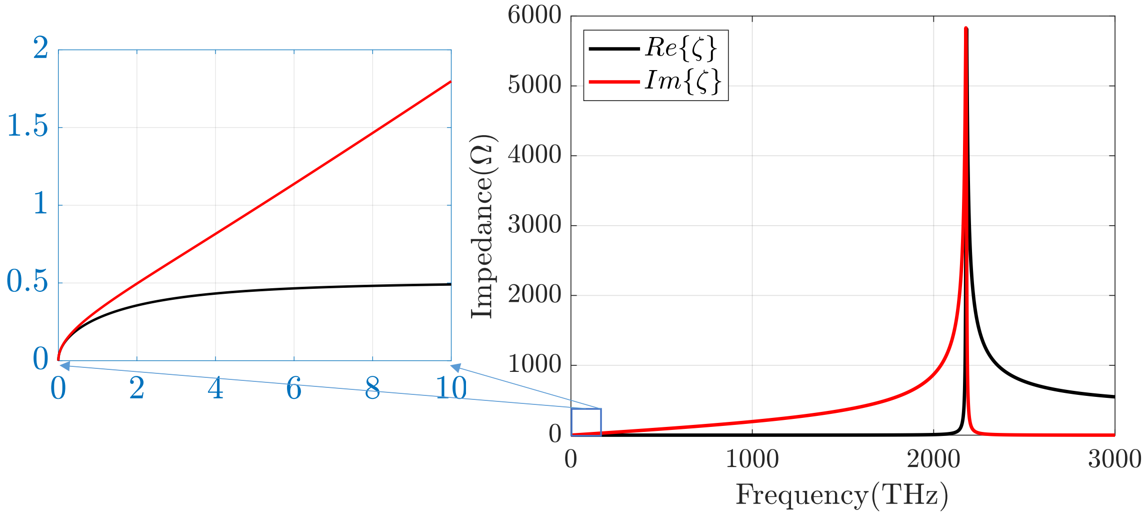

Figure 3.5: The characteristic impedance of gold, with low frequencies from 0 to 10 THz zoomed in in the left.

Figure 3.5 shows the characteristic impedance of gold, with low frequencies from 0 to 10 THz zoomed-in on the left. For frequencies higher than f_p, the characteristic impedance tends to be the free space impedance ζ_0, which corresponds to the fact that $\varepsilon_{r\infty}$ is 1 for gold. As it can be seen from the zoomed-in figure for low frequencies on the left, the real and imaginary part are the same for frequencies below 1 THz, which corresponds to the Lenotovich method introduced before.

The properties of the dispersion curves are highly dependent on the electron density n. Metals can be ground into powder to lower their electron density. Metallic powder, or bad metal (bad in terms of conductivity), is widely used in the microwave community to fabricate absorbers [34]. Consider a kind of gold powder to which Drude model can be applied. The electron density of the metallic powder is $n = 4.32 \times 10^{24}$ electrons/m^2 and scattering time remains the same as gold $\tau = 27\ fs$. One thing that is peculiar about this case is that, the transition frequency and the plasma frequency overlap, $f_\tau = f_p = 5.9$ THz, marked in Figure 3.6. Figure 3.6 shows the propagation constant and characteristic impedance of this material. It is clear that the material is more dispersive at low frequencies. For frequencies much higher than $f_\tau = f_p$, the material becomes "*transparent*" to the incoming wave, with the propagation constant and impedance both similar to free space ones.

3.1.2. Semiconductors

Semiconductors are arguably the most important material in modern days microelectronics industry. Mildly doped semiconductors generally have resistivity between $0.1 \sim 100\Omega cm$, much higher than metals in the GHz range. Thus, the dispersion characteristics of semiconductors have been of interest. Drude model played an important role to help scientists and engineers understand the high-frequency response of diodes [35], [36], and to provide fairly accurate results for describing the conduction results of semiconductors like silicon, at GHz and THz range [37], [38].

For semiconductors, an equivalent electron mass in Drude model can be applied to compensate for the loss of inertia due to the lattice structure and the bandgap structure of

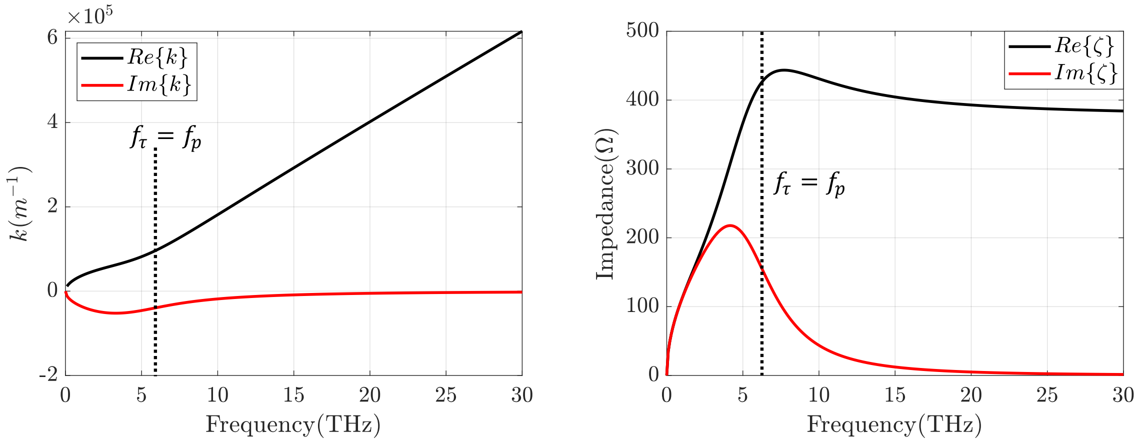

(a)

(b)

Figure 3.6: (a)The propagation constant of bad metal (b)The characteristic impedance of bad metal

the semiconductor material, $m_{si} = 0.26m_e$ for silicon [37] for example. The scattering time in this case can be found as:

$$\tau = \frac{m_{si}}{e}\mu, \tag{3.20}$$

with μ representing the mobility of the electrons, which can be represented as [39]:

$$\mu = \mu_{min} + \frac{\mu_{max} - \mu_{min}}{1 + \left(\frac{n}{N_{ref,1}}\right)^{\alpha_1}} - \frac{\mu_1}{1 + \left(\frac{N_{ref,2}}{n}\right)^{\alpha_2}}. \tag{3.21}$$

Table 3.1: Parameters in (3.21)

μ_{min}	$6.85 \times 10^{-3} m^2 V^{-1} s^{-1}$
μ_{max}	$0.1414 m^2 V^{-1} s^{-1}$
μ_1	$5.61 \times 10^{-3} m^2 V^{-1} s^{-1}$
$N_{ref,1}$	$9.20 \times 10^{22} m^{-3}$
$N_{ref,2}$	$3.41 \times 10^{26} m^{-3}$
α_1	0.711
α_2	1.98

Several parameters in (3.21) are given in Table 3.1, based on experimental data. Using (3.20) and (3.21), the dielectric parameters of silicon can be calculated from the previously-given formulas. Generally for semiconductors, both the transitional frequency and the plasma frequency, as defined in (3.12) and (3.13), are in the range of hundred GHz, depending on the doping level.

To give a specific example, consider a type of doped silicon, whose electron density is $n = 10^{22}$ electrons/m^2, with $\varepsilon_{r\infty} = 11.7$. The transition frequency is 909 GHz and the plasma frequency is 514 GHz, both in the GHz range. The resistivity of this silicon is shown in Figure 3.7, with f_τ marked in dashed lines.

We now compare the characteristic impedance of the silicon mentioned above along with two other doped silicon: $n = 5 \times 10^{21}$electrons/m^2 ($f_\tau = 852$ GHz, $f_p = 364$ GHz), and

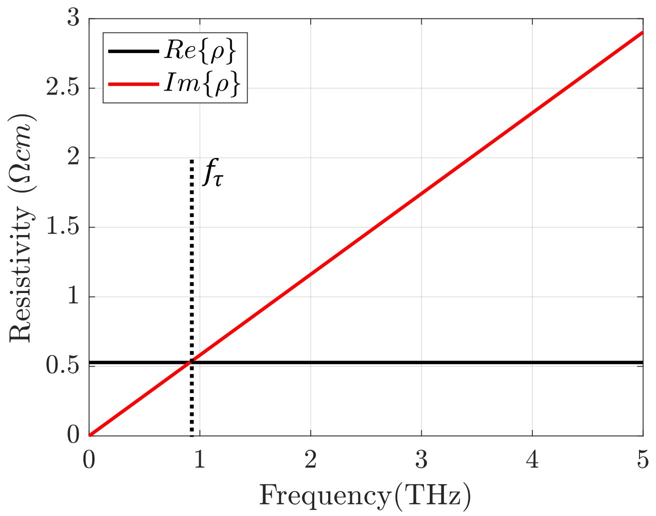

Figure 3.7: The resistivity of the silicon.

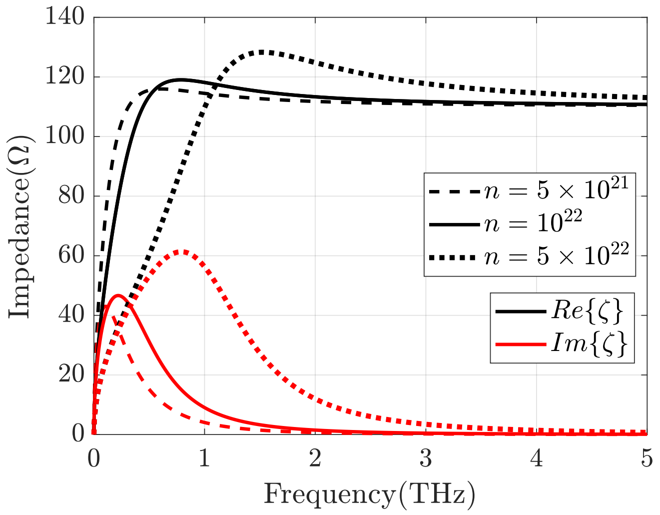

Figure 3.8: Comparison of the characteristic impedance of three silicon .

$n = 5 \times 10^{22}$electrons/m^2 (f_τ = 1216 GHz, f_p = 1150 GHz), as shown in Figure 3.8. As we can see, lower doping results in lower dispersion. Higher doping, on the other hand, has strong frequency dependence. This allows us the freedom to properly select the doping of the silicon to achieve the desired dispersion characteristics.

The dispersion properties of silicon are similar to the ones of metallic powder as studied in the previous section. However, depending on the doping level, the transition frequencies of silicon usually happen in the GHz range, instead of the THz range for metallic powders, which gives us the opportunity to use existing detectors to measure the thermal radiation of silicon at this frequency range.

3.2. Johnson-Nyquist Noise

In the year 1928, Johnson [7], along with his colleague Nyquist [8], successfully characterised the thermal noises in electrical circuits caused by thermal agitation, now widely known as Johnson-Nyquist noise. Johnson experimentally determined that, in thermodynamic equilibrium, the motion of free electrons agitated by heat will cause a fluctuation of differences in potentials between impedances in the electric circuit, resulting in an observed current. Nyquist theoretically demonstrated this discovery, which was later called Fluctuation Dissipation Theorem (FDT) [40].

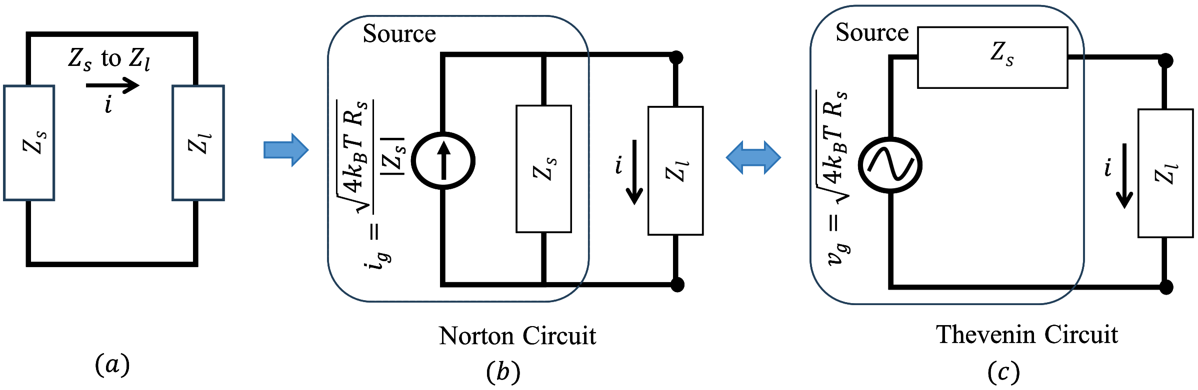

Figure 3.9: (a)Basic circuit with only two resistors in series (b)Norton equivalent circuit (c)Thevenin equivalent circuit.

Consider a basic electric circuit with only 2 impedance Z_s and Z_l, as shown in Figure 3.9(a). According to Johnson's discovery, the square of the current flowing from Z_s to Z_l can be expressed as:

$$i^2 = 4k_BT\int_0^\infty \frac{R_s(f)}{|Z_{tot}(f)|^2}df, \tag{3.22}$$

where $R_s(f) = Re\{Z_s(f)\}$ represents the real part of the source impedance and $Z_{tot}(f)$ represents the total transfer impedance of the network, both at each frequency point of f. Thus, we can represent this spectral current as:

$$i(f) = \frac{\sqrt{4k_BTR_s(f)}}{|Z_{tot}(f)|}. \tag{3.23}$$

This thermal agitated current can be represented by a Norton-type equivalent circuit shown in Figure 3.9(b). The impedance Z_s can be regarded as the internal impedance of the current source i_g, transferring energy to Z_l. The amplitude of the current source is given as:

$$i_g(f) = \frac{\sqrt{4k_BTR_s(f)}}{|Z_s(f)|}. \tag{3.24}$$

Equivalently, the circuit can also be represented in Thevenin-type, as shown in Figure 3.9(c), with a voltage source v_g connected in series with two impedances. The amplitude of the voltage source is:

$$v_g(f) = \sqrt{4k_BTR_s(f)}. \tag{3.25}$$

In both cases, the current i flowing over the load impedance Z_l in the circuit is the same as (3.23). The current generated by the thermal agitation of electrons in Z_s is divided by both impedance in the circuit, Z_s and Z_l. The amount of power absorbed by Z_l represents the power transferred from Z_s to Z_l. The situation is the same for the current generated by Z_l. When the two impedance are under the same temperature T, after the establishment of thermal equilibrium, the amount of the power flowing in one direction should be exactly the same as the power flowing in the other direction. In this situation, we can write the power transferred from Z_s to Z_l as:

$$p(f) = \frac{v_g^2}{|Z_{tot}|^2} Re\{Z_l\} = \frac{4k_B T R_s(f)}{\left|Z_s(f) + Z_l(f)\right|^2} R_l(f). \tag{3.26}$$

And the power transferred from Z_l to Z_s is:

$$p(f) = \frac{v_{gl}^2}{|Z_{tot}|^2} Re\{Z_s\} = \frac{4k_B T R_l(f)}{\left|Z_s(f) + Z_l(f)\right|^2} R_s(f), \tag{3.27}$$

where v_{gl} stands for the equivalent voltage source of Z_l. Consider that two impedances are equal and all purely real, i.e. $Z_s = Z_l = Z = R$, the power transferred in one direction is then:

$$p(f) = \frac{v_g^2}{|Z_{tot}|^2} Re\{Z_l\} = \frac{4k_B T R(f)}{4R^2(f)} R(f) = k_B T. \tag{3.28}$$

Nyquist, on the other hand, explained the experiment result of Johnson on a theoretical basis. Consider the circuit in Figure 3.10 with two resistors R which are purely real. The length of the conducting line connecting the two resistors is l. When the equilibrium is established, short the two resistors at the end of the circuit, trapping the energy generated by the two resistors. In this case, it can be also viewed as a set of waves existing in the line with length $2l$, vibrating at its natural frequencies. The lowest frequency of the wave that can exist is when the wavelength λ is equal to $2l$. In this mode, the frequency is $f = c/2l$, where c represents the propagation speed of the wave. In total, the number of these vibrating modes, also known as the degrees of freedom that can exist in this natural oscillator, in certain frequency interval df can be represented as:

$$N = \frac{2l}{c} df. \tag{3.29}$$

As suggested by the classic equipartition theorem, the average energy of each degree of freedom is $k_B T$. Then, the total energy of all the degrees of freedom is:

$$E_{tot} df = \frac{2l k_B T}{c} df. \tag{3.30}$$

In this case, the average power transferred from one end to the other end over the distance l in this electric circuit is just half of the total energy available:

$$P(f) = \frac{1}{2} \frac{E_{tot}(f)}{t} = \frac{1}{2} \frac{E(f)}{\frac{l}{c}} = k_B T, \tag{3.31}$$

which verifies the result of Johnson in (3.28). The same reasoning can also be applied to the impedance network shown in Figure 3.9(a).

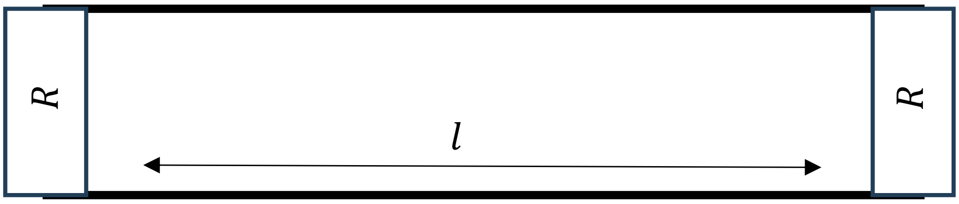

Figure 3.10: Nyquist's demonstration.

At the end of his paper [8], Nyquist pointed out, without giving any justification, that the average energy of one degree of freedom per frequency can be taken in accordance with Planck's law:

$$E_{Plk}(f) = \frac{hf}{e^{\frac{hf}{k_B T}} - 1}. \tag{3.32}$$

In this way, the current source in the circuit of Figure 3.9(b) is:

$$i_g(f) = \frac{\sqrt{\frac{4hf}{e^{\frac{hf}{k_B T}} - 1} R_s(f)}}{\left|Z_s(f)\right|}, \tag{3.33}$$

and the amplitude of the voltage source in Figure 3.9(c) can be represented by:

$$v_g(f) = \sqrt{\frac{4hf}{e^{\frac{hf}{k_B T}} - 1} R_s(f)}. \tag{3.34}$$

As stated in the paper [8] by Nyquist himself, at low frequencies and temperatures, the two kinds of expressions ($k_B T$ and (3.32)) produce the same results. For high frequencies and temperatures, however, experimental proof was lacking.

It is noteworthy that, since in Johnson-Nyquist representation we are only interested in the energy transferred from one degree of freedom to another, the phase of the current source (3.24) and the voltage source (3.25) are not defined.

4

Degrees of Freedoms in Infinite Media

In this chapter, a classic EM model [41], which sets the basis for this thesis, is introduced. Aiming at explaining the thermal radiation from ohmic media in a rigorous way, this model explains the available energy due to thermally agitation inside ohmic material from the perspective of EM theory. The available energy inside the thermal agitated radiating body in this new model is calculated from the characteristics of the medium of the real body itself, without using the reciprocity and Planck's law of black body radiation.

The total electric field in a certain medium at a certain frequency can be expanded in a *finite* number of modes (degrees of freedom) expressed as:

$$\vec{e}_{tot}\left(\vec{r},f\right) = \sum_{n=1}^{N_{DoF}} \vec{e}^{\,n,p}\left(\vec{r},f\right), \tag{4.1}$$

where N_{DoF} is the number of possible degrees of freedom inside the electric field, and $\vec{e}^{\,n,p}\left(\vec{r},f\right)$ is one degree of freedom (mode) located at $\vec{r}_n$ with polarization p, as shall be explained in detail in Section 4.1. These modes are all independent of and orthogonal to each other. If we are considering an ideal infinite medium, the N_{DoF} in this case is also infinite. In this case, N_{DoF} can be represented by the number of degrees of freedom per unit of volume. Each of these modes of the electric field is associated with a modal current. Then, we can represent the summation of all these modal currents as the total current $\vec{j}_{tot}\left(\vec{r},f\right)$ inside the electric field:

$$\vec{j}_{tot}\left(\vec{r},f\right) = \sum_{n=1}^{N_{DoF}} i_n^p\left(f\right)\vec{j}^{\,n,p}\left(\vec{r},f\right), \tag{4.2}$$

where $\vec{j}^{\,n,p}\left(\vec{r},f\right)$ represent the modal electric current density and $i_n^p\left(f\right)$ are the current amplitudes. All the degrees of freedom represent the same energy and consequently, the amplitudes of the currents are all the same for all these degrees of freedom. And the phases for these currents are considered as random. Thus the phase term could be dropped in (4.2) since we are only interested in the energy it delivers. In this sense, (4.1) and (4.2) are a macroscopic energy-wise description of the electric field, for the fact that we are unable to track the evolution of the field in the time domain. Notice that the frequency-dependent notion in both (4.1) and (4.2) does not represent the Fourier-transformed time-domain currents. Instead, they are in the unit of the square root of the spectral energy, as suggested by FDT.

This chapter first introduces the essence of the modes in the expansion of the electric field, as shown in (4.1). Each of these modes, being the lowest-order spherical wave, is a solution of Maxwell's equations either without the presence of the source or outside the source region.

Next in Section 4.2, the eigenvectors of Maxwell's equations are given, along with its corresponding eigenvalues. Based on this, an eigen-current, being the modal current in (4.2), is given in an explicit form in (4.5).

Then, the finite number of independent degrees of freedom in a certain volume is given in Section 4.3. The criterion of these degrees of freedom being decoupled from each other is given.

Finally, a Johnson-like circuit is introduced in Section 4.4 to estimate the amount of energy available inside the medium of a certain volume, rendering by each of these elementary sources.

4.1. Modal Solutions of Maxwell's Equations

We now consider a homogeneous media with infinite boundary, characterized by electric permittivity $\varepsilon = \varepsilon_0 \varepsilon_r$, free space permeability $\mu = \mu_0$, and frequency-dependent conductivity defined by Drude model in (3.3). In a source-free region, either without the presence of the source or out of the source region, the general solution of Maxwell's equation can be represented by a summation of elementary wave functions [42]. We can thus choose to represent the field with the lowest-order spherical waves, which is suitable for representing the solutions in our case, where Maxwell's equations are associated with specific spatial points $\vec{r}_n$.

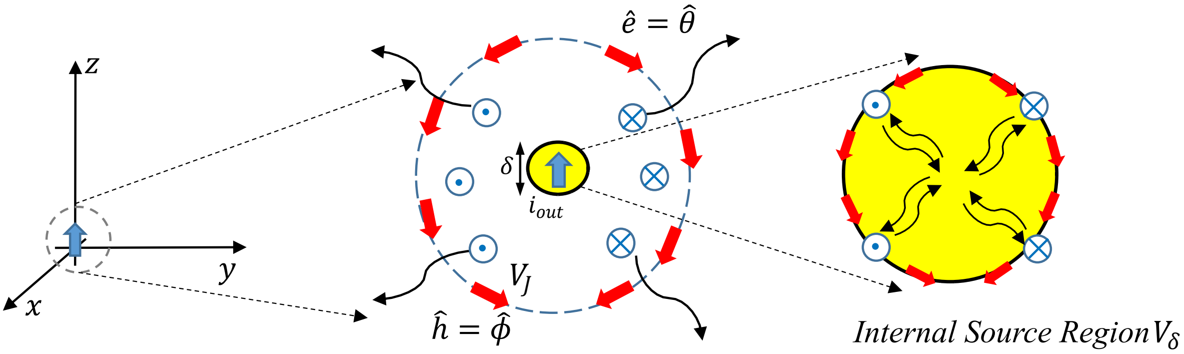

Figure 4.1: An elementary current located in the origin of the coordinate system, oriented along $\hat{z}$ direction. Electric (red arrows) and Magnetic (blue circles with dots and crossed) field lines, in the presence of a dipole radiating an outward wave. The detail of the source region with the superposition of an inward and an outward wave

The sources of these lowest-order spherical waves are elementary current sources [42]. Consider an elementary current located in the origin of the coordinate system, oriented along $\hat{z}$ direction, as shown in the left of Figure 1. The lowest-order spherical wave generated by the source propagates outward. Figure 4.1 only shows an example of the TM (transverse magnetic with respect to propagation direction $\hat{r}$) field generated by an elementary electric current. The figure in the middle shows the field configuration, with red arrows showing the electric field lines and blue dots and crosses showing the magnetic field lines. The length of the current source is δ and the outward current amplitude is i_{out}. The source itself, as shown in the zoomed-in figure at the right of Figure 4.1, can be interpreted as the superposition of the inward and outward waves with the same amplitude. Outside the source region V_δ (the region in yellow in Figure 1), only outward propagating waves remain. According to duality [42], [43], there is also a dual TE (transverse electric with respect to propagation direction $\hat{r}$) field orthogonal to the TM one, which positions at the same spatial point $\vec{r}_n$, and shares the same volume V_J. It is generated by an elementary magnetic source.

The analytical expression for this lowest-order spherical TM and TE waves outside the source region are well known, and can be found in various EM textbooks [42], [43]. For our case shown in Figure 4.1, the TM field generated by an elementary electric current source along $\hat{z}$ can be represented as:

$$e_{out}^{TMr}(\vec{r}) = i_{out}\delta\frac{\zeta\cos\theta}{2\pi}e^{-jkr}\left(\frac{1}{(kr)^2}-\frac{j}{(kr)^3}\right), \tag{4.3a}$$

$$e_{out}^{TM\theta}(\vec{r}) = i_{out}\delta\frac{j\sin\theta}{4\pi}e^{-jkr}\left[\frac{1}{kr}+\frac{1}{j(kr)^2}-\frac{1}{(kr)^3}\right], \tag{4.3b}$$

$$h_{out}^{TM\phi}(\vec{r}) = i_{out}\delta\frac{k^2\sin\theta}{4\pi}e^{-jkr}\left[j\frac{1}{kr}+\frac{1}{(kr)^2}\right], \tag{4.3c}$$

$$e_{out}^{TM\phi} = h_{out}^{TMr} = h_{out}^{TM\theta} = 0. \tag{4.3d}$$

From now on, we can use $\vec{e}^{n,p}(\vec{r})$ to indicate such electric field as in (4.1), radiated from an elementary current source centred at $\vec{r}_n$ and polarized at direction p. Each of these fields radiated by the elementary sources is regarded as a mode of the total electric field, without the presence of the source or out of the source region.

4.2. Eigenvectors of Maxwell's Equations

Using the commonly known Green's dyadic for homogenous media, one can express each of these modes, $\vec{e}^{n,p}(\vec{r})$, as:

$$\vec{e}^{n,p}(\vec{r}) = \iiint_{-\infty}^{\infty}\bar{\bar{g}}^{ej}\left(\vec{r},\vec{r}'\right)\cdot\vec{j}^{n,p}\left(\vec{r}'\right)d\vec{r}'. \tag{4.4}$$

Since that, each of these modes represents a solution of Maxwell's equations either without the presence of source or out of the source region, $\vec{j}^{n,p}\left(\vec{r}'\right)$ in (4.4) is an eigen-current associated with this mode $\vec{e}^{n,p}(\vec{r})$. This means that, for a mode $\vec{e}(\vec{r})$ that verifies Maxwell's equations in a homogeneous space, one can always find a corresponding eigen-current $\vec{j}^{n,p}(\vec{r})$ that satisfies (4.4) and $\vec{j}^{n,p}(\vec{r})$ should always bear the form as:

$$\vec{j}^{n,p}(\vec{r}) \equiv \left(\sigma + j\omega\varepsilon_0\varepsilon_r\right)\vec{e}^{n,p}(\vec{r}), \tag{4.5}$$

where σ is the complex conductivity of the medium and can be represented by its real and imaginary part as $\sigma = \sigma_r + j\sigma_i$. Substituting (4.5) into (4.4), it is clear that:

$$\iiint_{-\infty}^{\infty}\bar{\bar{g}}^{ej}\left(\vec{r},\vec{r}'\right)\cdot\vec{e}^{n,p}\left(\vec{r}'\right)d\vec{r}' = \frac{\vec{e}^{n,p}(\vec{r})}{\left(\sigma + j\omega\varepsilon_0\varepsilon_{r\infty}\right)}. \tag{4.6}$$

Thus, one can claim that, $\vec{e}^{n,p}(\vec{r})$ is one of the eigenvectors of Maxwell's equations in a homogeneous medium, and $1/\left(\sigma + j\omega\varepsilon_0\varepsilon_r\right)$ is its corresponding eigenvalue. This property is proved in [41], using the EM theorems provided in [44]. A brief proof is also provided in Appendix B of this thesis.

4.3. Numbers of Independent Degree of freedoms

Each of the modes of electric field and its corresponding eigen-current introduced in Section 4.1 and Section 4.2 can be interpreted as a degree of freedom of the total electric field. They are centred at different locations, $\vec{r}_n$, and can have 3 possible electric current polarization (TM) and 3 possible magnetic current polarization (TE) (due to the duality suggested in Section 4.1), both oriented along three axis of the coordinate system respectively. Accordingly, the total electric field in (4.1) can be expressed as:

$$\vec{e}_{tot}\left(\vec{r},f\right) = \sum_{n=1}^{N_{DoF}} \vec{e}^{\,n,p}\left(\vec{r},f\right) = \sum_{p=1}^{6}\sum_{n=1}^{N_{pos}} \vec{e}^{\,n,p}\left(\vec{r},f\right), \tag{4.7}$$

where N_{pos} is the number of positions that guarantees the degrees of freedom to be independent of each other. Each of these positions is associated with the aforementioned 6 possible polarizations. Thus we have $N_{DoF} = 6N_{pos}$.

Indeed, these modes $\vec{e}^{\,n,p}\left(\vec{r}\right)$ can exist everywhere in the space, but they are not necessarily independent, thus, not orthogonal to each other. In order to assess the independence or orthogonality between two eigenvectors, the mutual impedance of two eigenvectors $\vec{e}^{\,n,p}\left(\vec{r}\right)$ and $\vec{e}^{\,m,q}\left(\vec{r}'\right)$, can be defined using a conjugate projection on their corresponding eigen-currents as:

$$Z_{mn}^{pq} \equiv \iiint_{-\infty}^{\infty} \vec{j}^{\,n,p*}\left(\vec{r}\right)\cdot\left[\iiint_{-\infty}^{\infty} \bar{\bar{g}}\left(\vec{r},\vec{r}'\right)\cdot\vec{j}^{\,m,q}\left(\vec{r}'\right)d\vec{r}'\right]d\vec{r}. \tag{4.8}$$

Using (4.4), we can arrive at:

$$Z_{mn}^{pq} = \iiint_{-\infty}^{\infty} \vec{j}^{\,n,p*}\left(\vec{r}\right)\cdot\vec{e}^{\,m,q}\left(\vec{r}\right)d\vec{r}. \tag{4.9}$$

Replace $\vec{j}^{\,n,p}\left(\vec{r}\right)$ with the definition in (4.5), the mutual impedance can be represented as:

$$Z_{mn}^{pq} = \left(\sigma + j\omega\varepsilon_0\varepsilon_{r\infty}\right)^* \iiint_{-\infty}^{\infty} \vec{e}^{\,*n,p}\left(\vec{r}\right)\cdot\vec{e}^{\,m,q}\left(\vec{r}\right)d\vec{r}. \tag{4.10}$$

For the sake of convenience, we can then define a coupling coefficient C_{mn}^{pq} in (4.10) as:

$$C_{mn}^{pq}\left(\vec{r}_n,\vec{r}_m\right) = \iiint_{-\infty}^{\infty} \vec{e}^{\,n,p*}\left(\vec{r},\vec{r}_n\right)\vec{e}^{\,m,q}\left(\vec{r},\vec{r}_m\right)d\vec{r}. \tag{4.11}$$

Then the mutual impedance can be finally written as:

$$Z_{mn}^{pq} = \left(\sigma^* - j\omega\varepsilon_0\varepsilon_{r\infty}\right)C_{mn}^{pq}\left(\vec{r}_n,\vec{r}_m\right). \tag{4.12}$$

In order to make the two neighbouring eigen-sources independent from each other, $C_{mn}^{pq}(\vec{r}_n,\vec{r}_m)$ must be 0. If $C_{mn}^{pq}(\vec{r}_n,\vec{r}_m)$, as a function of the mutual distance $d = |\vec{r}_n - \vec{r}_m|$ of the two elements, always has a zero, then N_{DoF} is defined as:

$$N_{DoF} = N_{pos}\times 6 = \frac{Vol}{d_{min}^3}\times 6, \tag{4.13}$$

where d_{min} is the minimal distance that makes $C_{mn}^{pq}(\vec{r}_n,\vec{r}_m)$ equal to 0.

Notice that (4.13) is true only when the existence of the zero of $C_{mn}^{pq}(\vec{r}_n,\vec{r}_m)$ is confirmed. This property will be studied in Section 5.2.

4.4. Energy Available per Degree of Freedom

Since these degrees of freedom are independent from each other (details in Section 5.2) and have random phases, the total energy available per unit volume inside the medium can simply be calculated by summing up the contributions of all degrees of freedom. Given the premise that we are considering a homogeneous infinite medium, each of these degrees of freedom renders the same amount of energy, denoted as E^{1-DoF}. Intuitively, the total energy available per unit volume is simply:

$$E^{tot} = N_{DoF} \times E^{1-DoF}, \tag{4.14}$$

The next step is to establish a model to estimate the amount of energy each of these degrees of freedom can render.

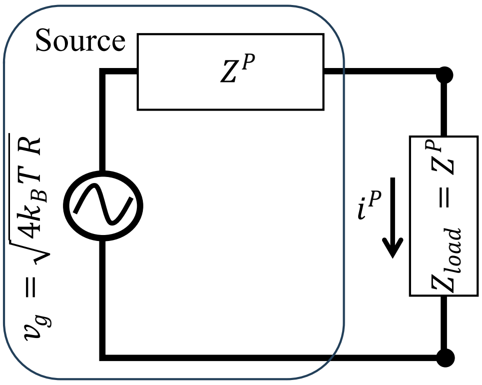

Figure 4.2: The Johnson-like Thevenin circuit

Based on Johnson's work introduced in Section 3.2, a Johnson-like circuit, as shown in Figure 4.2, was proposed in [41] to estimate the amplitude i^p of each eigen-current and the amount of energy one degree of freedom is available to deliver. Each degree of freedom is modelled as a voltage generator with an amplitude of $\sqrt{4k_B TR^p}$ and an internal impedance, which is the self-impedance Z^p of that degree of freedom, $R^p = Re\{Z^p\}$. Notice that here we only retain the amplitude of (3.25), which is associated with the classic explanation of average energy per degree of freedom $k_B T$ suggested by equipartition theorem, instead of the Planck-like correction suggested by Nyquist in (3.34).

This *"source"* is then connected to a load Z_{load} which represents the ambient environment of that degree of freedom. It can easily be seen that when $Z_{load} = Z^{p*}$, which is the case when a matched load is connected, the generator will render the maximum spectral energy $E(f) = k_B T$ to the load. However, this is hardly the case. Consider an infinite homogenous medium. In this case, $Z_{load} = Z^p$, rather than its conjugate. From Figure 4.2, the current amplitude i^p can be calculated as:

$$i_p = \frac{v_g}{2Z^p} = \frac{\sqrt{4k_B TR^p}}{2Z^p}. \tag{4.15}$$

Then, the spectral energy transferred by the generator to the load is:

$$E^{1-DoF} = \left|i_p\right|^2 Re\left\{Z^p\right\} = \frac{k_B T\,(R^p)^2}{|Z^p|^2}. \tag{4.16}$$

In order to calculate (4.16), the self-impedance Z^p of one degree of freedom must be found. This shall be addressed in Section 5.1.

5

Coupling for Eigenvectors of Maxwell's Equations

In the previous chapter, a classic EM model describing the available energy inside the ohmic medium due to thermal agitation is formed. The model is based on the degrees of freedom within the electromagnetic field, which is the eigenvectors of Maxwell's equations. The total energy available is calculated by summing up all the energy available per degree of freedom, as suggested by (4.14). In order to calculate this energy, two critical unresolved issues must be cleared, i.e. the mutual coupling coefficient (as defined in (4.11)) must always have a zero and the self-impedance Z^p of one degree of freedom must be given.

In this chapter, the self-impedance of one eigenvector is calculated and given explicitly in (5.10). The numerical results calculated from the visible part of spatial Green's function verify this analytical expression. The mutual impedance of two eigenvectors is approximated by (5.50) and is proportional to a *sinc* function, thus confirming the existence of zeros. This allows two degrees of freedom to be uncoupled from each other, with a minimum distance of $\lambda_\beta/2$. This approximation proves to be a good match with numerical results, despite some discrepancies in amplitudes for high frequencies.

Proceeding Section 4.4, the total energy available within the medium is given explicitly in Section 5.3, which decreases proportionally to $1/f^3$ at high frequencies.

5.1. Self-impedance of 1 Eigenvector

5.1.1. Analytical Derivation

The electric field of an elementary electric current source oriented along $\hat{z}$ placed at the centre of the reference system with length δ and amplitude I_0, as given in (4.3), can be expressed as:

$$\vec{e}(\vec{r}) = I_0\delta\zeta\, k^2 \frac{e^{-jkr}}{4\pi}\left[2\cos\theta\left(\frac{1}{(kr)^2}-\frac{j}{(kr)^3}\right)\hat{\boldsymbol{r}}+\sin\theta\left(\frac{j}{kr}+\frac{1}{(kr)^2}-\frac{j}{(kr)^3}\right)\hat{\boldsymbol{\theta}}\right]. \tag{5.1}$$

Notice that in (5.1), the components associated with $1/(kr)^2$ and $1/(kr)^3$ decay very fast with respect to the increase of distance r. We can define these parts of Green's function as invisible, as they represent the reactive energy surrounding the dipole, as shown in Figure 5.1. In this way, the visible part of Green's function is defined as:

$$\vec{e}_{vis}(\vec{r}) = I_0 \delta\zeta\, k^2 \frac{je^{-jkr}}{4\pi kr} \sin\theta\, \hat{\boldsymbol{\theta}}. \tag{5.2}$$

Proceeding as for (4.12), self-impedance of an elementary source is:

$$Z_{nn}^{pp} = \left(\sigma^* - j\omega\varepsilon_0\varepsilon_r\right) C_{nn}^{pp}(\vec{r}_n, \vec{r}_n), \tag{5.3}$$

where the self-coupling coefficient C_{nn}^{pp} is:

$$C_{nn}^{pp}(\vec{r}_n, \vec{r}_n) = \iiint_{-\infty}^{\infty} \vec{e}^{\,n,p*}(\vec{r}, \vec{r}_n) \vec{e}^{\,n,p}(\vec{r}, \vec{r}_n) d\vec{r}. \tag{5.4}$$

Replace $\vec{e}^{\,n,p}(\vec{r}, \vec{r}_n)$ in (5.4) with (5.2), we can arrive at:

$$C_{nn}^{pp}(\vec{r}_n, \vec{r}_n) = I_0^2 \delta^2 \frac{|\zeta|^2 |k|^2}{(4\pi)^2} \iiint_{-\infty}^{\infty} \frac{e^{jk^* r} e^{-jkr}}{r^2} \sin^2\theta\, d\vec{r}. \tag{5.5}$$

Notice that k is complex and can be represented by (3.11):

$$e^{jk^* r} e^{-jkr} = e^{j(k^* - k)r} = e^{-2k_\alpha r}. \tag{5.6}$$

Then the integral in (5.5) can be written in spherical coordinates as:

$$C_{nn}^{pp}(\vec{r}_n, \vec{r}_n) = I_0^2 \delta^2 \frac{|\zeta|^2 |k|^2}{(4\pi)^2} \int_0^{2\pi} \int_0^{\pi} \int_0^{\infty} \frac{e^{-2k_\alpha r}}{r^2} r^2 \sin^3\theta\, dr d\theta\, d\phi. \tag{5.7}$$

And the 3D integral can be closed respectively as:

$$\int_0^{2\pi} d\phi = 2\pi, \tag{5.8a}$$

$$\int_0^{\pi} \sin^3\theta\, d\theta = \frac{1}{3}\cos^3\theta - \cos\theta|_0^{\pi} = \frac{4}{3}, \tag{5.8b}$$

$$\int_0^{\infty} e^{-2k_\alpha r} dr = \frac{1}{2k_\alpha}. \tag{5.8c}$$

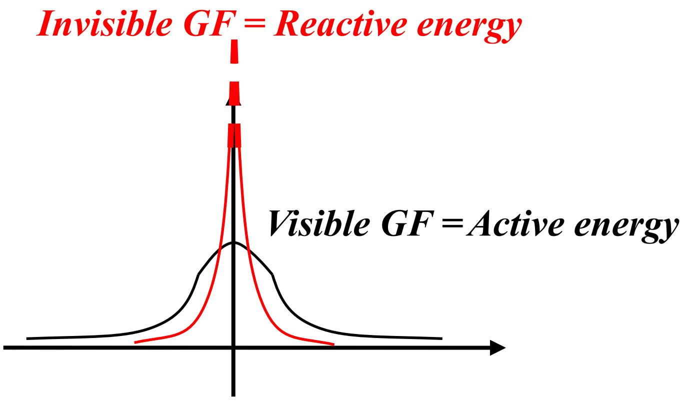

Figure 5.1: Visible and invisible part of Green's function

Combing the results in (5.8), the integral in (5.5) can be closed analytically as:

$$C_{nn}^{pp}(\vec{r}_n,\vec{r}_n) = I_0^2\delta^2\frac{|\zeta|^2|k|^2}{(4\pi)^2}\frac{4\pi}{3k_\alpha} = \frac{I_0^2\delta^2}{\lambda_0^2}\zeta_0^2\frac{\pi}{3k_\alpha}. \tag{5.9}$$

The self-coupling coefficient shown by (5.9) turns out to be purely real, which corresponds to the conjugate projection in its definition (5.4). Thus, the analytical form of self-impedance of an elementary electric current source is:

$$Z_{nn}^{pp} = \left(\sigma^* - j\omega\varepsilon_0\varepsilon_{r\infty}\right)\frac{I_0^2\delta^2}{\lambda_0^2}\zeta_0^2\frac{\pi}{3k_\alpha}. \tag{5.10}$$

Using this expression, we can now represent the spectral energy transferred by 1 degree of freedom as:

$$E^{1-DoF} = \frac{k_B T\,(R^p)^2}{|Z^p|^2} = k_B T\frac{\sigma_r^2}{\left|\sigma_r - j\sigma_i - j\omega\varepsilon_0\varepsilon_{r\infty}\right|^2}, \tag{5.11}$$

where $\sigma = \left(\sigma_r + j\sigma_i\right)$ represents the real and imaginary part of the complex conductivity.

5.1.2. Validation of the Result

In order to validate the analytical expression of self-impedance (5.9)and (5.10), a comparison with numerical results is needed. Spatial Green's function of an electric current source is expressed in its general form [45] as:

$$\bar{\bar{G}}^{ej}(\vec{r},\vec{r}\,') = -jk\zeta\frac{e^{-jk|R|}}{4\pi|R|}\left(\left[\bar{\bar{I}}-\hat{R}\hat{R}\right] - \frac{j}{k|R|}\left[\bar{\bar{I}}-3\hat{R}\hat{R}\right] - \frac{1}{k^2|R|^2}\left[\bar{\bar{I}}-3\hat{R}\hat{R}\right]\right), \tag{5.12}$$

where $|R| = |\vec{r}-\vec{r}\,'|$ is the distance between source and observation point. Similar to (5.1), the latter two terms in (5.12) can also be regarded as the invisible part of the Green's function. Hence, the visible part of the spatial Green's function is:

$$\bar{\bar{G}}^{ej}_{vis}(\vec{r},\vec{r}\,') = -jk\zeta\left[\bar{\bar{I}}-\hat{R}\hat{R}\right]\frac{e^{-jk|R|}}{4\pi|R|}. \tag{5.13}$$

Then according to (5.3) the self-impedance of an elementary dipole can be expressed as:

$$\begin{aligned} Z_{nn}^{pp} &= \left(\sigma^* - j\omega\varepsilon_0\varepsilon_{r\infty}\right)C_{nn}^{pp}(\vec{r}_n,\vec{r}_n) \\ &= \left(\sigma^* - j\omega\varepsilon_0\varepsilon_{r\infty}\right)I_0^2\delta^2\iiint_{-\infty}^{\infty}\bar{\bar{G}}^{ej*}_{vis}(\vec{r},\vec{r}_n)\cdot\hat{p}\,\bar{\bar{G}}^{ej}_{vis}(\vec{r},\vec{r}_n)\cdot\hat{p}\,d\vec{r}. \end{aligned} \tag{5.14}$$

The self-impedance can then be calculated numerically using (5.14) by discretizing the 3D space adjacent to the source. Figure 5.2 shows the comparison between numerical and analytical results of the self-impedance for a bad metal, BM1, whose electron density is $n = 5\times10^{24}$ electrons/m^2 and scattering time is $\tau = 1.3\times10^{-14}$ s. As we can see from the figure, the numerical and analytical results show a good agreement with each other.

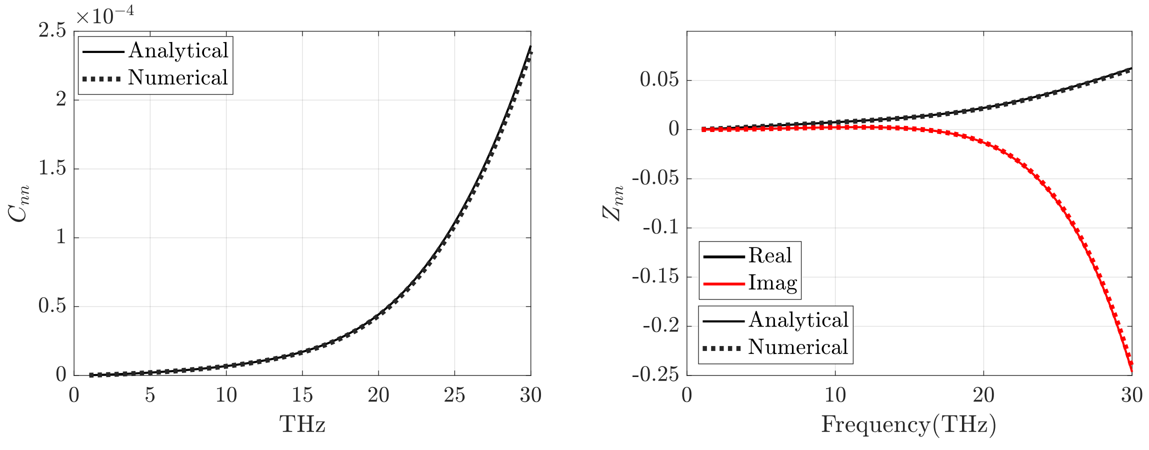

(a) Self-coupling C_{nn}

(b) Self-impedance Z_{nn}

Figure 5.2: Comparison between numerical and analytical results of self-coupling

5.2. Mutual Impedance of 2 Eigenvectors

5.2.1. Analytical Derivation

The mutual impedance of 2 eigenvectors can be expressed by (4.11) and (4.12). Consider the same elementary electric current source with length δ and amplitude I_0, but placed at point $\vec{r}_n$ and oriented along $\hat{p}$ this time. The electric field associated to it can be written as:

$$\vec{e}^{\,n,p}(\vec{r}) = \iiint_{-\infty}^{\infty} \bar{\bar{G}}^{ej}(\vec{r},\vec{r}_n)\cdot\vec{j}(\vec{r}_n)\cdot\hat{p}\,d\vec{r}_n = \bar{\bar{G}}^{ej}(\vec{r},\vec{r}_n)\,\delta\,I_0\cdot\hat{p}. \tag{5.15}$$

According to (4.11), the coupling coefficient C_{mn}^{pq} can then be expressed as:

$$C_{mn}^{pq}(\vec{r}_n,\vec{r}_m) = I_0^2\delta^2\iiint_{-\infty}^{\infty} \bar{\bar{G}}^{ej*}(\vec{r},\vec{r}_n)\cdot\hat{p}\,\bar{\bar{G}}^{ej}(\vec{r},\vec{r}_m)\cdot\hat{q}\,d\vec{r}. \tag{5.16}$$

Using 3D Fourier transform, the spatial Green's function in (5.16) can be represented in spectral domain:

$$\bar{\bar{G}}^{ej}(x,y,z;x',y',z') = \frac{j\zeta}{k(2\pi)^3}\int_{-\infty}^{\infty}\int_{-\infty}^{\infty}\int_{-\infty}^{\infty}\frac{e^{-jk_x(x-x')}e^{-jk_y(y-y')}e^{-jk_z(z-z')}}{k^2-k_x^2-k_y^2-k_z^2}\bar{\bar{D}}\left(\vec{k}\right) dk_x dk_y dk_z, \tag{5.17}$$

where $\vec{k} = k_x\hat{x}+k_y\hat{y}+k_z\hat{z}$, and $\bar{\bar{D}}\left(\vec{k}\right)$ is a dyad:

$$\bar{\bar{D}}\left(\vec{k}\right) = \begin{bmatrix} k^2-k_x^2 & -k_xk_y & -k_xk_z \\ -k_xk_y & k^2-k_y^2 & -k_yk_z \\ -k_xk_z & -k_yk_z & k^2-k_z^2 \end{bmatrix} = (k^2\bar{\bar{I}} - k_r^2\hat{k}\hat{k}), \tag{5.18}$$

where $\bar{\bar{I}}$ is the identity matrix, $k_r^2 = k_x^2+k_y^2+k_z^2$, and $\hat{k} = \vec{k}/k_r$ is the unit vector of $\vec{k}$. Replace (5.17) into (5.16), we can arrive at:

$$C_{mn}^{pq}(\vec{r}_n,\vec{r}_m) = \frac{I_0^2\delta^2}{(2\pi)^6}\left|\frac{\zeta}{k}\right|^2 \iiint_{-\infty}^{\infty}\iiint_{-\infty}^{\infty}\frac{e^{jk_x(x-x_n)}e^{jk_y(y-y_n)}e^{jk_z(z-z_n)}}{k^{*2}-k_x^2-k_y^2-k_z^2}\bar{\bar{D}}^*\left(\vec{k}\right)\cdot\hat{p}\,dk_xdk_ydk_z$$
$$\iiint_{-\infty}^{\infty}\frac{e^{-jk'_x(x-x_m)}e^{-jk'_y(y-y_m)}e^{-jk'_z(z-z_m)}}{k^2-k'^2_x-k'^2_y-k'^2_z}\bar{\bar{D}}\left(\vec{k}\right)\cdot\hat{q}\,dk'_xdk'_ydk'_z\,d\vec{r}. \tag{5.19}$$

Rearranging the terms in (5.19) and expand $\bar{\bar{D}}\left(\vec{k}\right)$ by the form in (5.18):

$$
\begin{aligned}
C_{mn}^{pq}\left(\vec{r}_n,\vec{r}_m\right) = \frac{I_0^2\delta^2}{(2\pi)^6}\left|\frac{\zeta}{k}\right|^2 & \iiint_{-\infty}^{\infty} e^{j(k_x-k'_x)x}e^{j(k_y-k'_y)y}e^{j(k_z-k'_z)z}dxdydz \\
& \iiint_{-\infty}^{\infty} \frac{e^{-jk_xx_n}e^{-jk_yy_n}e^{-jk_zz_n}}{k^{*2}-k_x^2-k_y^2-k_z^2}\left(k^{*2}\bar{\bar{I}}-k_r^{*2}\hat{k}\hat{k}\right)\cdot\hat{p}dk_xdk_ydk_z \\
& \qquad \iiint_{-\infty}^{\infty} \frac{e^{jk'_xx_m}e^{jk'_yy_m}e^{jk'_zz_m}}{k^2-k'^2_x-k'^2_y-k'^2_z}(k^2\bar{\bar{I}}-k_r^2\hat{k}'\hat{k}')\cdot\hat{q}dk'_xdk'_ydk'_z. \qquad (5.20)
\end{aligned}
$$

We can close the first 3D integral in $d\vec{r} = dxdydz$ as:

$$
\iiint_{-\infty}^{\infty} e^{j(k_x-k'_x)x}e^{j(k_y-k'_y)y}e^{j(k_z-k'_z)z}dxdydz = (2\pi)^3\,\delta(k_x-k'_x)\delta(k_y-k'_y)\delta(k_z-k'_z). \qquad (5.21)
$$

Substituting (5.21) into (5.20), the 9D integral in (3.6) can then be reduced into a 3D integral:

$$
\begin{aligned}
C_{mn}^{pq}\left(\vec{r}_n,\vec{r}_m\right) = \frac{I_0^2\delta^2}{(2\pi)^3}\left|\frac{\zeta}{k}\right|^2 \iiint_{-\infty}^{\infty} & \frac{e^{-jk_xx_n}e^{-jk_yy_n}e^{-jk_zz_n}}{k^{*2}-k_x^2-k_y^2-k_z^2}\,\frac{e^{jk_xx_m}e^{jk_yy_m}e^{jk_zz_m}}{k^2-k_x^2-k_y^2-k_z^2} \\
& \left(k^{*2}\bar{\bar{I}}-k_r^{*2}\hat{k}\hat{k}\right)\cdot\hat{p}(k^2\bar{\bar{I}}-k_r^2\hat{k}\hat{k})\cdot\hat{q}dk_xdk_ydk_z. \qquad (5.22)
\end{aligned}
$$

Rearranging the terms and we have:

$$
\begin{aligned}
C_{mn}^{pq}\left(\vec{r}_n,\vec{r}_m\right) = \frac{I_0^2\delta^2}{(2\pi)^3}\left|\frac{\zeta}{k}\right|^2 \iiint_{-\infty}^{\infty} & \frac{e^{-jk_x(x_n-x_m)}e^{-jk_y(y_n-y_m)}e^{-jk_z(z_n-z_m)}}{(k^{*2}-k_x^2-k_y^2-k_z^2)(k^2-k_x^2-k_y^2-k_z^2)} \\
& \left(k^{*2}\bar{\bar{I}}-k_r^{*2}\hat{k}\hat{k}\right)\cdot\hat{p}(k^2\bar{\bar{I}}-k_r^2\hat{k}\hat{k})\cdot\hat{q}dk_xdk_ydk_z. \qquad (5.23)
\end{aligned}
$$

Now, we focus on the terms induced by the Green's dyad $\bar{\bar{D}}\left(\vec{k}\right)$. A polarization function can be defined as:

$$
\begin{aligned}
pol^2\left(k_r\right) = \left(k^{*2}\bar{\bar{I}}-k_r^{*2}\hat{k}\hat{k}\right)\cdot\hat{p}\left(k^2\bar{\bar{I}}-k_r^2\hat{k}\hat{k}\right)\cdot\hat{q} &= \left|k^2\right|^2\left(\bar{\bar{I}}-\frac{k_r^{2*}}{k^{2*}}\hat{k}\hat{k}\right)\cdot\hat{p}\left(\bar{\bar{I}}-\frac{k_r^2}{k^2}\hat{k}\hat{k}\right)\cdot\hat{q} \\
&= \left|k^2\right|^2 pol_{real}^2(k_r), \qquad (5.24)
\end{aligned}
$$

where $\left|k^2\right|^2 = k^{2*}k^2$. Then (5.23) can be expressed as:

$$
C_{mn}^{pq}\left(\vec{r}_n,\vec{r}_m\right) = \frac{I_0^2\delta^2}{(2\pi)^3}\left|\zeta k\right|^2 \iiint_{-\infty}^{\infty} \frac{e^{-jk_x(x_n-x_m)}e^{-jk_y(y_n-y_m)}e^{-jk_z(z_n-z_m)}}{(k^{*2}-k_x^2-k_y^2-k_z^2)(k^2-k_x^2-k_y^2-k_z^2)}pol_{real}^2dk_xdk_ydk_z. \qquad (5.25)
$$

Now, we can change (5.25) into spherical coordinate system by adopting the standard procedure of changing variables:

$$
\begin{cases}
k_x = k_r\sin\beta\cos\alpha, \\
k_y = k_r\sin\beta\sin\alpha, \\
k_z = k_r\cos\beta.
\end{cases} \qquad (5.26)
$$

And define another set of variables to represent the position of two dipoles in spherical coordinate:

$$\begin{cases} (x_n - x_m) = d\sin\theta\cos\phi, \\ (y_n - y_m) = d\sin\theta\sin\phi, \\ (z_n - z_m) = d\cos\theta. \end{cases} \tag{5.27}$$

where $d = \sqrt{(x_n - x_m)^2 + (y_n - y_m)^2 + (z_n - z_m)^2}$ represents the distance of this two dipoles. Then, (5.25) can be written as:

$$C_{mn}^{pq}(\vec{r}_n, \vec{r}_m) = \frac{I_0^2 \delta^2 |\zeta k|^2}{(2\pi)^3} \int_0^\infty \int_0^{2\pi} \int_0^\pi \frac{e^{-jk_r d(\sin\beta\cos\alpha\sin\theta\cos\phi + \sin\beta\sin\alpha\sin\theta\sin\phi + \cos\beta\cos\theta)}}{(k^{*2} - k_r^2)(k^2 - k_r^2)} k_r^2 \sin\beta pol_{real}^2 \, d\beta d\alpha dk_r. \tag{5.28}$$

Simplifying (5.28) using trigonometric identities, we can arrive at:

$$C_{mn}^{pq}(\vec{r}_n, \vec{r}_m) = \frac{I_0^2 \delta^2 |\zeta k|^2}{(2\pi)^3} \int_0^\infty \int_0^{2\pi} \int_0^\pi \frac{e^{-jk_r d(\sin\beta\sin\theta\cos(\alpha-\phi))} e^{-jk_r d\cos\beta\cos\theta}}{(k^{*2} - k_r^2)(k^2 - k_r^2)} pol_{real}^2 k_r^2 \sin\beta d\beta d\alpha dk_r. \tag{5.29}$$

In order to close the 3D integral in (5.29), from now on we will take a bold assumption that $pol_{real}^2 \approx 1/\sqrt{\pi}$. However, one can always argue that this assumption is very brutal. In fact, pol_{real}^2 is a function of 3 variables k_r, β and α. Considering the most coupled case in which the two dipoles are polarized at the same direction, for example $\hat{p} = \hat{q} = \hat{z}$, pol_{real}^2 can be expressed as:

$$pol_{real}^2(k_r) = \left(\bar{\bar{I}} - \frac{k_r^{2*}}{k^{2*}} \hat{k}\hat{k}\right) \cdot \hat{z} \left(\bar{\bar{I}} - \frac{k_r^2}{k^2} \hat{k}\hat{k}\right) \cdot \hat{z} = \left(-\frac{k_r^{2*}}{k^{2*}} \sin\beta\cos\alpha\cos\beta\right) \left(-\frac{k_r^2}{k^2} \sin\beta\cos\alpha\cos\beta\right) + \left(-\frac{k_r^{2*}}{k^{2*}} \sin\beta\sin\alpha\cos\beta\right) \left(-\frac{k_r^2}{k^2} \sin\beta\sin\alpha\cos\beta\right) + \left(1 - \frac{k_r^{2*}}{k^{2*}} \cos^2\beta\right) \left(1 - \frac{k_r^2}{k^2} \cos^2\beta\right). \tag{5.30}$$

(5.30) is a very complicated function. It will be a very difficult job to close the 3D integral if pol_{real}^2 stays in the integral by its full form like (5.30). The effect of the assumption $pol_{real}^2 \approx 1/\sqrt{\pi}$ on the final result C_{mn}^{pq} and Z_{mn}^{pq} will be closely examined in Section 5.2.2 and 5.2.3. Another approximation for pol_{real}^2 is shown in Appendix B, which proves to perform worse than $pol_{real}^2 \approx 1/\sqrt{\pi}$. After taking $pol_{real}^2 \approx 1/\sqrt{\pi}$, (5.29) can be written as:

$$C_{mn}^{pq}(\vec{r}_n, \vec{r}_m) = \frac{I_0^2 \delta^2 |\zeta k|^2}{(2\pi)^3} \frac{1}{\sqrt{\pi}} \int_0^\infty \int_0^{2\pi} \int_0^\pi \frac{e^{-jk_r d(\sin\beta\sin\theta\cos(\alpha-\phi))} e^{-jk_r d\cos\beta\cos\theta}}{(k^{*2} - k_r^2)(k^2 - k_r^2)} k_r^2 \sin\beta d\beta d\alpha dk_r. \tag{5.31}$$

Then, one shall notice that the integral in α can be closed analytically in the form of 0th order Bessel functions of the first kind [46]:

$$\int_0^{2\pi} e^{-jk_r d\sin\theta\sin\beta\cos(\alpha-\phi)} d\alpha = 2\pi J_0\left(k_r d\sin\theta\sin\beta\right). \tag{5.32}$$

Substitute (5.32) into (5.31), we have:

$$C_{mn}^{pq}\left(\vec{r}_n,\vec{r}_m\right)=\frac{1}{\sqrt{\pi}}\frac{I_0^2\delta^2\left|\zeta k\right|^2}{(2\pi)^3}2\pi\int_0^{\infty}\int_0^{\pi}\frac{J_0\left(k_r d\sin\theta\sin\beta\right)e^{-jk_r d\cos\beta\cos\theta}}{(k^{*2}-k_r^2)(k^2-k_r^2)}k_r^2\sin\beta d\beta dk_r. \tag{5.33}$$

In order to change the integral domain over k_r to $[-\infty,\infty]$, (5.33) can be represented as:

$$C_{mn}^{pq}\left(\vec{r}_n,\vec{r}_m\right)=\frac{1}{\sqrt{\pi}}\frac{I_0^2\delta^2\left|\zeta k\right|^2}{(2\pi)^3}2\pi\frac{1}{2}\int_{-\infty}^{\infty}\int_0^{\pi}\frac{H_0^{(2)}\left(k_r d\sin\theta\sin\beta\right)e^{-jk_r d\cos\beta\cos\theta}}{(k^{*2}-k_r^2)(k^2-k_r^2)}k_r^2\sin\beta d\beta dk_r, \tag{5.34}$$

where $H_0^{(2)}$ represents the 0th order Hankel functions of the second kind. For large z, 0th order Hankel functions of the second kind can be approximated as [46]:

$$H_0^{(2)}(z)\approx\sqrt{\frac{2}{\pi z}}e^{-jz}e^{\frac{j\pi}{4}}. \tag{5.35}$$

Using this approximation, we have:

$$H_0^{(2)}\left(k_r d\sin\theta\sin\beta\right)\approx\sqrt{\frac{2}{\pi}}\frac{1}{\sqrt{k_r d\sin\theta\sin\beta}}\,e^{-jk_r d\sin\theta\sin\beta}e^{\frac{j\pi}{4}}. \tag{5.36}$$

Figure 5.3 shows the comparison between the Hankel functions $H_0^{(2)}\left(k_r d\sin\theta\sin\beta\right)$ and its approximation in (5.36). The Hankel function is well approximated by (5.36) when $k_r d$ is relatively large.

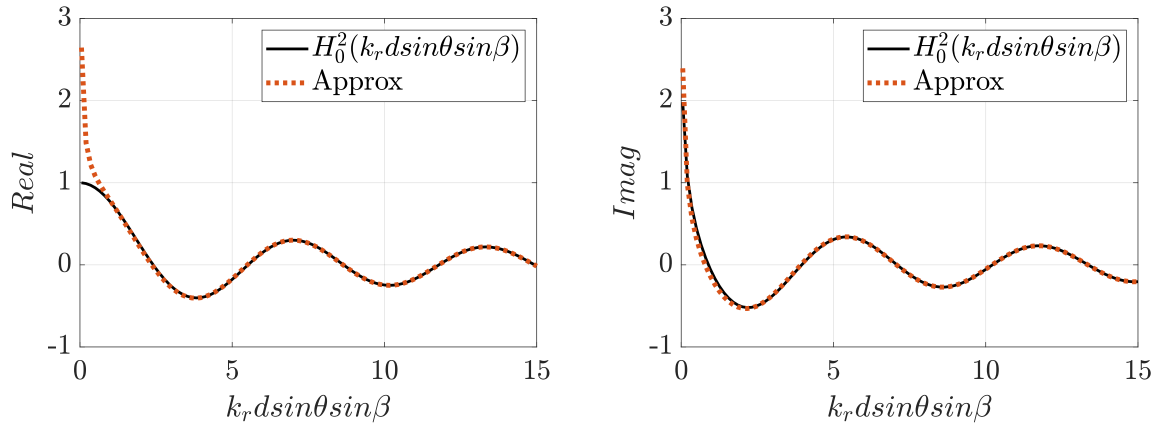

(a) Real part

(b) Imaginary part

Figure 5.3: Comparison between the left and right hand side of (5.36)

Using the approximation in (5.36), (5.34) can be represented as:

$$C_{mn}^{pq}\left(\vec{r}_n,\vec{r}_m\right)=\frac{1}{\sqrt{\pi}}\frac{I_0^2\delta^2\left|\zeta k\right|^2}{(2\pi)^3}\pi\sqrt{\frac{2}{\pi}}$$
$$\int_{-\infty}^{\infty}\int_0^{\pi}\frac{e^{\frac{j\pi}{4}}}{\sqrt{k_r d\sin\theta\sin\beta}}\frac{e^{-jk_r d\sin\theta\sin\beta}e^{-jk_r d\cos\beta\cos\theta}}{(k^{*2}-k_r^2)(k^2-k_r^2)}k_r^2\sin\beta d\beta dk_r. \tag{5.37}$$

The next step is to close the angular integral in β. Using the trigonometric identities, the integral in β can be represented as:

$$\int_0^{\pi} e^{\frac{j\pi}{4}} \frac{e^{-jk_r d\sin\theta\sin\beta} e^{-jk_r d\cos\beta\cos\theta}}{\sqrt{k_r d\sin\theta\sin\beta}} \sin\beta d\beta = \int_0^{\pi} e^{\frac{j\pi}{4}} \frac{e^{-jk_r d\cos(\beta-\theta)}}{\sqrt{k_r d\sin\theta\sin\beta}} \sin\beta d\beta. \tag{5.38}$$

Notice that (5.38) can be evaluated by its first order saddle point $\beta_s = \theta$ as:

$$\int_0^{\pi} e^{\frac{j\pi}{4}} \frac{e^{-jk_r d\cos(\beta-\theta)}}{\sqrt{k_r d\sin\theta\sin\beta}} \sin\beta d\beta \approx \frac{e^{\frac{j\pi}{4}}}{\sqrt{k_r d}} \int_0^{\pi} e^{-jk_r d\cos(\beta-\theta)} d\beta. \tag{5.39}$$

Using an approximation method provided in page 382 of [47], if function $f(z)$ has no singularities near the first order saddle point z_s of $q(z)$, the following integral can be approximated as:

$$I(\Omega) = \int_{SDP} f(z)\, e^{j\Omega\, \hat{q}(z)} dz \approx \sqrt{\frac{2\pi}{\Omega\left|\hat{q}''(z_s)\right|}} f(z_s)\, e^{j\Omega\, \hat{q}(z_s) \pm \frac{j\pi}{4}}\ ,\ \ \hat{q}'' \gtrless 0, \tag{5.40}$$

where SDP stands for Steepest Descend Path, $\hat{q}$ denotes that both z_s and the phase term $\Omega\ \hat{q}(z)$ are real, and $\hat{q}''$ indicates the second-order derivatives. Applying the identity in (5.40) into (5.39), we can arrive at:

$$\frac{e^{\frac{j\pi}{4}}}{\sqrt{k_r d}} \int_0^{\pi} e^{-jk_r d\cos(\beta-\theta)} d\beta \approx \frac{e^{\frac{j\pi}{4}}}{\sqrt{k_r d}} \sqrt{2\pi} \frac{e^{\frac{j\pi}{4}} e^{-jk_r d}}{\sqrt{k_r d}} = \sqrt{2\pi} \frac{j e^{-jk_r d}}{k_r d}. \tag{5.41}$$

Substitute (5.41) back into (5.37), the integral now is only left with 1 dimension:

$$C_{mn}^{pq}(\vec{r}_n, \vec{r}_m) = \frac{1}{\sqrt{\pi}} \frac{\delta^2 |\zeta k|^2}{(2\pi)^3} 2\pi \frac{j}{d} \int_{-\infty}^{\infty} \frac{k_r e^{-jk_r d}}{(k^{*2} - k_r^2)(k^2 - k_r^2)} dk_r. \tag{5.42}$$

The integral of k_r on the right hand side of (5.42) can be closed using residue theorem. This integral is in the form:

$$I = \int_{-\infty}^{\infty} f(k_r)\, dk_r = \int_{-\infty}^{\infty} \frac{k_r e^{-jk_r d}}{(k^{*2} - k_r^2)(k^2 - k_r^2)} dk_r. \tag{5.43}$$

It is clear that the function $f(k_r)$ has four poles: k, k^*, $-k^*$ and k, as shown in Figure 5.4. In order to make the function converge, the two poles for $Im\{k_r\} < 0$, namely k and $-k^*$, are selected for the following process.

We can define a closed clockwise contour C as shown in Figure 5.4. Using the residue theorem:

$$\begin{aligned} I = \int_{-\infty}^{\infty} \frac{k_r e^{-jk_r d}}{(k^{*2} - k_r^2)(k^2 - k_r^2)} dz &= \int_{-C} \frac{k_r e^{-jk_r d}}{(k^* - k_r)(k^* + k_r)(k - k_r)(k + k_r)} dz \\ &= -2\pi j \left[Res\left(f, k\right) + Res\left(f, -k^*\right)\right]. \end{aligned} \tag{5.44}$$

First, we look at $Res\left(f, k\right)$:

$$\begin{aligned} Res\left(f, k\right) &= \lim_{k_r \to k} (k_r - k) \frac{k_r e^{-jk_r d}}{(k - k_r)(k + k_r)(k^* - k_r)(k^* + k_r)} \\ &= \frac{-k}{2k} \frac{e^{-jkd}}{(k^* - k)(k^* + k)} = -\frac{1}{2} \frac{e^{-jkd}}{\left(2jk_\alpha\right)\left(2k_\beta\right)} = -\frac{e^{-jk_\beta d} e^{-k_\alpha d}}{8jk_\alpha k_\beta}. \end{aligned} \tag{5.45}$$

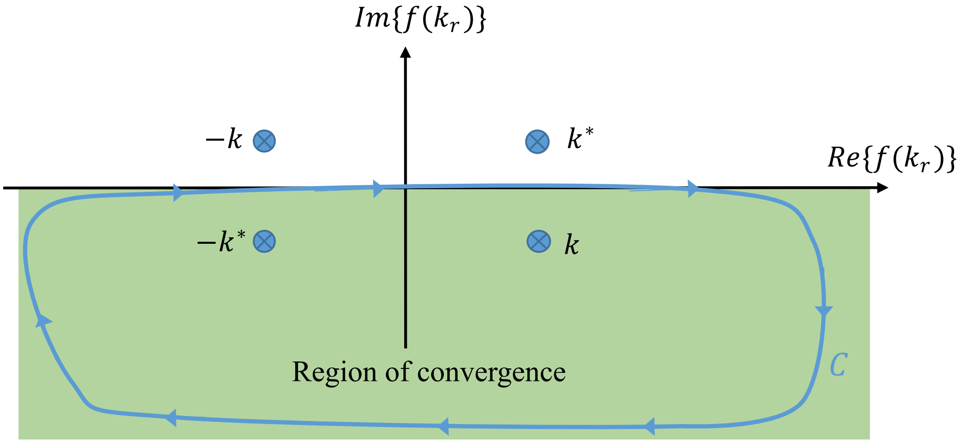

Figure 5.4: Position of four poles in the complex plane

Then, we look at $Res\left(f,-k^*\right)$:

$$
\begin{aligned}
Res\left(f,-k^*\right) &= \lim_{k_r\to -k^*}\left(k_r+k^*\right)\frac{k_r e^{-jk_r d}}{\left(k-k_r\right)\left(k+k_r\right)\left(k^*-k_r\right)\left(k^*+k_r\right)}\\
&= \frac{-k^*}{2k^*}\frac{e^{jk^*d}}{\left(k+k^*\right)\left(k-k^*\right)} = \frac{-1}{2}\frac{e^{jk^*d}}{\left(-2jk_\alpha\right)\left(2k_\beta\right)} = \frac{e^{jk_\beta d}e^{-k_\alpha d}}{8jk_\alpha k_\beta}.
\end{aligned}
\tag{5.46}
$$

Substituting (5.45) and (5.46) back into (5.44), we can finally close the integral as:

$$
I = -2\pi j\left[-\frac{e^{-jk_\beta d}e^{-k_\alpha d}}{8jk_\alpha k_\beta}+\frac{e^{jk_\beta d}e^{-k_\alpha d}}{8jk_\alpha k_\beta}\right] = -\frac{\pi e^{-k_\alpha d}}{2k_\alpha k_\beta}j\sin\left(k_\beta d\right).
\tag{5.47}
$$

Substitute (5.47) into (5.42):

$$
C_{mn}^{pq}\left(\vec r_n,\vec r_m\right) = \frac{1}{\sqrt{\pi}}\frac{\delta^2\left|\zeta k\right|^2}{(2\pi)^3}2\pi\frac{1}{d}\frac{\pi e^{-k_\alpha d}}{2k_\alpha k_\beta}\sin\left(k_\beta d\right) = \frac{1}{\sqrt{\pi}}\frac{\delta^2\left|\zeta k\right|^2}{8\pi}\frac{e^{-k_\alpha d}}{k_\alpha}\operatorname{sinc}\left(k_\beta d\right).
\tag{5.48}
$$

Rearranging the terms, (5.48) can be written as:

$$
C_{mn}^{pq}\left(\vec r_n,\vec r_m\right) = \frac{1}{\sqrt{\pi}}\frac{\delta^2}{\lambda_0^2}\zeta_0^2\frac{\pi}{2k_\alpha}e^{-k_\alpha d}\operatorname{sinc}\left(k_\beta d\right).
\tag{5.49}
$$

The comparison between the numerical evaluation of the 3D integral (5.31) and the analytical expression (5.49) we derived for the same bad metal BM1 as in Section 5.1.2 is shown in Figure 5.5. The distance of the two dipoles is taken as the penetration depth of the material, i.e., $d = \delta_p = 1/k_\alpha$. It can be seen from the figure that the 3D integral is well approximated by (5.49).

Finally, we can write the analytical expression for mutual impedance Z_{mn}^{pq} as:

$$
Z_{mn}^{pq} = \left(\sigma^* - j\omega\varepsilon_0\varepsilon_{r\infty}\right)C_{mn}^{pq}\left(\vec r_n,\vec r_m\right) = \left(\sigma^* - j\omega\varepsilon_0\varepsilon_r\right)\frac{1}{\sqrt{\pi}}\frac{\delta^2}{\lambda_0^2}\zeta_0^2\frac{\pi}{2k_\alpha}e^{-k_\alpha d}\operatorname{sinc}\left(k_\beta d\right).
\tag{5.50}
$$

Based on the analytical expressions given in (5.49) and (5.50), it is easy to find that two elementary dipoles are decoupled when:

$$
d = n\frac{\pi}{k_\beta} = n\frac{\lambda_\beta}{2},\quad n\in\mathbb{N},
\tag{5.51}
$$

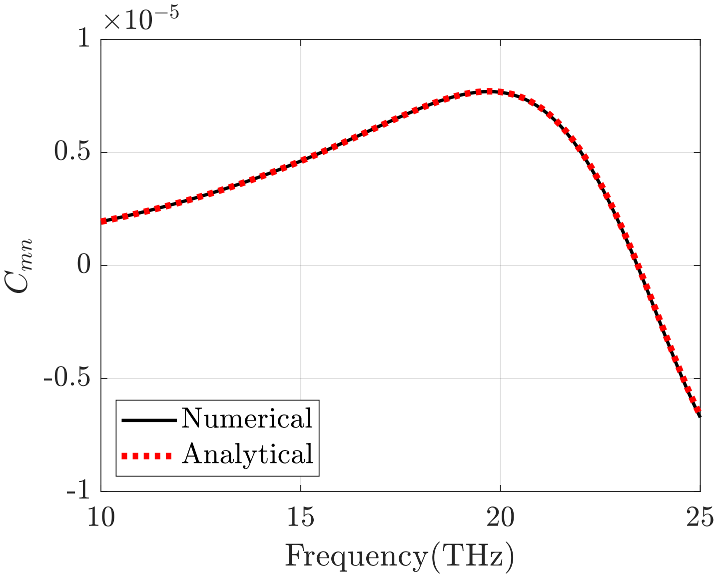

Figure 5.5: Comparison between the analytical expression (5.49) and numerical validation of (5.31)

where n is a positive integer and $\lambda_\beta = 2\pi / k_\beta$ is the real part of effective wavelength. In this case $C_{mn}^{pq} = Z_{mn}^{pq} = 0$. The first null (the smallest positive root of function (5.50)) occurs just when $n = 1$:

$$d_{\min} = \frac{\pi}{k_\beta} = \frac{\lambda_\beta}{2}. \tag{5.52}$$

In this case, the number of degrees of freedom in (4.13) can be expressed as:

$$N_{DoF} = N_{pos} \times 6 = \frac{Vol}{d_{\min}^3} \times 6 = \frac{8Vol}{\lambda_\beta^3} \times 6. \tag{5.53}$$

It is worth pointing out that the *sinc* term in (5.50) resembles the *sinc* in field coherence introduced in Section 2.4. However, field coherence in Section 2.4 is the relation of the field outside the source region, assuming a plane wave expansion. While our model here in (5.50) represents the coupling of the eigen-sources themselves.

5.2.2. Validation of the Asymptotic Result

Similar to Section 5.1.2, the validity of the asymptotic expression of the mutual impedance (5.49) and (5.50) need to be checked with the numerical results calculated by the spatial Green's function. Using the visible Green's function defined in (5.13), the mutual coupling coefficient C_{mn}^{pq} of two elementary electric current source n, p and m, q can be expressed as:

$$C_{mn}^{pq}(\vec{r}_n, \vec{r}_m) = \delta^2 \iiint_{-\infty}^{\infty} \overline{\overline{G}}_{vis}^{ej*}(\vec{r}, \vec{r}_n) \cdot \hat{p}\; \overline{\overline{G}}_{vis}^{ej}(\vec{r}, \vec{r}_m) \cdot \hat{q}\, d\vec{r}. \tag{5.54}$$

Then the mutual impedance Z_{mn}^{pq} of the two dipoles can be expressed as:

$$Z_{mn}^{pq}(\vec{r}_n, \vec{r}_m) = \left(\sigma^* - j\omega\varepsilon_0\varepsilon_{r\infty}\right)\delta^2 \iiint_{-\infty}^{\infty} \overline{\overline{G}}_{vis}^{ej*}(\vec{r}, \vec{r}_n) \cdot \hat{p}\; \overline{\overline{G}}_{vis}^{ej}(\vec{r}, \vec{r}_m) \cdot \hat{q}\, d\vec{r}. \tag{5.55}$$

The comparisons of the mutual coupling C_{mn}^{pq} and Z_{mn}^{pq}, between the asymptotic analytical expression ((5.49), (5.50)) and the numerical result calculated by spatial visible Green's

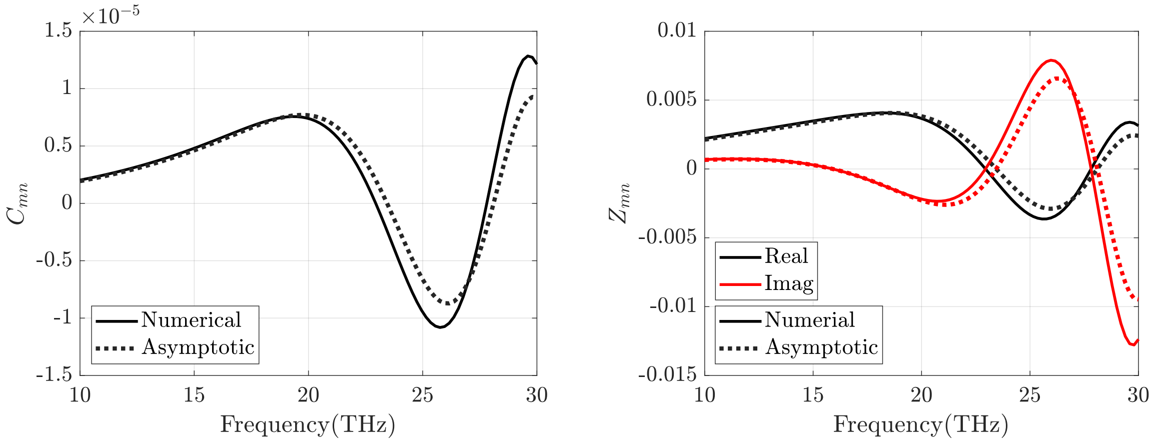

(a) Mutual coupling C_{mn} (b) Mutual impedance Z_{mn}

Figure 5.6: Comparison between numerical and analytical results of mutual coupling for BM1

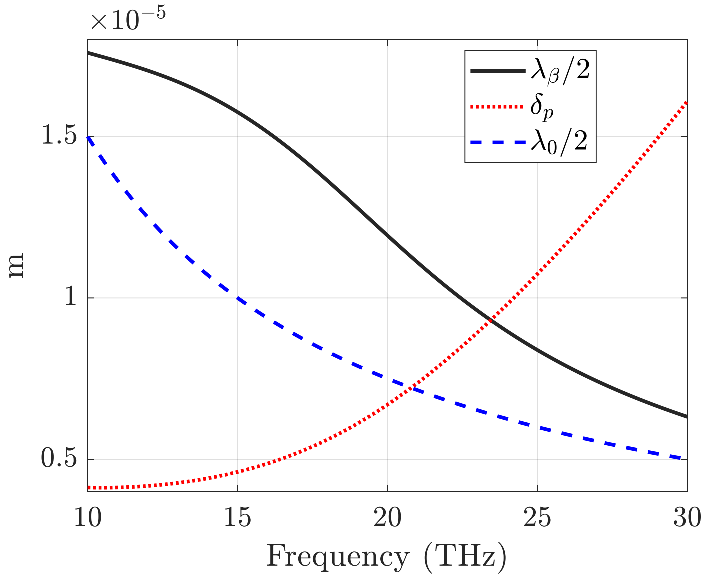

Figure 5.7: Penetration depth, half-wavelength in the dielectric and half-wavelength in free-space for BM1

function ((5.54), (5.55)), are shown in Figure 5.6. The material used in this example is the same bad metal BM1 used in Section 5.1.2 and the distance of the two dipoles is again taken as the penetration depth δ_p of the material, which is shown in Figure 5.7.

As we can see from Figure 5.6 that below 20 THz, the numerical results are well approximated by our analytical expressions. There are some discrepancies at higher frequencies, but the trend of the curves remains identical. The reason accounting for these discrepancies comes from the assumption we took for $pol_{real}^2 \approx 1/\sqrt{\pi}$. Its dependence on the 3 variables may play a more important role on the final result when the frequency becomes higher. Also, for higher frequencies, the numerical results could lack accuracy due to the limitation of the number of points taken in the numerical integration process.

5.2.3. Analysis on the First Null

Nonetheless, as stated in Section 4.3, what is important is the position of the first null in C_{mn}^{pq}. This will be carefully analysed in this section.

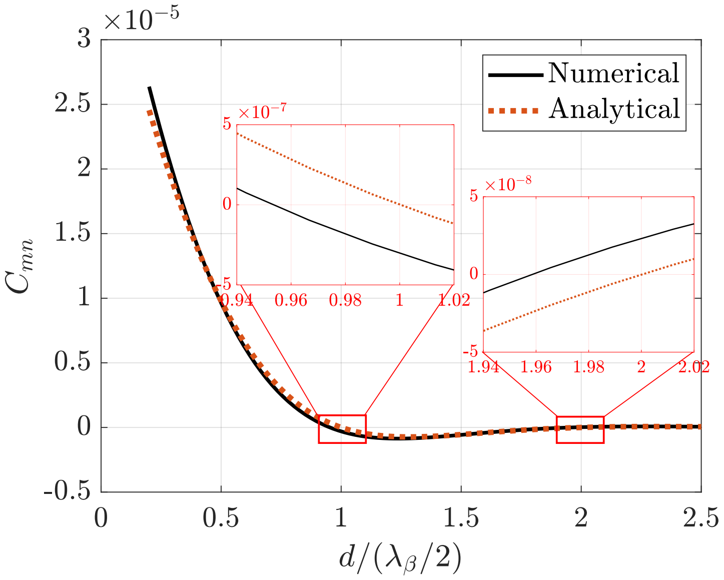

Figure 5.8: Comparison of the position of nulls of analytical and numerical results at 20 THz as a function of distance

Instead of showing C_{mn}^{pq} as a function of frequency, as in Figure 5.6, we now select a certain frequency and plot C_{mn}^{pq} as a function of changing distance d. Figure 5.8 shows an example for the same material BM1 at 20 THz, with distance d normalized by $\lambda_\beta/2$. As suggested by (5.51), for the analytical expression, the nulls should occur at $d/(\lambda_\beta/2)$ equal to a positive integer, such as $1, 2, 3\ldots$. But taking a closer look, we can discover that for the numerical results, the positions of the nulls are not exactly integers as predicted by the analytical expression. In the example in Figure 5.8, the 1st and 2nd null for the numerical results are positioned at around 0.95 and 1.96, which is slightly shifted from the integers predicted by our analytical expression.

Since we are most interested in the first null, which decides the number of degrees of freedom we have in a certain volume, as stated by (4.13), we now focus on the shift from the integers of the first null in the numerical result as a function of frequency. Figure 5.9a shows the changing of the position of the first null calculated by the numerical method for the same material BM1. We can discover that the curve starts around 1 at very low frequencies, then rises to around 1.025 and begins dropping, passing 1 around 15.8 THz. It means that at low frequencies and 15.8 THz, the first null appears exactly at $d = \lambda_\beta/2$, as suggested by our analytical expression.

If we now plot the energy transferred per degree of freedom, as given in (5.11), for the same material BM1, as shown in Figure 5.9b, we can see that it peaks around very low frequencies and 15.8 THz, which is identical to the two frequencies when the first null of the mutual impedance appears exactly at $d = \lambda_\beta/2$. As we can see from Figure 5.9b, at these two frequencies, $E^{1-DoF} \approx k_B T$. Temperature T is taken as 300 Kelvin in this thesis if not

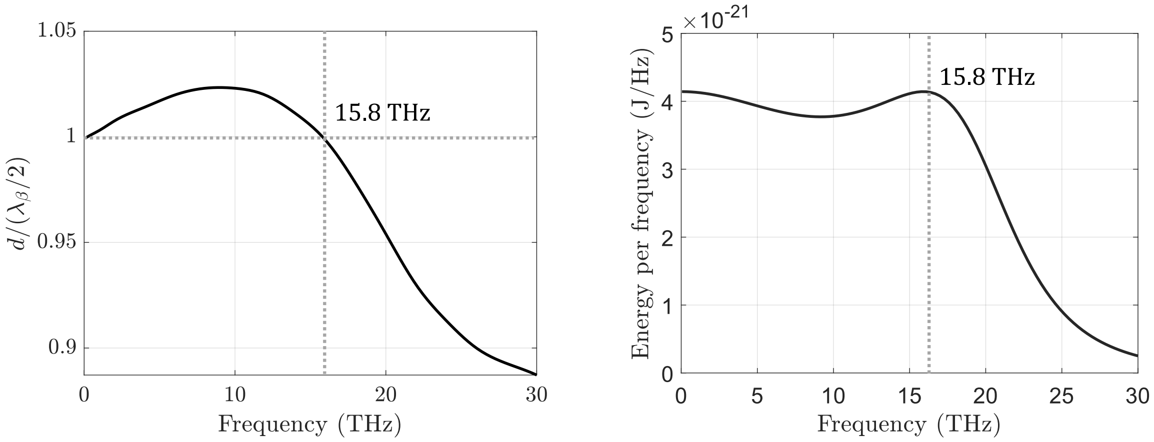

(a) Position of the first null

(b) Estimated energy per degree of freedom

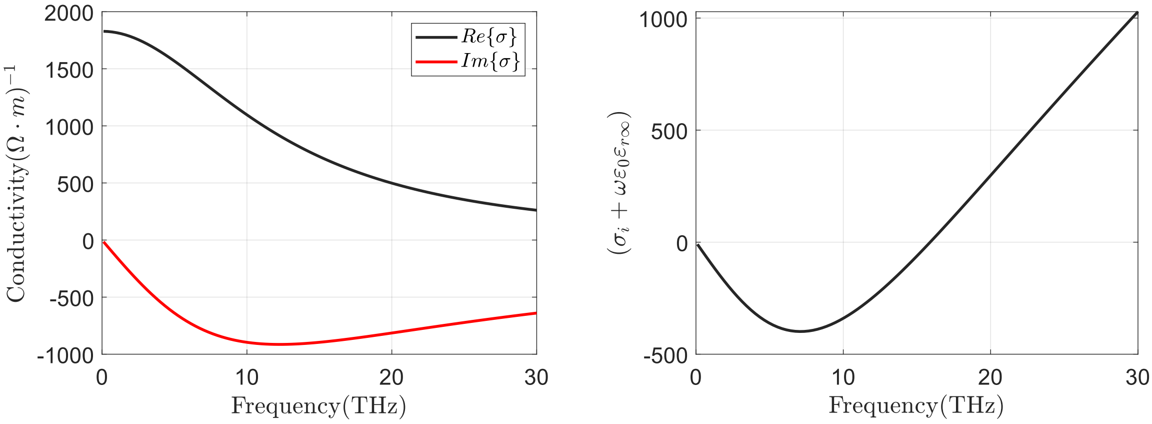

(c) Real and imaginary part of conductivity

(d) $(\sigma_i + \omega\epsilon_0\epsilon_{r\infty})$ in (5.56)

Figure 5.9: Analysis for BM1

specified otherwise. Let's recall that:

$$E^{1-DoF} = \frac{k_B T (R^p)^2}{|Z^p|^2} = k_B T \frac{\sigma_r^2}{\left|\sigma_r - j\sigma_i - j\omega\epsilon_0\epsilon_{r\infty}\right|^2}. \tag{5.56}$$

These two peaks suggest that at these frequencies, the imaginary part inside the absolute bar of the denominator in (5.56), $(\sigma_i + \omega\epsilon_0\epsilon_{r\infty})$, is very small compared with the real part, which results in the curve peaks around $k_B T$, the maximum possible spectral energy one degree of freedom can render. The imaginary part of the conductivity σ_i, defined in (3.3) and shown in Figure 5.9c, is small at low frequencies. Consider that $(\omega\epsilon_0\epsilon_{r\infty})$ is a linear function continuously rising with respect to increasing frequencies. Then $(\sigma_i + \omega\epsilon_0\epsilon_{r\infty})$ is shown in Figure 5.9d, where at very low frequencies and 15.8 THz the value of the curve is 0 as we would expect.

To test our findings, we now propose a new kind of bad metal BM2, whose electron density is $n = 8 \times 10^{24}$ electrons$/m^2$ and scattering time is $\tau = 2 \times 10^{-14}$ s. The position of its first null calculated by the numerical method as a function of frequency and the estimated energy per degree of freedom of BM2 are shown in Figure 5.10a and Figure 5.10b. As we can see from the figures, again, when the nulls appear exactly at $d = \lambda_\beta/2$, the estimated energy per degree of freedom peaks around $k_B T$.

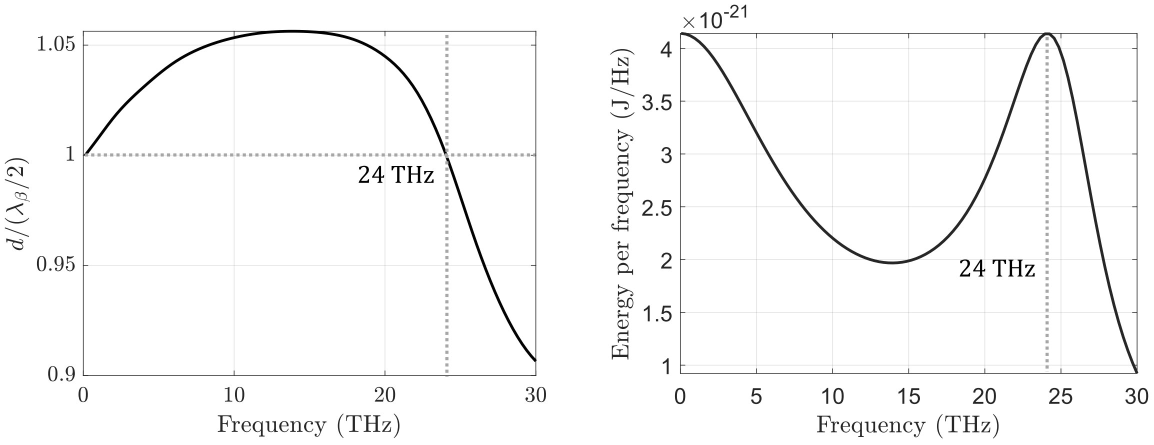

(a) Position of the first null

(b) Estimated energy per degree of freedom

Figure 5.10: Analysis for BM2

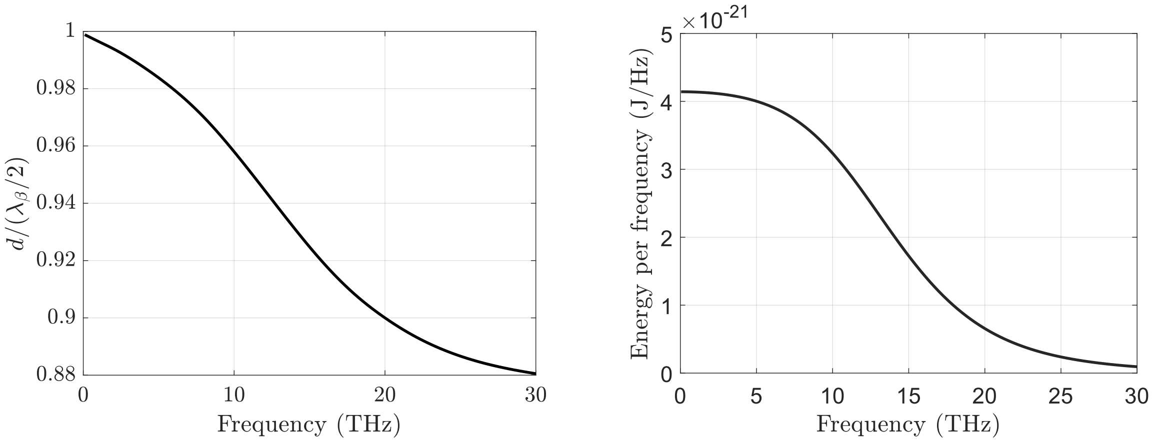

(a) Position of the first null

(b) Estimated energy per degree of freedom

Figure 5.11: Analysis for BM3

We propose another kind of bad metal BM3, whose electron density is $n = 3 \times 10^{24}$ electrons/m^2 and scattering time is $\tau = 8 \times 10^{-15}$ s. The estimated energy per degree of freedom curve of this material, as shown in Figure 5.11b, does not have any peaks. It keeps dropping from $k_B T$ at very low frequencies. Correspondingly, the position of the first null only appears exactly at $d = \lambda_\beta/2$ for very low frequencies and continues to shift towards lower values when frequency increases, as shown in Figure 5.11a.

The two new materials BM2 and BM3 all comply with our discovery for BM1. We can also examine our theory on silicon. A type of silicon (Si1), whose electron density is $n = 8 \times 10^{21}$ is selected. Figure 5.12 to Figure 5.13 shows C_{mn} and Z_{mn} calculated using both analytical and numerical methods as before. Figure 5.12 shows the case when the mutual distance d always equals to the penetration depth δ_p. Figure 5.13 shows the case that the mutual distance d always equals a fixed number $d = 250\mu m$. Figure 5.14 shows the case that C_{mn} is changing as a function of d, which is normalized by $\lambda_\beta/2$, at a fixed frequency of 100 GHz. The results of silicon are all in accordance with our previous discoveries for the bad metals.

Now we are able to conclude that, for ideal lossless homogeneous media, the smallest

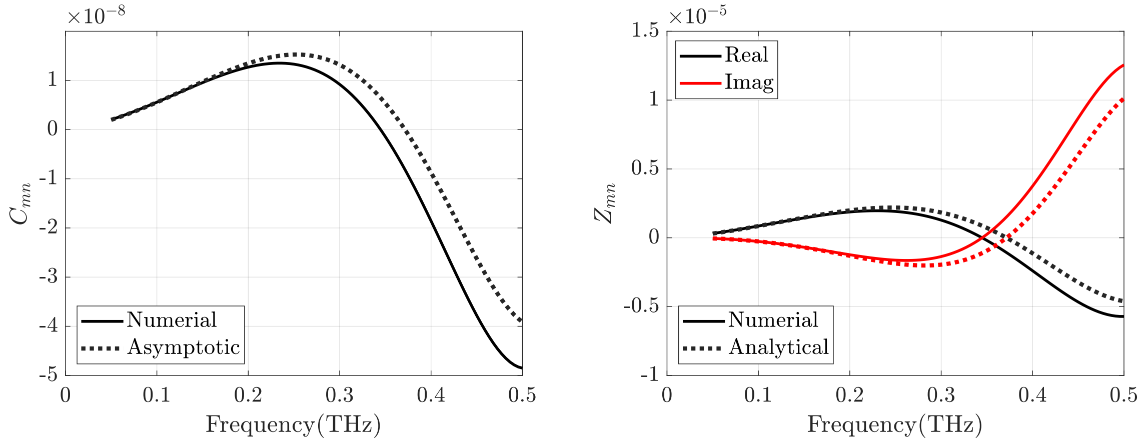

(a) Mutual coupling C_{mn} (b) Mutual impedance Z_{mn}

Figure 5.12: Mutual Coupling for Si1 when $d = \delta_p$

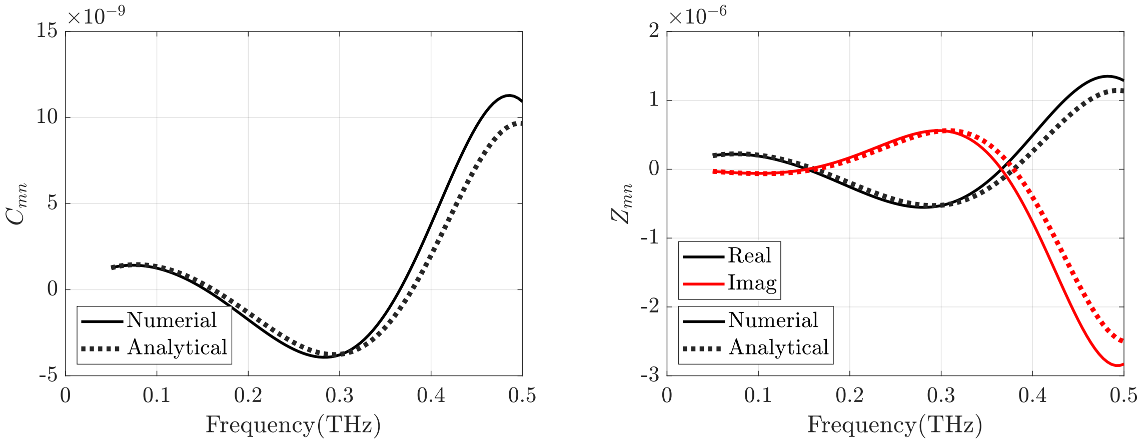

(a) Mutual coupling C_{mn} (b) Mutual impedance Z_{mn}

Figure 5.13: Mutual Coupling for Si1 when $d = 250\mu m$.

distance for two eigenvectors two be uncoupled is exactly $\lambda/2$. But for real dispersive materials, the actual position of the first null of the mutual impedance curve may shift from $\lambda_\beta/2$ depending on the dispersion curve of the material. This shift is not very significant until certain frequencies. So in this case, the smallest distance can still be regarded as $\lambda_\beta/2$.

5.3. Total Energy Available within the Medium

Proceeding (4.14), we can now write the total energy available in a certain volume Vol in an analytical way using (5.11) and (5.53) as:

$$E^{tot} = N_{DoF} \times E^{1-DoF} = \frac{48Vol}{\lambda_\beta^3} \times \frac{k_B T (R^p)^2}{|Z^p|^2} = \frac{48Vol}{\lambda_\beta^3} \frac{k_B T \sigma_r^2}{\left|\sigma_r - j\sigma_i - j\omega\epsilon_0\epsilon_{r\infty}\right|^2}. \tag{5.57}$$

Two examples of (5.57) realized for BM1 and BM3 are shown in Figure 5.15. The volume is taken as a ball with a radius of $100\mu m$. The bend of the curve around 16 THz for BM1 in Figure 5.15a is induced by the second peak of E^{1-DoF} (See Figure 5.9b). While the curve for BM3 (Figure 5.15b) does not have the bend, as its corresponding E^{1-DoF} curve does not

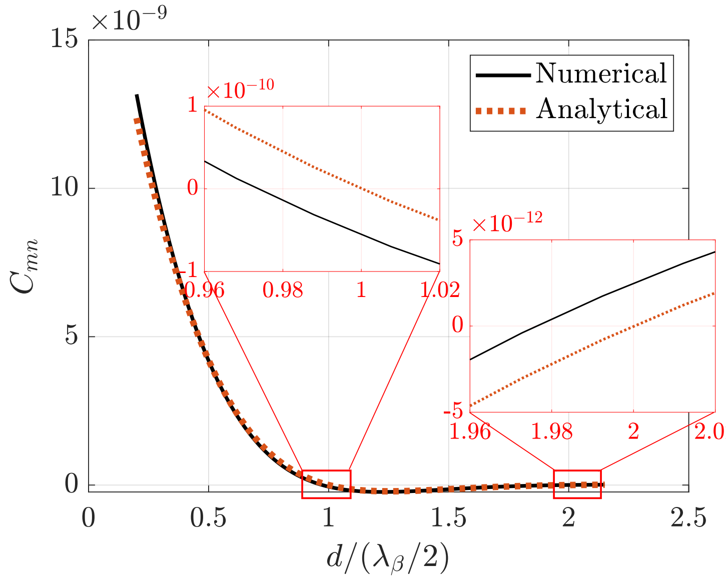

Figure 5.14: Mutual Coupling for Si1 at 100 GHz as a Function of Distance

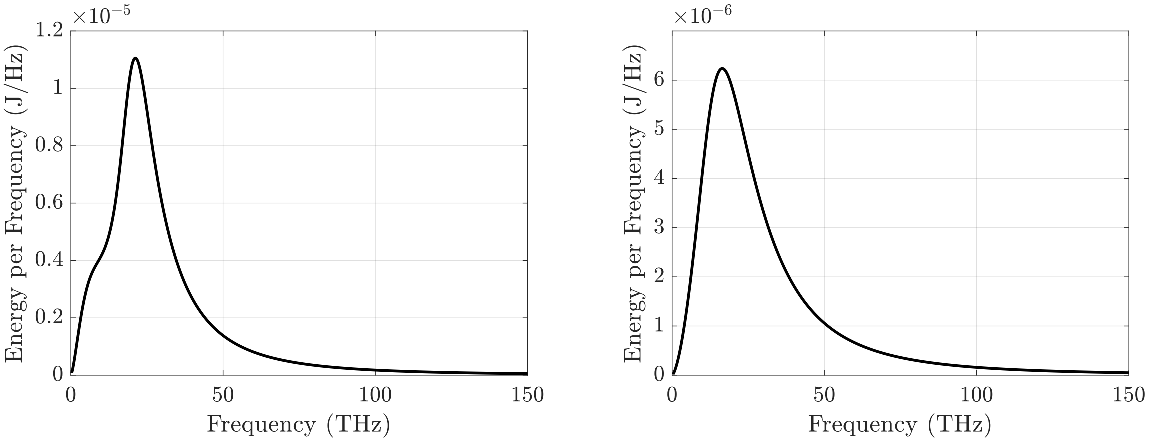

(a) BM1

(b) BM3

Figure 5.15: Total energy available within a certain volume.

have a second peak (See Figure 5.11b). For low frequencies N_{DoF} dominates the rise of the curves with respect to frequency. While for high frequencies the curves decrease because the curves of E^{1-DoF} drop significantly with respect to frequency.

To find out the rate of decrease of the curves for high frequencies, we now derive the high-frequency approximation of E^{1-DoF}. At high frequencies, it can be approximated as:

$$\lim_{f\to\infty} E_{EM}^{1-DoF} \approx k_B T \frac{\lim_{f\to\infty}(R^p)^2}{\lim_{f\to\infty}|Z^p|^2} \approx k_B T \frac{\left(\frac{\sigma_{qs}}{\omega^2\tau^2}\right)^2}{|\omega\varepsilon_0\varepsilon_{r\infty}|^2} \approx k_B T \frac{\sigma_{qs}^2}{(2\pi)^6\,\varepsilon_0^2\varepsilon_{r\infty}^2\tau^4}\frac{1}{f^6}. \tag{5.58}$$

Then the total energy available E^{tot} at high frequencies can be approximated as:

$$\lim_{f\to\infty} E^{tot} \approx \frac{48 Vol\cdot f^3}{\left(c_0\sqrt{\varepsilon_{r\infty}}\right)^3}\times\frac{k_B T\sigma_{qs}^2}{(2\pi)^6\,\varepsilon_0^2\varepsilon_{r\infty}^2\tau^4}\frac{1}{f^6} = \frac{3Vol}{4\left(c_0\sqrt{\varepsilon_{r\infty}}\right)^3}\frac{k_B T\sigma_{qs}^2}{\pi^6\varepsilon_0^2\varepsilon_{r\infty}^2\tau^4}\frac{1}{f^3} \propto \frac{1}{f^3}, \tag{5.59}$$

where c_0 refers to the propagation speed in free space.

Unlike the traditional Rayleigh-Jeans model which continues to rise at high frequencies, the total energy available in our model decreases proportionally to $1/f^3$ at high frequencies (see (5.59)), despite using the classic description of average energy per degree of freedom $k_B T$ as suggested by equipartition theorem. One should always bear in mind that this amount of energy is the energy available within the boundary of the medium. For the case of a real finite object, the amount of energy actually leaving the boundary of the object will be much less than the amount suggested by (5.57) since a large portion of this energy will be absorbed by the object before it reaches to the boundary. This situation will be addressed in detail in the next chapter.

6

Evaluation of Radiated Power

In previous chapters, we only focus on the available energy within in certain volume of ohmic medium. In this proceeding chapter, instead of considering an ideal infinite medium, we will establish a model to estimate the power radiated outside a real finite bulk object.

In this chapter, the generating currents of the eigenvectors are described in Section 6.1. They are defined as volumetric current distributions on small cubes. Then, the possible positions of the finite number of degrees of freedom are discussed in Section 6.2. These possible positions result in a discretization of the bulk object. Then, the power radiated outside the object boundary is calculated in Section 6.3 from the Poynting vectors of these sources. An analytical approximation of this power is given in (6.35), whose credibility is verified by numerical realization in Section 6.6. It turns out that for low frequencies, the result of radiated power from our model is very similar to the traditional method given in (2.6). While for high frequencies, there are some major discrepancies.

6.1. Generating Currents of the Eigenvectors

In Chapter 5, we treat the eigen-currents as elementary dipoles. We can now represent the sources generating these eigenmodes as volumetric current distributions $\vec{j}(\vec{r})$ on small cubes with side lengths equal to Δ, which is very small compared to the wavelength. They can be represented as:

$$\vec{j}(\vec{r}) = \frac{I}{\Delta^2} rect\left(\vec{r}, \Delta^3\right) \cdot \hat{p}, \tag{6.1}$$

where I is the net current, and $\hat{p}$ is the direction of the current, which is orthogonal to the cross-section with an area of Δ^2. For a source located at $\vec{r}_m$, oriented along $\hat{p}$ and with net current I_m^p, the current distribution is:

$$\vec{j}(\vec{r}, \vec{r}_m) = \frac{I_m^p}{\Delta^2} rect\left(\vec{r} - \vec{r}_m, \Delta^3\right) \cdot \hat{p}. \tag{6.2}$$

Extending (4.2) to the generating currents, the total generating current inside the bulk object can be represented as:

$$\vec{j}_{tot}(\vec{r}, \vec{r}_m) = \sum_{m=1}^{N_{DoF}} I_m^p \hat{p} \frac{1}{\Delta^2} rect\left(\vec{r} - \vec{r}_m, \Delta^3\right). \tag{6.3}$$

The current I_m^p in (6.2) and (6.3) can be represent by its amplitude and phase $I_m^p = \left|I_m^p\right| e^{j\phi_m^p}$. The phase ϕ_m^p here is random due to that these currents are non-coherent to each other. The amplitude of the current can be calculated via the Johnson-like circuit introduced in Section 3.2. The load impedance Z_{load} is associated with the load of the surrounding environment of $\vec{r}_m$, which represents the location of that degree of freedom. We can approximate that for every $\vec{r}_m$ in the object, $Z_{load} \approx Z_p$, as if it is in an infinite homogenous medium. This approximation is more accurate for degrees of freedom which are at the inner layers of the bulk object and less accurate for ones near the surface of the object. Using this approximation, the amplitude of each of the generating currents can be approximated as:

$$\left|I_m^p\right|^2 \approx |I_0|^2 = \frac{k_B T R^p}{|Z^p|^2}, \tag{6.4}$$

where $R^p = Re\{Z^p\}$. Z^p is given analytically in (5.10).

6.2. Position of Generating Currents

As we discovered in Chapter 5 that the minimal distance for two eigenmodes to be independent can be approximated by $\frac{\lambda_\beta}{2}$. Thus, the number of degrees of freedom in a certain volume can be calculated by (5.53). However, where these degrees of freedom are actually placed remains a problem. One simple and intuitive solution is to divide the object equally by a grid with the side length of each cube equal to $\frac{\lambda_\beta}{2}$, as shown in Figure 6.1a. The generating sources, as given by (6.2), are then placed at the centre of each cube, $\vec{r}_m$. The number of these centres is just N_{pos} given in (5.53):

$$N_{pos} = \frac{vol}{\left(\frac{\lambda_\beta}{2}\right)^3} = \frac{8vol}{\lambda_\beta^3}. \tag{6.5}$$

Figure 6.1b shows a cross-section of the ball object as given in Figure 6.1a. Since these generating currents are independent of each other, the total power radiated outside the object can be simply calculated by summing up the individual contribution of each degree of freedom. By adopting the approximation in (6.4), we can thus represent the total power as:

$$P_{rad}^{tot}(f) = \sum_{DoF} P_{rad_{1DOF}} = \sum_{m=1}^{N_{pos}} \sum_{p=1}^{Pol.} P_{rad}\left(f, \vec{r}_m, |I_0|^2, \left[\frac{\lambda_\beta}{2}\right]^3\right), \tag{6.6}$$

where $Pol = 6$ represents 6 different possible polarizations.

However, one can always argue that the situation shown in Figure 6.1b is only one possible realization. There is always going to be other different allocations of these sources, for example, the case shown in Figure 6.1c, as the positions of the sources $\vec{r}_{m'}$ are shifted from their previous positions $\vec{r}_m$ in Figure 6.1b. In fact, there is no reason to believe one place is any better than others. Any position inside the object is equally possible for a degree of freedom and its generating source to exist. Acknowledging this fact, one can divide the grid of one degree of freedom (side length equals $\frac{\lambda_\beta}{2}$) into small cubes with a side length of Δ, whose centre can be indicated by $\vec{r}_l$, as shown in Figure 6.2. The generating current associated with this degree of freedom has equal possibilities to be placed at all of these small cubes. In this case, the power radiated outside by each degree of freedom can be

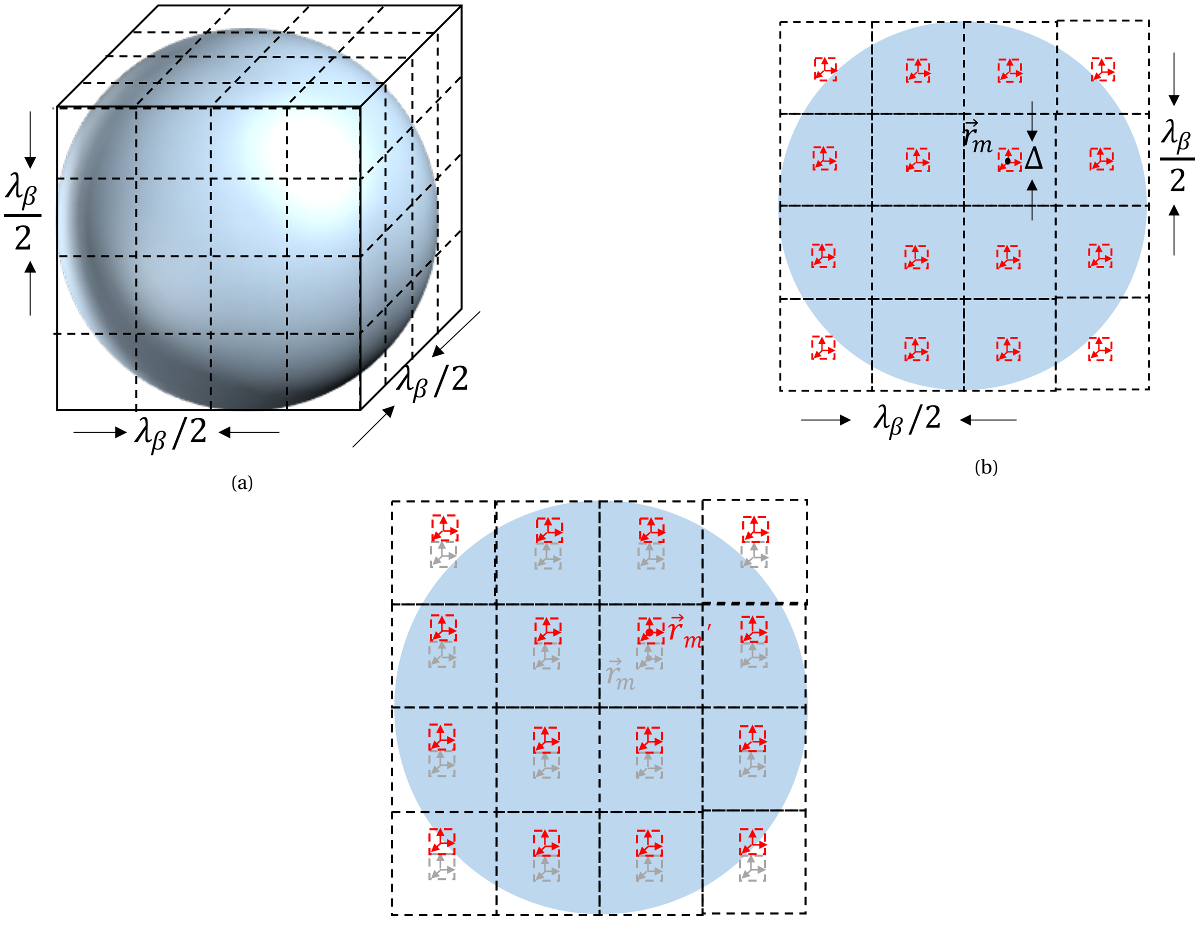

(a)

(b)

(c)

Figure 6.1: (a)Discretization of the bulk object (b)Cross-section in 2D (c)Another possible location of the sources

represented as:

$$P_{rad_{1DOF}} = \frac{1}{L}\sum_{l=1}^{L} P_{rad}\left(f, \vec{r}_l, |I_0|^2, \Delta^3\right), \tag{6.7}$$

where L represents the number of small cubes inside a cube of one degree of freedom:

$$L = \frac{\left(\frac{\lambda_\beta}{2}\right)^3}{\Delta^3} = \frac{\lambda_\beta^3}{8\Delta^3}. \tag{6.8}$$

L here is used as an average factor for the reason that these L small cubes actually represent L possible realizations of the position of the generating source associated to one degree of freedom.

Dividing all degrees of freedom into L sub-cubes and replacing L with (6.8), the total power radiated outside the object can be written as:

$$P_{rad}^{tot}(f) = \frac{1}{L} \times \sum_{DoF}\sum_{l=1}^{L} P_{rad}\left(f, \vec{r}_l, |I_0|^2, \Delta^3\right) = \frac{8\Delta^3}{\lambda_\beta^3} \times \sum_{DoF}\sum_{l=1}^{L} P_{rad}\left(f, \vec{r}_l, |I_0|^2, \Delta^3\right). \tag{6.9}$$

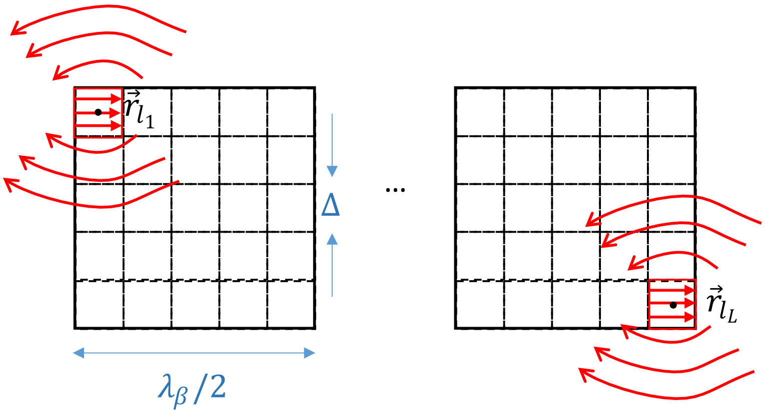

Figure 6.2: Divide the $\lambda_\beta/2$ cube into smaller cubes with side length Δ. This figure only shows the $\hat{x}$ oriented current.

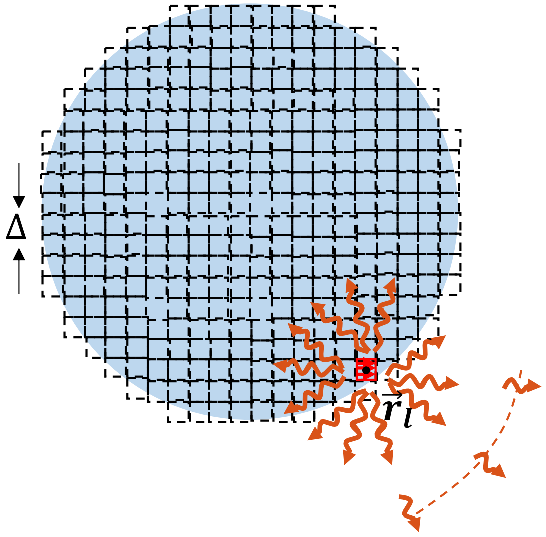

Figure 6.3: Divide the whole bulk object into small cubes. Each of these cubes is a generating source.

We can represent the double summation in (6.9) by a single summation as:

$$P_{rad}^{tot}(f) = \frac{8\Delta^3}{\lambda_\beta^3} \sum_{l=1}^{L\times N_{pos}\times pol} P_{rad}\left(f, \vec{r}_l, |I_0|^2, \Delta^3\right) = 6 \times \frac{8\Delta^3}{\lambda_\beta^3} \sum_{l=1}^{L\times N_{pos}} P_{rad}\left(f, \vec{r}_l, |I_0|^2, \Delta^3\right). \quad (6.10)$$

This is equivalent to the model shown in Figure 6.3. In Figure 6.3, we directly divide the bulk object into $L \times N_{pos}$ number of small cubes with side length Δ. Each of these small cubes is a volumetric generating current source defined as:

$$\vec{j}(\vec{r}, \vec{r}_l) = \frac{I_0}{\Delta^2} rect\left(\vec{r} - \vec{r}_l, \Delta^3\right) \cdot \hat{p}. \quad (6.11)$$

Since these currents are non-coherent, their contribution to the total power radiated outside can be summed up together. Just as a further clarification, one can realize that, firstly, these small cubes represent different possible realizations of the degrees of freedom, thus they are independent of each other. Secondly, all these $L \times N_{pos}$ number of sources cannot exist at the same time, only L number of these sources with a mutual distance of $\frac{\lambda_\beta}{2}$ with the neighbouring source can exist at a certain moment.

6.3. Power Radiated outside

As mentioned before, since these generating currents are non-coherent, their contributions to the total power radiated outside can be summed up together, as illustrated in equation (6.10). To calculate this power, one can integrate the Poynting vectors over the entire surface area (SA) of the bulk object. In the example of Figure 6.1 and 6.3, the object is considered as a ball object. The Poynting vector is defined as the energy flux in a certain direction. Generally, it can be written as [32]:

$$\vec{S} = \vec{e} \times \vec{h}^*. \tag{6.12}$$

We start from the contribution of one of the small volumetric currents of Δ^3 defined by (6.11). The electrical field generated by the volumetric current centred at $\vec{r}_l$ can be calculated as:

$$\vec{e}(\vec{r}) = \iiint_{\Delta^3(\vec{r}_l)} \bar{\bar{g}}^{ej}(\vec{r}, \vec{r}_\Delta) \cdot \vec{j}(\vec{r}_\Delta, \vec{r}_l)\, d\vec{r}_\Delta, \tag{6.13}$$

where $\vec{r}_\Delta$ refers to the points in the source volume $\Delta^3(\vec{r}_l)$ centred at $\vec{r}_l$. If the observation point is very far away from the source volume $\Delta^3(\vec{r}_l)$, we can take $(\vec{r} - \vec{r}_\Delta) \approx (\vec{r} - \vec{r}_l)$. In this way, the Green's function in (6.13) can be approximated as the Green's function at the centre $\vec{r}_l$:

$$\vec{e}(\vec{r}, \vec{r}_l) = \bar{\bar{g}}^{ej}(\vec{r}, \vec{r}_l)\, \Delta I_0 \cdot \hat{p}. \tag{6.14a}$$

Similarly, the magnetic field can be written as:

$$\vec{h}(\vec{r}, \vec{r}_l) = \bar{\bar{g}}^{hj}(\vec{r}, \vec{r}_l)\, \Delta I_0 \cdot \hat{p}. \tag{6.14b}$$

The Poynting vector of a volumetric generating source oriented along $\hat{z}$ centred at $\vec{r}_l$ can be written as:

$$\vec{S}(\vec{r} - \vec{r}_l) = \vec{e}(\vec{r}, \vec{r}_l) \times \vec{h}^*(\vec{r}, \vec{r}_l) = |I_0|^2 \zeta_0 \Delta^2 \frac{1}{\lambda_0^2} \sqrt{\varepsilon_{r,eff}}^{\,*} \frac{\sin^2(\theta - \theta_l)}{4|\vec{r} - \vec{r}_l|^2} e^{-2k_\alpha |\vec{r} - \vec{r}_l|} \frac{\vec{r} - \vec{r}_l}{|\vec{r} - \vec{r}_l|}, \tag{6.15}$$

where θ and θ_l are the $\hat{\theta}$ component of vector $\vec{r}$ and $\vec{r}_l$ in spherical coordinate. The detailed algebraic steps can be found in Appendix D. Then, the spectral power radiated by the source centred at $\vec{r}_l$ outside the ball object can be calculated by integrating all the Poynting vectors that have travelled through the whole surface area SA:

$$P_{rad}\left(f, (\vec{r}_s - \vec{r}_l)\right) = \iint_{SA} \left[1 - \Gamma^2(\vec{r}_s - \vec{r}_l)\right] Re\left\{\vec{S}(\vec{r}_s - \vec{r}_l)\right\} \cdot \hat{n}(\vec{r}_s) d\vec{r}_s, \tag{6.16}$$

where $\vec{r}_s$ are the surface points of the whole object; $\hat{n}(\vec{r}_s)$ is the normal vector of the surface at point $\vec{r}_s$; $\vec{S}(\vec{r}_s - \vec{r}_l)$ is the Poynting vector flowing from the source point of $\vec{r}_l$ to the surface point of $\vec{r}_s$; and $\Gamma^2(\vec{r}_s - \vec{r}_l)$ is the power reflection coefficient between the object medium and its surrounding environment when the Poynting vector $\vec{S}(\vec{r}_s - \vec{r}_l)$ arrives at surface point $\vec{r}_s$. $\Gamma^2(\vec{r}_s - \vec{r}_l)$ can be calculated using the Fresnel equations (details in Section 6.6).

Notice that (6.15) only gives one case of the Poynting vector for the current oriented along $\hat{z}$ direction. The expression varies for currents oriented at different directions. But this specific direction of the source does not contain any useful information, since we are integrating the Poynting vector over the entire surface area and only intersted in the total power radiated by all the sources. Hence, it is convenient to replace the directional sources by isotropic ones. We can then have an expression (detailed derivations see Appendix D) of Poynting vectors for all of the isotropic sources as:

$$\vec{S}_{iso}\left(\vec{r}-\vec{r}_l\right) = |I_{iso}|^2 \zeta_0 \Delta^2 \frac{1}{\lambda_0^2} \sqrt{\varepsilon_{r,eff}}^{*} \frac{1}{4\,|\vec{r}-\vec{r}_l|^2} e^{-2k_\alpha|\vec{r}-\vec{r}_l|} \frac{\vec{r}-\vec{r}_l}{|\vec{r}-\vec{r}_l|}, \tag{6.17}$$

In order to get the same power as the directional sources, i.e. make (6.15) equal to (6.17), the current of the isotropic dipoles should be set as (detailed derivations see Appendix D):

$$|I_{iso}|^2 = \frac{2}{3}|I_0|^2. \tag{6.18}$$

If we define the power transmission coefficient as $T\left(\vec{r}-\vec{r}_l\right) = \left[1-\Gamma^2\left(\vec{r}-\vec{r}_l\right)\right]$, the spectral power radiated by an isotropic source centred at $\vec{r}_l$ outside the whole surface area can then be written as:

$$P_{rad}^{iso}\left(f,\left(\vec{r}_s-\vec{r}_l\right)\right) = \iint_{SA} T\left(\vec{r}_s-\vec{r}_l\right) Re\left\{\vec{S}_{iso}\left(\vec{r}_s-\vec{r}_l\right)\right\} \cdot \hat{n}\left(\vec{r}_s\right) d\vec{r}_s. \tag{6.19}$$

Substitute (6.17) into (6.19):

$$P_{rad}^{iso}\left(f,\left(\vec{r}_s-\vec{r}_l\right)\right) = \frac{1}{6}|I_0|^2 \zeta_0 \Delta^2 \frac{1}{\lambda_0^2} Re\left\{\sqrt{\varepsilon_{r,eff}}\right\} \iint_{SA} T\left(\vec{r}_s-\vec{r}_l\right) \frac{e^{-2k_\alpha|\vec{r}_s-\vec{r}_l|}}{|\vec{r}_s-\vec{r}_l|^2} \frac{\vec{r}_s-\vec{r}_l}{|\vec{r}_s-\vec{r}_l|} \cdot \hat{n}\left(\vec{r}_s\right) d\vec{r}_s. \tag{6.20}$$

Then, substituting (6.20) into (6.10), the total spectral power radiated outside the object by the volumetric source at $\vec{r}_l$ can be written as:

$$\begin{aligned} P_{rad}^{tot}(f) &= \frac{6\times 8\Delta^3}{\lambda_\beta^3}\frac{1}{6}\,|I_0|^2 \zeta_0 \Delta^2 \frac{1}{\lambda_0^2} Re\left\{\sqrt{\varepsilon_{r,eff}}\right\} \sum_{l=1}^{L\times N_{pos}} \iint_{SA} T\left(\vec{r}_s-\vec{r}_l\right) \frac{e^{-2k_\alpha|\vec{r}_s-\vec{r}_l|}}{|\vec{r}_s-\vec{r}_l|^2} \frac{\vec{r}_s-\vec{r}_l}{|\vec{r}_s-\vec{r}_l|} \cdot \hat{n}\left(\vec{r}_s\right) d\vec{r}_s \\ &= \frac{8\Delta^3}{\lambda_\beta^3}\,|I_0|^2 \zeta_0 \Delta^2 \frac{1}{\lambda_0^2} Re\left\{\sqrt{\varepsilon_{r,eff}}\right\} \sum_{l=1}^{L\times N_{pos}} \iint_{SA} T\left(\vec{r}_s-\vec{r}_l\right) \frac{e^{-2k_\alpha|\vec{r}_s-\vec{r}_l|}}{|\vec{r}_s-\vec{r}_l|^2} \frac{\vec{r}_s-\vec{r}_l}{|\vec{r}_s-\vec{r}_l|} \cdot \hat{n}\left(\vec{r}_s\right) d\vec{r}_s. \end{aligned} \tag{6.21}$$

To replace the summation in (6.21) by an integration, we can make an assumption that the power contribution of the source at $\vec{r}_l$ is averagely distributed over the entire source volume of $\Delta^3\left(\vec{r}_l\right)$. In this way, we can approximate the integral in (6.21) as:

$$\begin{aligned} &\iint_{SA} T\left(\vec{r}_s-\vec{r}_l\right) \frac{e^{-2k_\alpha|\vec{r}_s-\vec{r}_l|}}{|\vec{r}_s-\vec{r}_l|} \frac{\vec{r}_s-\vec{r}_l}{|\vec{r}_s-\vec{r}_l|} \cdot \hat{n}\left(\vec{r}_s\right) d\vec{r}_s \\ &\qquad \approx \frac{1}{\Delta^3} \iint_{SA} \iiint_{\Delta^3(\vec{r}_l)} T\left(\vec{r}_s-\vec{r}_\Delta\right) \frac{e^{-2k_\alpha|\vec{r}_s-\vec{r}_\Delta|}}{|\vec{r}_s-\vec{r}_\Delta|^2} \frac{\vec{r}_s-\vec{r}_\Delta}{|\vec{r}_s-\vec{r}_\Delta|} \cdot \hat{n}\left(\vec{r}_s\right) d\vec{r}_\Delta d\vec{r}_s, \end{aligned} \tag{6.22}$$

where $1/\Delta^3$ is the average factor to ensure the unity of the power. From now on, we extend $\vec{r}_l$ to all points within the volume (Vol) of the bulk object. To simplify the notation, we can define a vector pointing from source point to surface point as: $\vec{r}\,' = \left(\vec{r}_s-\vec{r}_l\right)$ and its unit vector $\hat{r}' = \left(\vec{r}_s-\vec{r}_l\right)/|\vec{r}_s-\vec{r}_l|$, which is the direction of the Poyting vector. Then, the summation of all generating sources in (6.21) can be approximated by the integration over the entire volume (Vol) of the bulk object:

$$P_{rad}^{tot}(f) = \frac{8}{\lambda_\beta^3}\,|I_0|^2 \zeta_0 \Delta^2 \frac{1}{\lambda_0^2} Re\left\{\sqrt{\varepsilon_{r,eff}}\right\} \iint_{SA} \iiint_{Vol} T\left(\vec{r}\,'\right) \frac{e^{-2k_\alpha|\vec{r}\,'|}}{|\vec{r}\,'|^2} \vec{r}\,' \cdot \hat{n}\left(\vec{r}_s\right) d\vec{r}_l d\vec{r}_s. \tag{6.23}$$

Equation (6.23) represents the power per frequency radiates outside the bulk object without any significant approximation and can be evaluated numerically, as shall be introduced in Section 6.6.

6.4. Analytical Expression for High Loss Material

For high loss material, we can assume that only the layer close to the surface of the object (i.e. SA) contributes to the flux that actually radiates outside. Then, the integration over the entire volume can be replaced by a ball portion that intersects with the bulk object (blue ball in Figure 6.4). The ball portion is centred at surface point $\vec{r}_s$, with a radius of l, shaded in light green in Figure 6.4:

$$P_{rad}^{tot}(f) = \frac{8}{\lambda_\beta^3}|I_0|^2\zeta_0\Delta^2\frac{1}{\lambda_0^2}Re\left\{\sqrt{\varepsilon_{r,eff}}\right\}\iint_{SA}\int_0^{2\pi}\int_0^{\pi}\int_0^{l} T\left(\vec{r}'\right)\frac{e^{-2k_\alpha|\vec{r}'|}}{|\vec{r}'|^2}\hat{r}'\cdot\hat{n}\left(\vec{r}_s\right) r'^2\sin\theta' dr' d\theta' d\phi' d\vec{r}_s. \tag{6.24}$$

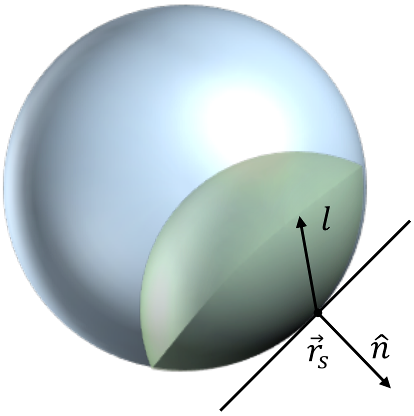

Figure 6.4: Integration over a ball portion (shaded in light green) that intersects with the bulk object (blue ball)

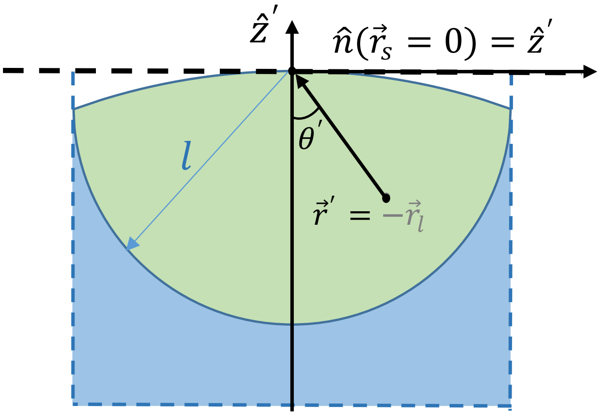

Figure 6.5: Cross-section of Figure 6.4

The cross-section of Figure 6.4 is shown in Figure 6.5. If we place the origin of the coordinate at the surface point $\vec{r}_s$ and consider $\hat{n}(\vec{r}_s) = \hat{z}'$, then we can have:

$$\hat{r}'\cdot\hat{n}\left(\vec{r}_s\right) = \hat{r}'\cdot\left(\hat{z}'\right) = \cos\theta'. \tag{6.25}$$

Then, (6.24) can be reduced to:

$$P_{rad}^{tot}(f) = \frac{8}{\lambda_\beta^3}|I_0|^2\zeta_0\Delta^2\frac{1}{\lambda_0^2}Re\left\{\sqrt{\varepsilon_{r,eff}}\right\}\iint_{SA}\int_0^{2\pi}\int_0^{\pi}\int_0^{l} T\left(\vec{r}'\right)\frac{e^{-2k_\alpha|\vec{r}'|}}{|\vec{r}'|^2}r'^2 dr' \cos\theta'\sin\theta' d\theta' d\phi' d\vec{r}_s. \tag{6.26}$$

Considering the fact that the permittivity of the bulk object and its outside environment are different, not all the fluxes coming from every angle can transmit through the surface. In fact, only the fluxes with angles of incidence smaller than the critic angle θ_c are contributing to the total power radiated out. For angles of incidence larger than θ_c, according to Snell's law, the corresponding angles of refraction are then larger than 90°. In this case, the fluxes will be reflected back within the object. Since we are considering a high loss material, all the multi-reflections within the bulk object are ignored and considered as loss. If the environment surrounding the bulk object has a relative permittivity of $\varepsilon_{r,2}$, the critic angle can be calculated as:

$$\theta_{1c} = \sin^{-1}\left[\frac{\sqrt{\varepsilon_{r,2}}}{Re\left\{\sqrt{\varepsilon_{r,eff}}\right\}}\right]. \tag{6.27}$$

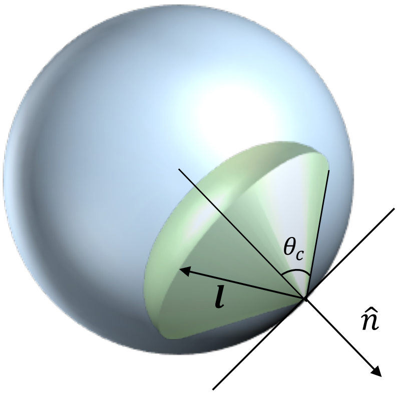

Figure 6.6: Introducing critical angle θ_c, the integration domain is reduced to a volume bounded by a spherical cone (shaded in green).

This critical angle results in the integration domain of the ball portion in Figure 6.4 to be reduced into a volume bounded by a spherical cone, as shaded in light green in Figure 6.6. The total power radiated out can thus be represented as:

$$P_{rad}^{tot}(f) = \frac{8}{\lambda_\beta^3}|I_0|^2\zeta_0\Delta^2\frac{1}{\lambda_0^2}Re\left\{\sqrt{\varepsilon_{r,eff}}\right\}\iint_{SA}\int_0^{2\pi}\int_0^{\theta_c}\int_0^{l} T\left(\vec{r}'\right)e^{-2k_\alpha r'} dr' \cos\theta'\sin\theta' d\theta' d\phi' d\vec{r}_s \tag{6.28}$$

To simplify the integral, we can assume that the transmission coefficient is always equal to the broadside case for all angles of incidence smaller than the critical angle θ_c, and equal to zero for other angles:

$$T\left(\vec{r}'\right) \approx T\left(\theta'=0, \phi'=0\right) rect\left(\theta', \theta_c\right). \tag{6.29}$$

Then, the transmission coefficient is independent of $\vec{r}'$ and can be pulled out of the integral as:

$$P_{rad}^{tot}(f) = \frac{8}{\lambda_\beta^3}|I_0|^2\zeta_0\Delta^2\frac{1}{\lambda_0^2}Re\left\{\sqrt{\varepsilon_{r,eff}}\right\}T(0)\iint_{SA}\int_0^{2\pi}\int_0^{\theta_c}\int_0^l e^{-2k_\alpha r'}dr' \cos\theta'\sin\theta' d\theta' d\phi' d\vec{r}_s \tag{6.30}$$

The integrals in (6.30) can be closed respectively as:

$$\int_0^{2\pi} d\phi' = 2\pi, \tag{6.31a}$$

$$\int_0^{\theta_c}\cos\theta'\sin\theta' d\theta\prime = \frac{1}{2}\sin^2\theta_c, \tag{6.31b}$$

$$\int_0^l e^{-2k_\alpha r}dr = \frac{1-e^{-2k_\alpha l}}{2k_\alpha}, \tag{6.31c}$$

$$\iint_{SA} d\vec{r}_s = SA. \tag{6.31d}$$

Substituting (6.31), (6.30) can be expressed analytically as:

$$P_{rad}^{tot}(f) = \frac{4}{\lambda_\beta^3}|I_0|^2\zeta_0\Delta^2\frac{1}{\lambda_0^2}Re\left\{\sqrt{\varepsilon_{r,eff}}\right\}T(0)\pi\sin^2\theta_c\frac{1-e^{-2k_\alpha l}}{k_\alpha}SA. \tag{6.32}$$

Notice that we can approximate $\sin^2\theta_c$ as:

$$\sin^2\theta_c = \sin^2\left(\sin^{-1}\left[\frac{\sqrt{\varepsilon_{r,2}}}{Re\left\{\sqrt{\varepsilon_{r,eff}}\right\}}\right]\right) \approx \frac{\varepsilon_{r,2}}{Re^2\left\{\sqrt{\varepsilon_{r,eff}}\right\}}. \tag{6.33}$$

Then, the total power radiated outside can be written as:

$$P_{rad}^{tot}(f) = \frac{4}{\lambda_\beta^3}|I_0|^2\zeta_0\Delta^2\frac{1}{\lambda_0^2}T(0)\pi\frac{\varepsilon_{r,2}}{Re\left\{\sqrt{\varepsilon_{r,eff}}\right\}}\frac{1-e^{-2k_\alpha l}}{k_\alpha}SA. \tag{6.34}$$

If the medium surrounding the bulk object is free space, $\varepsilon_{r,2} = 1$, (6.34) is reduced to:

$$P_{rad}^{tot}(f) = \frac{4}{\lambda_\beta^3}|I_0|^2\zeta_0\Delta^2\frac{1}{\lambda_0^2}T(0)\pi\frac{1}{Re\left\{\sqrt{\varepsilon_{r,eff}}\right\}}\frac{1-e^{-2k_\alpha l}}{k_\alpha}SA. \tag{6.35}$$

Equation (6.35) is the analytical expression to calculate the power per frequency radiated by a real lossy material object, with $|I_0|^2$ defined in (6.4).

We can now evaluate (6.35) (referred to as **EM** in the figures) on real materials and compare it with the Planck-like expression (2.6) (referred to as **Planck** in the figures) calculated using the brightness of black body. Figure 6.7 shows the curves of a bad metal (BM4) with $n = 4.7 \times 10^{23}$ electrons$/m^2$ and $\tau = 12fs$. The bulk object is a ball with a radius of $R_S = 100\ \mu\ m$. The surface area SA can be calculated as $SA = 4\pi\ R_S^2$. As we can see from the figure, at low frequencies, the two curves are more or less comparable. Especially for the zoomed-in figure, at frequencies below 0.2 THz, the two curves are overlapping.

The same comparison can also be made for silicon. Consider the bulk object of the same size made of a type of silicon (Si2) with $n = 10^{22}$ electrons$/m^2$. The results are shown in Figure 6.8. It is obvious that the peak of our model (EM) is one magnitude lower than the Planck-like curve in (2.6). And the peak also appears at a lower frequency than the Planck-like curve. Same to the bad metal case, the two curves are overlapping at low frequencies, as can be seen in the zoomed-in figure on the left.

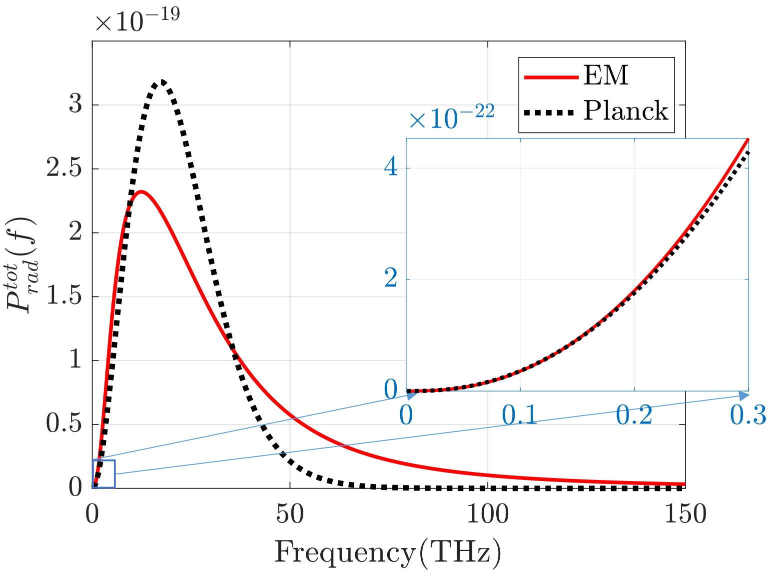

Figure 6.7: Evaluation of (6.35) **EM** and (2.6) **Plank** on BM4

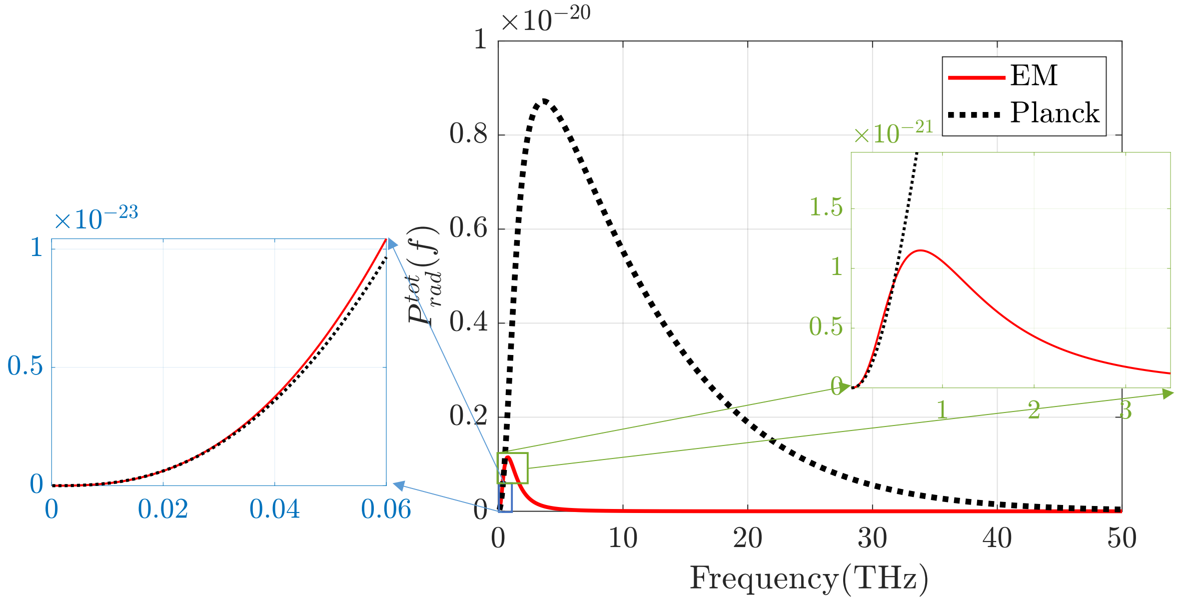

Figure 6.8: Evaluation of (6.35) **EM** and (2.6) **Plank** on Si2

6.5. Approximation for Very Low Frequencies

In the previous section, we have discovered that for low frequencies, our model (6.35) overlaps with the Planck-like curve in (2.6). We now try to simplify (6.35) for every low frequencies and compare it with (A.11), the low-frequency approximation of the Planck-like curve that uses Rayleigh-Jeans law as black body brightness.

For every low frequencies, the real and imaginary part of the propagation constant can be approximated as equal:

$$k_\alpha \approx k_\beta = k_0 Re\left\{\sqrt{\epsilon_{r1}}\right\} = k_0 Re\left\{\sqrt{1 - \frac{j\sigma}{\omega\epsilon_0}}\right\} = k_0\, 0.707\sqrt{\frac{\sigma_{qs}}{\omega\epsilon_0}}. \tag{6.36}$$

Then the self-impedance of one degree of freedom given in (5.10) can be approximated as:

$$Z_p \approx \left(\sigma^* - j\omega\epsilon_0\epsilon_{r\infty}\right)\frac{\Delta^2}{\lambda_0^2}\,\zeta_0^2\frac{\pi}{3k_0\,0.707\sqrt{\frac{\sigma_{qs}}{\omega\epsilon_0}}}. \tag{6.37}$$

Notice that, for the frequency-dependent term inside the bracket, at low frequencies $j\omega\epsilon_0\epsilon_{r\infty}$ is very small and conductivity σ can be approximated by its quasi-static part σ_{qs} given by (3.2), which is purely real. Thus, (6.37) can be reduced to:

$$Z^p \approx \sigma_{qs}\frac{\Delta^2}{\lambda_0^2}\,\zeta_0^2\frac{\pi}{3k_0\,0.707\sqrt{\frac{\sigma_{qs}}{\omega\epsilon_0}}}. \tag{6.38}$$

Replace k_0 with $\frac{2\pi}{\lambda_0}$, (6.38) can be further reduced to:

$$Z^p \approx \sigma_{qs}\frac{\Delta^2}{\lambda_0}\,\zeta_0^2\frac{1}{6\times 0.707\sqrt{\frac{\sigma_{qs}}{\omega\epsilon_0}}}. \tag{6.39}$$

Notice that in (6.39) Z^p is purely real at low frequencies. The amplitude of the current given by (6.4) is then:

$$|I_0|^2 = \frac{k_B T R^p}{|Z^p|^2} = \frac{k_B T}{Z^p} = \frac{k_B T\lambda_0}{\sigma_{qs}\Delta^2\,\zeta_0^2}6\times 0.707\sqrt{\frac{\sigma_{qs}}{\omega\epsilon_0}}. \tag{6.40}$$

Then, substitute (6.40) into (6.35) and use the approximation in (6.36):

$$\begin{aligned} P_{rad}^{tot}(f) &= \frac{4}{\lambda_\beta^3}\frac{k_B T\lambda_0}{\sigma_{qs}\,\zeta_0}6\times 0.707\sqrt{\frac{\sigma_{qs}}{\omega\epsilon_0}}\frac{1}{\lambda_0^2}T(0)\,\pi\frac{1}{0.707\sqrt{\frac{\sigma_{qs}}{\omega\epsilon_0}}}\frac{1-e^{-2k_\alpha l}}{k_0\,0.707\sqrt{\frac{\sigma_{qs}}{\omega\epsilon_0}}}\,SA \\ &= \frac{24}{\lambda_\beta^3}\frac{k_B T}{\sigma_{qs}\,\zeta_0}\frac{1}{\lambda_0}T(0)\,\pi\frac{1-e^{-2k_\alpha l}}{k_0\,0.707\sqrt{\frac{\sigma_{qs}}{\omega\epsilon_0}}}\,SA \\ &= \frac{12}{\lambda_\beta^3}\frac{k_B T}{\sigma_{qs}\,\zeta_0}T(0)\,\frac{1-e^{-2k_\alpha l}}{0.707\sqrt{\frac{\sigma_{qs}}{\omega\epsilon_0}}}\,SA. \end{aligned} \tag{6.41}$$

Using (6.36), at low frequencies, $\frac{1}{\lambda_\beta^3}$ in (6.41) can also be approximated as:

$$\frac{1}{\lambda_\beta^3} \approx \frac{\left[0.707\sqrt{\frac{\sigma_{qs}}{\omega\epsilon_0}}\right]^3}{\lambda_0^3}. \tag{6.42}$$

Substitute (6.42) into (6.41):

$$\begin{aligned} P_{rad}^{tot}(f) &= 12\frac{\left[0.707\sqrt{\frac{\sigma_{qs}}{\omega\epsilon_0}}\right]^3}{\lambda_0^3}\frac{k_B T}{\sigma_{qs}\,\zeta_0}T(0)\,\frac{1-e^{-2k_\alpha l}}{0.707\sqrt{\frac{\sigma_{qs}}{\omega\epsilon_0}}}\,SA \\ &= 12\frac{\left[0.707\sqrt{\frac{\sigma_{qs}}{\omega\epsilon_0}}\right]^2}{\lambda_0^3}\frac{k_B T}{\sigma_{qs}\,\zeta_0}T(0)\left(1-e^{-2k_\alpha l}\right)\,SA \\ &\approx \frac{k_B T}{\lambda_0^3\omega\epsilon_0}\frac{6}{\zeta_0}T(0)\left(1-e^{-2k_\alpha l}\right)\,SA. \end{aligned} \tag{6.43}$$

Notice that $\zeta_0 = \sqrt{\frac{\mu_0}{\epsilon_0}}$, $\omega = \frac{2\pi c_0}{\lambda_0}$ and $c_0 = \frac{1}{\sqrt{\mu_0 \epsilon_0}}$, (6.43) can be simplified as:

$$\begin{aligned} P_{rad}^{tot}(f) &= \frac{k_B T}{\lambda_0^3 2\pi \frac{c_0}{\lambda_0} \epsilon_0} \frac{6}{\sqrt{\frac{\mu_0}{\epsilon_0}}} T(0) \left(1 - e^{-2k_\alpha l}\right) SA \\ &\approx \frac{k_B T}{\lambda_0^3 \frac{c_0}{\lambda_0} \epsilon_0} \frac{1}{\sqrt{\frac{\mu_0}{\epsilon_0}}} T(0) \left(1 - e^{-2k_\alpha l}\right) SA \\ &= \frac{k_B T}{\lambda_0^2 \frac{1}{\sqrt{\mu_0 \epsilon_0}}} \frac{1}{\sqrt{\mu_0 \epsilon_0}} T(0) \left(1 - e^{-2k_\alpha l}\right) SA \\ &= \frac{k_B T}{\lambda_0^2} T(0) \left(1 - e^{-2k_\alpha l}\right) SA \\ &= \frac{k_B T f^2}{c_0^2} \left[1 - |\Gamma(0)|^2\right] \left(1 - e^{-2k_\alpha l}\right) SA. \end{aligned} \tag{6.44}$$

Here, comparing (6.44) with the results calculated by Bekefi [20] in (A.11) we can discover that they are very similar.

6.6. Numerical Validation

As mentioned before, Equation 6.23 represents the power per frequency that radiates outside the bulk object without any significant approximation and can be evaluated numerically. Consider the same ball bulk object with a radius of R_s. It can be represented by the spherical coordinate system as shown in Figure 6.9. This representation divides the object into small portions with the volume of $dr_l \times d\theta_l \times d\phi_l$, which represents each source point. Similarly, the surface area (SA) can also be divided into small portions of spheres $d\Theta_s \times d\Phi_s$ when the radial distance equals the radius of the ball R_s as shown in Figure 6.10. Then, (6.23) can be represented as the summation of every source point in the whole volume through every surface point, as given in (6.45):

$$\begin{aligned} P_{rad}^{tot}(f) = \frac{8}{\lambda_\beta^3} & |I_0|^2 \zeta_0 \Delta^2 \frac{1}{\lambda_0^2} Re\left\{\sqrt{\varepsilon_{r,eff}}\right\} \\ & \sum_0^{2\pi}\sum_0^{\pi}\sum_0^{2\pi}\sum_0^{\pi}\sum_0^{R_s} T\left(\vec{r}'\right) \frac{e^{-2k_\alpha |\vec{r}'|}}{|\vec{r}'|^2} \hat{r}' \cdot \hat{n}\left(\vec{r}_s\right) r_l^2 \sin\theta_l dr_l d\theta_l d\phi_l R_s^2 \sin\Theta_s d\Theta_s d\Phi_s. \end{aligned} \tag{6.45}$$

Figure 6.11 gives a pictorial representation of (6.45). Notice that in (6.45), $|I_0|^2$ can be calculated by (6.4) and the normal vector $\hat{n}(\vec{r}_s)$ at $\vec{r}_s$ is equivalent to the unit radial vector of the point $\vec{r}_s$:

$$\hat{n}(\vec{r}_s) = \hat{R}_s. \tag{6.46}$$

Thus, (6.45) can be written in a more explicit way:

$$\begin{aligned} P_{rad}^{tot}(f) = \frac{8}{\lambda_\beta^3} & \frac{k_B T R^p}{|Z^p|^2} \zeta_0 \Delta^2 \frac{1}{\lambda_0^2} Re\left\{\sqrt{\varepsilon_{r,eff}}\right\} \\ & \sum_0^{2\pi}\sum_0^{\pi}\sum_0^{2\pi}\sum_0^{\pi}\sum_0^{R_s} T\left(\vec{r}'\right) \frac{e^{-2k_\alpha |\vec{r}'|}}{|\vec{r}'|^2} \hat{r}' \cdot \hat{R}_s r_l^2 \sin\theta_l dr_l d\theta_l d\phi_l R_s^2 \sin\Theta_s d\Theta_s d\Phi_s. \end{aligned} \tag{6.47}$$

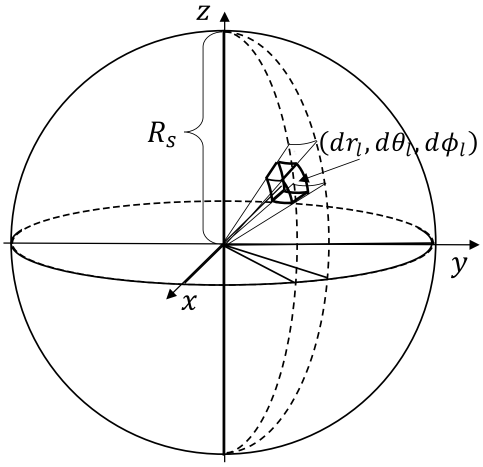

Figure 6.9: Spherical coordinate.

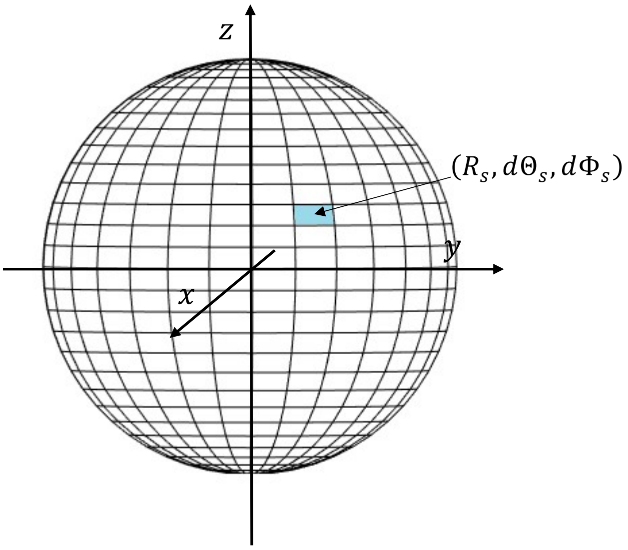

Figure 6.10: Portion of spheres $d\Theta_s \times d\Phi_s$.

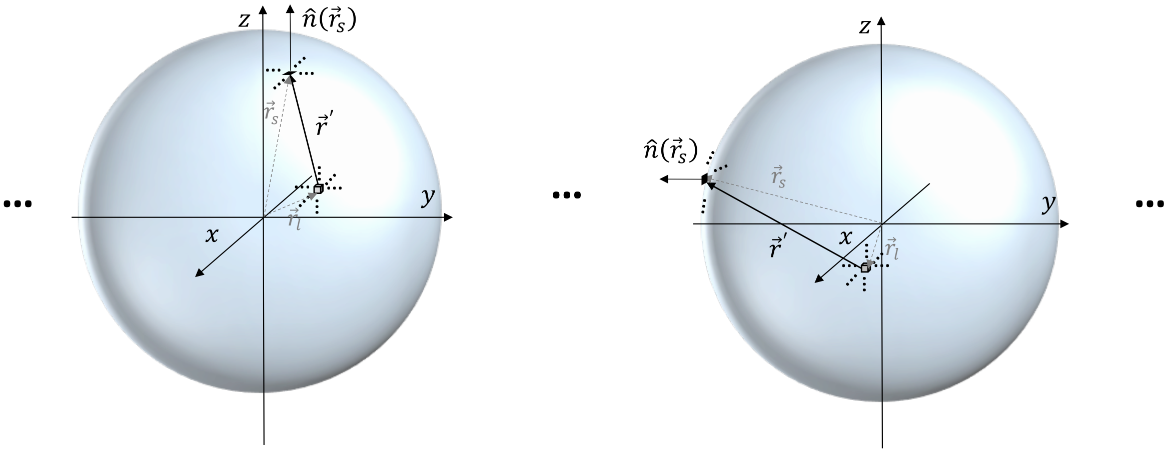

Figure 6.11: A pictorial representation of the numerical calculation (6.45).

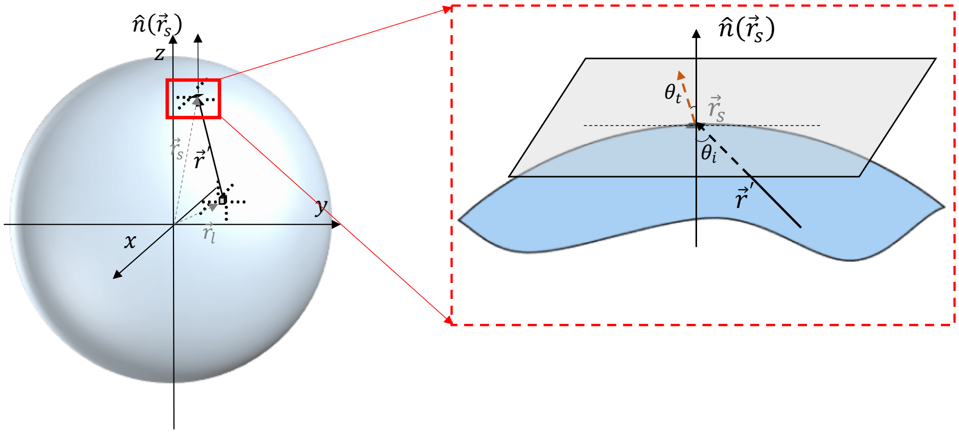

Figure 6.12: Transmission of Poyniting vectors at the surface of the bulk object.

The transmission coefficient in (6.47) can be calculated using Fresnel equations. Figure 6.12 shows a zoomed-in picture around the surface point $\vec{r}_s$. First, the angle of incidence θ_i is the angle between vector $\vec{r}'$ and the normal vector $\hat{n}(\vec{r}_s)$ and can be calculated as:

$$\theta_i = \cos^{-1}\left(\frac{\vec{r}' \cdot \hat{n}}{|\vec{r}'|}\right). \tag{6.48}$$

Then, using Snell's law, the angle of refraction θ_t can be calculated as:

$$\theta_t = \sin^{-1}\left(\frac{Re\left\{\sqrt{\varepsilon_{r,eff}}\right\}}{\sqrt{\varepsilon_{r,2}}}\sin\theta_i\right), \tag{6.49}$$

where $\varepsilon_{r,eff}$ is the effective permittivity of the material of the object, and $\varepsilon_{r,eff}$ is the effective permittivity of its surrounding environment. Consider the surrounding environment as free space, then $\varepsilon_{r,2} = 1$. Fresnel equations for electromagnetic power with TM (indicated as parallel ∥) and TE (indicated as perpendicular ⊥) polarization are given as:

$$\left|\Gamma^{\parallel}\right|^2 = \left|\frac{\zeta_0\cos\theta_t - \zeta_d\cos\theta_i}{\zeta_0\cos\theta_t + \zeta_d\cos\theta_i}\right|^2, \tag{6.50a}$$

$$\left|\Gamma^{\perp}\right|^2 = \left|\frac{\zeta_0 cos\theta_i - \zeta_d cos\theta_t}{\zeta_0 cos\theta_i + \zeta_d cos\theta_t}\right|^2, \tag{6.50b}$$

where ζ_0 is free space impedance and ζ_d is the impedance in the bulk object given as $\zeta_d = \frac{\zeta_0}{\sqrt{\varepsilon_{r,eff}}}$. Then, the power transmission coefficient can be expressed respectively as:

$$T^{\parallel} = 1 - \left|\Gamma^{\parallel}\right|^2, \tag{6.51a}$$

$$T^{\perp} = 1 - \left|\Gamma^{\perp}\right|^2. \tag{6.51b}$$

Considering the fact that our equivalent source is unpolarized and isotropic, we can define an effective power transmission coefficient as the average of the transmission coefficient for the two polarizations.

$$T_{eff} = \frac{1}{2}\left(T^{\parallel} + T^{\perp}\right). \tag{6.52}$$

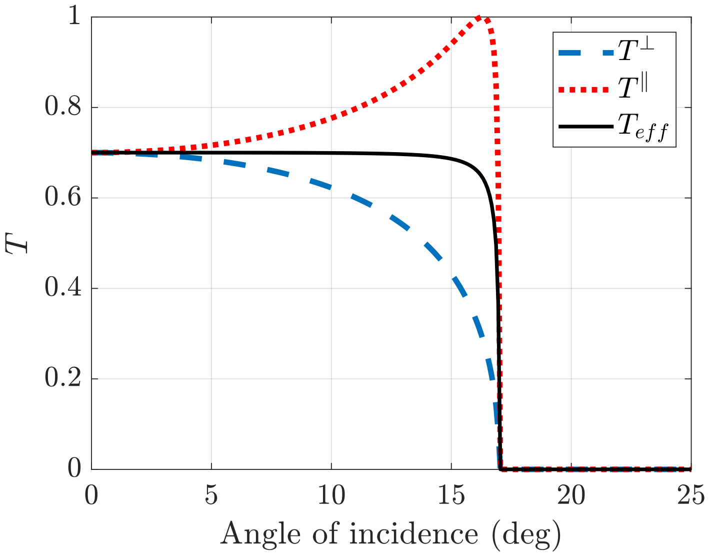

Figure 6.13: An example of T_{eff} compared with $T^{\parallel}$ and $T^{\perp}$.

Figure 6.13 gives an example of comparison between $T^{\perp}$, $T^{\parallel}$ and T_{eff}, for the bulk object with an ideal relative permittivity equal to 11.7. As we can see from the figure, the critical angle θ_c here is 17°. For angles of incidence larger than θ_c, the transmission coefficient equals to zero. Also, for $\theta_i < \theta_c$, T_{eff} is not far away from the transmission coefficient at the broadside. So (6.29) can serve as a good approximation for most of the cases.

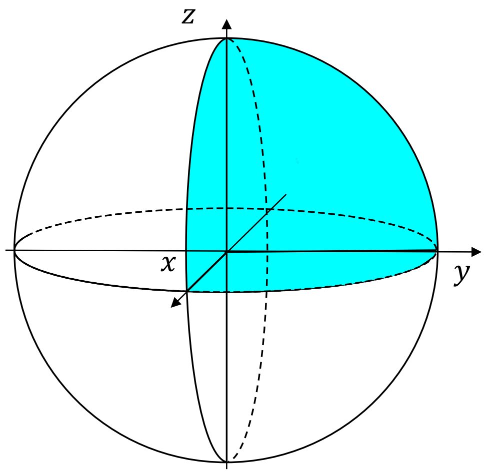

Figure 6.14: An example of 1/8 of the ball volume.

The numerical evaluation process of (6.47) is extremely time and resource-consuming, especially for the size of the bulk object much larger than the wavelength, $R_s \gg \lambda_\beta$. We can utilize the symmetry of the ball-shaped object to speed up the calculation process. It is clear that for the isotropic source, the Poynting vectors radiating from every source in the whole volume through every 1/8 of the surface area are the same. Equivalently, the Poynting vectors radiating from sources in every 1/8 of the volume through the whole surface area are the same. Figure 6.14 gives an example of 1/8 of the ball volume. Originally in

(6.47), the range of the variables are:

$$Sources = \begin{cases} r_l \in [0, R_s], \\ \theta_l \in [0, \pi], \\ \phi_l \in [0, 2\pi]. \end{cases} \quad \text{and,} \; Surface = \begin{cases} R_s, \\ \Theta_s \in [0, \pi], \\ \Phi_s \in [0, 2\pi]. \end{cases} \tag{6.53}$$

Using this symmetry, we can calculate the 1/8 of the total energy radiated out $P_{rad}^{1/8}(f)$ by taking the range of the surface variables as:

$$Surface = \begin{cases} R_s, \\ \Theta_s \in [0, \pi/2], \\ \Phi_s \in [0, \pi/2]. \end{cases} \tag{6.54a}$$

or equivalently changing the range of the source variables as:

$$Sources = \begin{cases} r_l \in [0, R_s], \\ \theta_l \in [0, \pi/2], \\ \phi_l \in [0, \pi/2]. \end{cases} \tag{6.54b}$$

Intuitively, the total power radiated out can be simply calculated as:

$$P_{rad}^{tot}(f) = 8 \times P_{rad}^{1/8}(f). \tag{6.54c}$$

Then (6.47) can be expressed as:

$$P_{rad}^{tot}(f) = \frac{64}{\lambda_\beta^3} \frac{k_B T R^p}{|Z^p|^2} \zeta_0 \Delta^2 \frac{1}{\lambda_0^2} Re\left\{\sqrt{\varepsilon_{r,eff}}\right\}$$
$$\sum_0^{\pi/2} \sum_0^{\pi/2} \sum_0^{2\pi} \sum_0^{\pi} \sum_0^{R_s} T_{eff}(\vec{r}\,') \frac{e^{-2k_\alpha |\vec{r}\,'|}}{|\vec{r}\,'|^2} \hat{r}' \cdot \hat{R}_s r_l^2 \sin\theta_l dr_l d\theta_l d\phi_l R_s^2 \sin\Theta_s d\Theta_s d\Phi_s. \tag{6.55a}$$

Or equivalently:

$$P_{rad}^{tot}(f) = \frac{64}{\lambda_\beta^3} \frac{k_B T R^p}{|Z^p|^2} \zeta_0 \Delta^2 \frac{1}{\lambda_0^2} Re\left\{\sqrt{\varepsilon_{r,eff}}\right\}$$
$$\sum_0^{2\pi} \sum_0^{\pi} \sum_0^{\pi/2} \sum_0^{\pi/2} \sum_0^{R_s} T_{eff}(\vec{r}\,') \frac{e^{-2k_\alpha |\vec{r}\,'|}}{|\vec{r}\,'|^2} \hat{r}' \cdot \hat{R}_s r_l^2 \sin\theta_l dr_l d\theta_l d\phi_l R_s^2 \sin\Theta_s d\Theta_s d\Phi_s \tag{6.55b}$$

Using (6.55a) or (6.55b) we can evaluate (6.23) in a numerical way. We can then compare the results with the analytical approximation we derived at (6.35).

6.6.1. Validation Results

We can test the numerical results of two bulk objects of the same size and the same material as in Section 6.4. The results of BM4 is shown in Figure 6.15, with the numerical result indicated as **EM**(Num), the analytical approximation in (6.35) indicated as **EM**(Analy) and the Planck-like expression (2.6) indicated as **Planck**. As we can see from the figure, the analytical and numerical results show good agreement with each other over low frequencies. For higher frequencies, there are some slight differences between analytical and numerical results. Similar behaviour can also be seen in the results of Si2 in Figure 6.16. The numerical result also shows some discrepancies with the analytical one, especially around the peak of the curves, as can be seen in the zoomed-in figure.

Notice that the frequency range of the numerical calculation is limited due to the fact that the wavelength is getting smaller with respect to the increase of frequency. In order to achieve the same level of accuracy in point sampling ($dr_l = \lambda_\beta/100$ for example), the number of points taken in the object of the same size increases exponentially with respect to frequency. Thus the frequency range for the numerical calculation is limited by the computation resources.

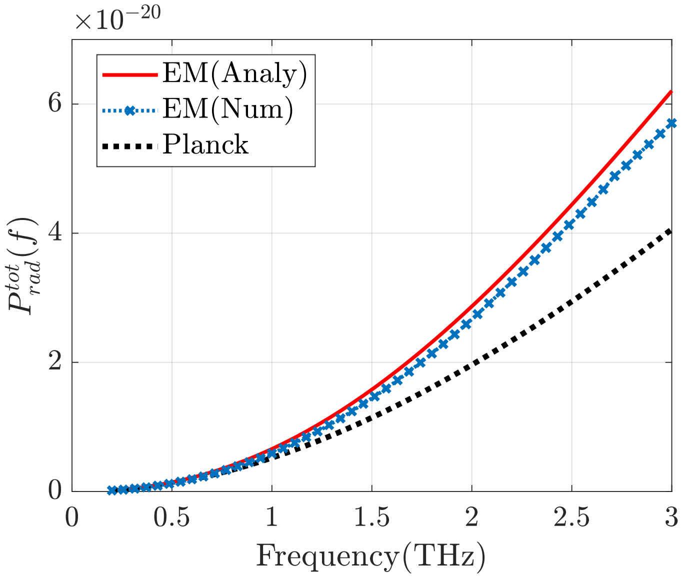

Figure 6.15: Numerical validation of BM4.

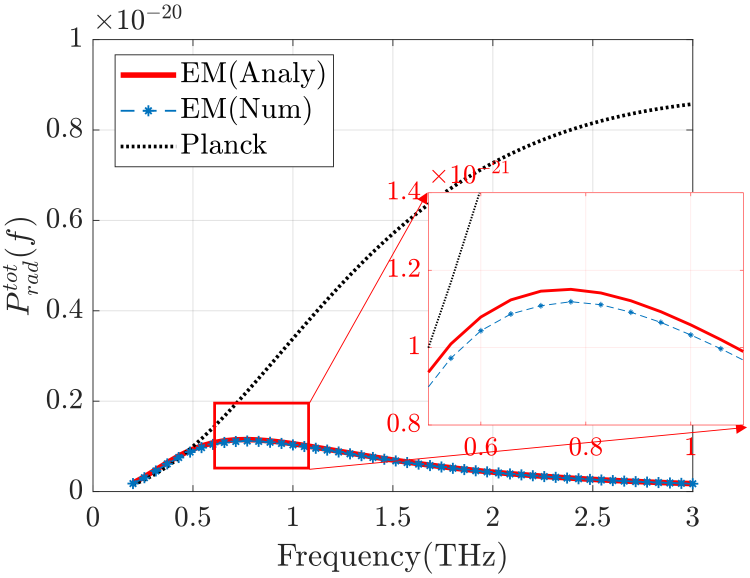

Figure 6.16: Numerical validation of Si2.

6.6.2. Analysis on the Discrepancies

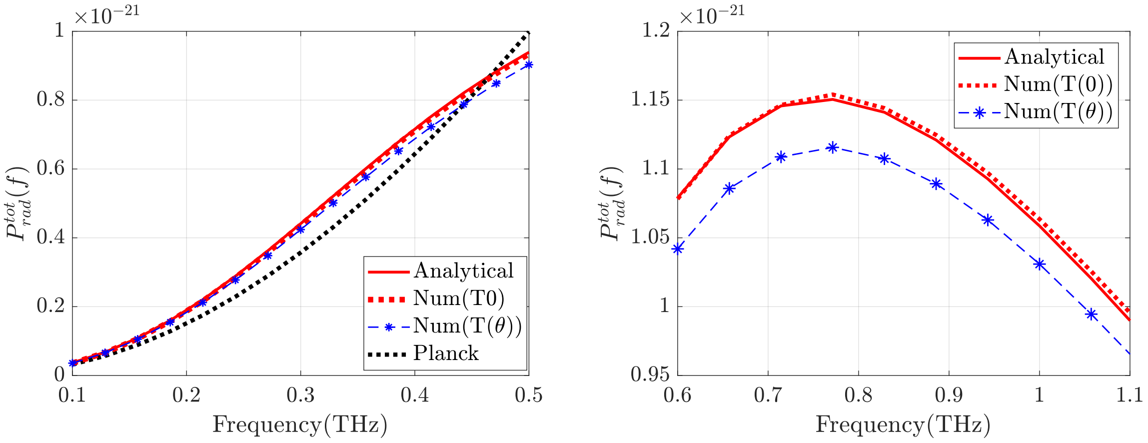

(a) 0.1 to 0.5 THz (b) 0.6 to 1.1 THz

Figure 6.17: Comparioson when T_{eff} is taken as T(0) and T(θ)

The discrepancies between the analytical expression and the numerical evaluation primarily come from the approximation we take in (6.29), where we assumed in the analytical expression that the transmission coefficient is always equal to the broadside case for the angle of incidence smaller than the critical angle θ_c. In fact, the effective transmission coefficient T_{eff} in (6.53) varies with respect to the angle of incidence, as shown by the example in Figure 6.13.

We can examine this judgment by setting T_{eff} in the numerical validation also always equal to the broadside case, as in the analytical approximation. Figure 6.17 shows the case of Si2 from 0.1 to 0.5 THz and around the peak of the curve from 0.6 to 1.1 THz. As we can see from the figure, the numerical results of T_{eff} always taken as broadside (indicated as **Num**(T(0)) in the figure), almost overlaps with the analytical curve. While for the numerical results of T_{eff} calculated by the Fresnel equations (indicated as **Num**(T(θ)) in the figure), the discrepancy remains.

Also, some numerical errors can also be induced by the lack of accuracy during the numerical calculation process at high frequencies.

Now we are able to conclude that analytical expression (6.35) is a good approximation for most of the cases and can be used to estimate the total spetral power radiated outside a bulk object made from ohmic materials.

7

Experiment Proposal

In previous chapters, we have established a classic EM model to estimate the power radiated from a finite real body. This model sets the theoretical basis for our measurement campaign, which will be introduced in this chapter.

Due to the lack of existing data for the thermal radiation of a real finite body made by ohmic materials at known temperatures, we would like to propose a campaign to provide accurate measurements of radiated power from material bodies in the mm and sub-mm range and test the validity of our classic EM model versus the Planck-like model.

Section 7.1 to 7.5 introduces the preliminary works of designing the experiment, including the process of material selection, material characterization using Terahertz Time Domain Spectroscopy (THz-TDS) system, instrument selection and the readout mechanism. Silicon is selected as the material for the measurement. Four Virginia Diodes (VDI) [48] zero-bias Schottky detectors operating at different frequency bands are selected as the measurement instrument. A cavity on a waveguide (WG) short is designed to host the sample. The readout mechanism is discussed in Section 7.5. A low-noise amplifier should be connected to enhance the DC voltage level in the output of the detector.

Then, three measurement set-ups are proposed in Section 7.6.

7.1. Material Selection

Silicon is one of the most widely used materials in modern integrated circuits. This prevalence provides us with easy access to silicon samples with different doping levels. Also, silicon can be in various sizes, from the finest wafer to large ingots. The technologies to process silicon materials, like laser dicing or photolithography and etching, are fairly mature.

As studied in Section 3.1.2, silicon can easily reach resistivity between $0.1 \sim 100\Omega cm$ by doping, resulting in its transition frequency appearing in the frequency range of the sub-THz band. The frequency-dependent characteristics of silicon can be accurately modelled by Drude model. Carefully manipulating the doping levels between samples, we can achieve desired characteristics of silicon to have a clear contrast in measured power to test our model. Based on all the aforementioned reasons, we would like to choose silicon as our measurement material.

We can calculate the power per frequency radiated by silicon with different doping using our EM model. The analytical expression of the radiated power per frequency is given by (6.35):

$$P_{EM}(f) = \frac{4}{\lambda_\beta^3}\frac{\pi}{\lambda_0^2}\frac{|I_0|^2\zeta_0\Delta^2}{k_\alpha Re\left\{\sqrt{\varepsilon_{r,eff}}\right\}}\left[1-|\Gamma|^2\right]\left[1-e^{-2k_\alpha L}\right]\cdot SA. \tag{7.1}$$

The power per frequency of the Planck-like curve predicted by Bekefi [20] in (2.6) is also given for comparison as:

$$P_{Plk}(f) = \frac{hf^3}{c_0^2}\frac{1}{e^{\frac{hf}{k_BT}}-1}\left[1-|\Gamma|^2\right]\left[1-e^{-2k_\alpha L}\right]\cdot SA. \tag{7.2}$$

Consider a cubic silicon sample with a side length of $L = 500\mu m$. The surface area of the sample can be calculated as: $SA = 6\times L^2 = 1.5\times 10^{-6} mm^2$. Using the analytical expression given by our EM model (7.1), we can plot the spectral power radiated by the samples with various doping levels. Figure 7.1a shows results from 75 GHz to 500 GHz of four different types of silicon, whose electron density n are 10^{21}, 10^{22}, 10^{23}, and 10^{24} electrons/m^2 and corresponding nominal resistivity are about 4.6, 0.5, 0.09 and 0.02 Ωcm respectively, at room temperature of 300 K. For comparison, the result of a metal sample (Copper(Cu) with $n = 8.49\times 10^{28}$ electrons/m^2 and $\tau = 27fs$.) of the same size is also provided in Figure 7.1a. The results of the same samples predicted by (7.2) are given in Figure 7.1b. Silicon samples with an electron density of 10^{22} electrons/m^2 can radiate the most spectral power in both predictions. Figure 7.2 shows the direct comparison between our EM model and the Planck-like curve in linear scale. As we can see from Figure 7.2b, for silicon with an electron density of $n = 10^{22}$ electrons/m^2, the results predicted by two models are comparable. While for $n = 10^{21}$ electrons/m^2 case as shown in Figure 7.2a, the results of our EM model is one magnitude lower than the prediction of the Planck-like curve.

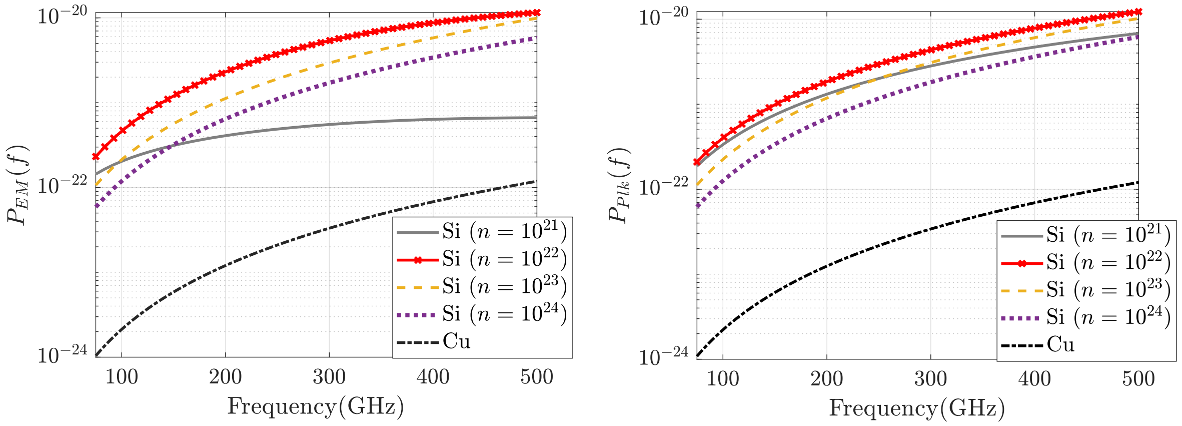

(a) EM model (7.1)

(b) Planck-like curve (7.2)

Figure 7.1: Spectral power radiated by the silicon sample predicted by two models.

The spectral power results for silicon sample with $n = 10^{22}$ electrons/m^2 at various temperatures (300 (room temperature), 500, 800 and 1000 Kelvin) are shown in Figure 7.3. The radiated spectral power is higher for higher temperatures.

7.2. Material Characterization

Commercially available silicon wafers are labelled by the nominal resistivity, i.e. the traditional quasi-static model as introduced in Section 3.1. However, due to limitations caused

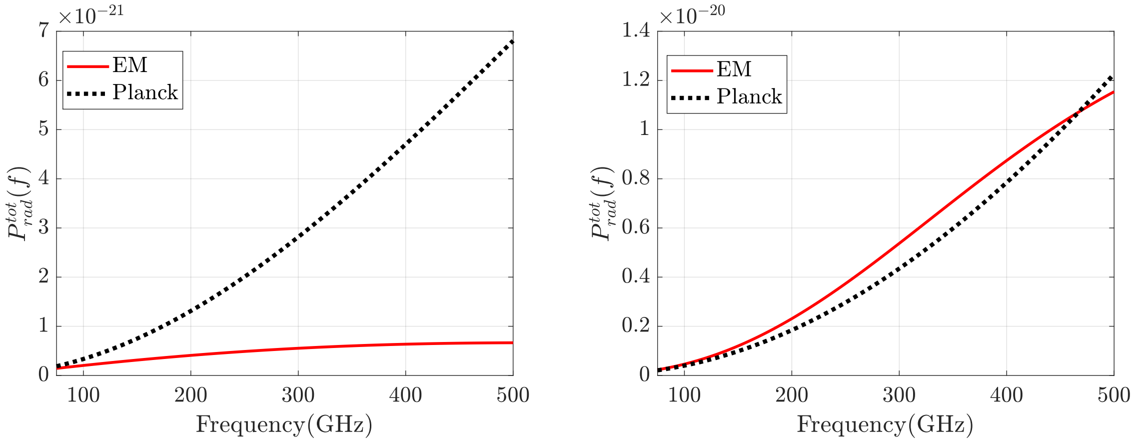

(a) $n = 10^{21}$ electrons/m^2.

(b) $n = 10^{22}$ electrons/m^2.

Figure 7.2: Comparison between the EM model and the Planck-like curve for two samples in linear scale.

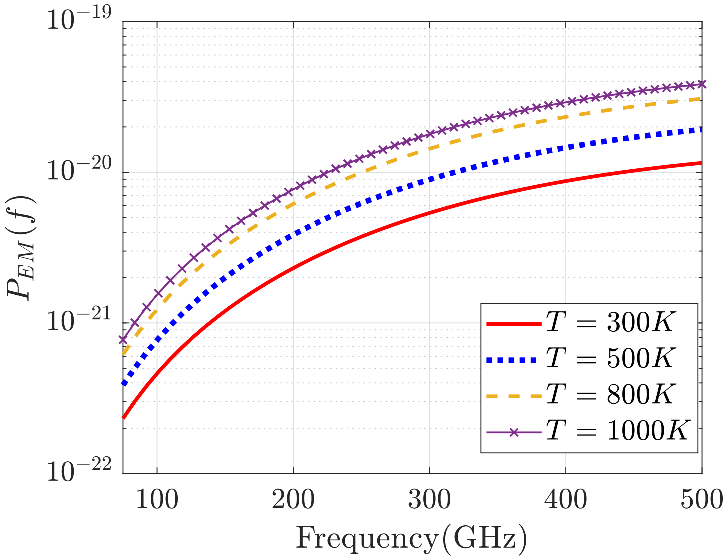

Figure 7.3: Spectral power for silicon sample with $n = 10^{22}$ electrons/m^2 at various temperatures.

by the manufacturing process, it is difficult to have accurate control of these parameters. As a result, this nominal resistivity is usually given in a rough range. To get the exact parameter of the sample under test (SUT), we propose to use the THz-TDS system provided by Menlo systems [49]. A brief introduction of the system and the measurement set-up is given in Appendix E, as well as the procedure to extract the complex permittivity of the SUT from the measured transmission coefficient data. Then a transmission line model (Figure 7.4) is established and analysed in detail in Appendix F to reconstruct this transmission coefficient from a theoretical perspective. By comparing the theoretical and measured transmission coefficients, we can fit our measured data into Drude model to have a complete understanding of the SUT.

During the characterization, one measurement with SUT and one reference measurement without SUT are done. The received time domain signal can be transformed into the frequency domain signal using Fourier Transform. The measured transmission coefficient

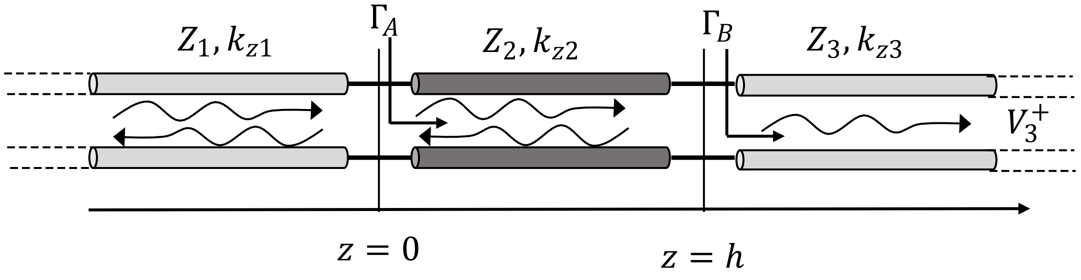

Figure 7.4: Transmission line model for the THz-TDS sample measurement.

data can then be expressed as:

$$T = \frac{\tilde{S}_s\left(f\right)}{\tilde{S}_r\left(f\right)}, \tag{7.3}$$

where $\tilde{S}_r\left(f\right)$ is the frequency domain reference data and $\tilde{S}_s\left(f\right)$ for frequency domain measurement data with SUT. The theoretical transmission coefficient can be derived from the transmission line model shown in Figure 7.4. Medium 2 represents the SUT, and medium 1 and 3 are regarded as free space. The THz pulse is transmitted from the side of medium 1 and received at the side of medium 3. The transmission coefficient from medium 1 to medium 3 can be represented as:

$$T = \frac{\left(1+\Gamma_B\right)\left(1+\Gamma_A\right)}{e^{jk_{z2}d}e^{-jk_0 d}\left(1+\Gamma_B e^{-jk_{z2}2d}\right)}, \tag{7.4}$$

where Γ_A and Γ_B are the reflection coefficients at point A and B, k_0 and k_{z2} are propagation constants in free space and SUT, and d is the thickness of SUT.

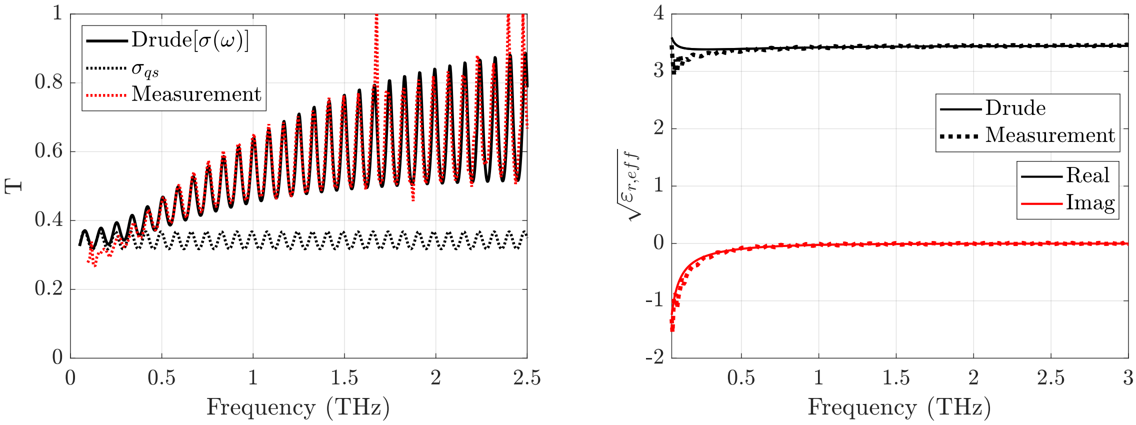

(a) The Transmission coefficient.

(b) The square root of effective permittivity.

Figure 7.5: Fitting the data of a silicon slab measured using THz-TDS with Drude model.

Figure 7.5 shows an example of a silicon slab with a thickness of $d = 525\mu m$ and labelled with nominal resistivity as $2 \sim 5\Omega cm$. After tuning the parameters and fitting with Drude model, the electron density of the silicon slab is found as 1.15×10^{21}electrons/m^2. The corresponding nominal (quasi-static) resistivity of this silicon slab is $4\Omega cm$. The transmission coefficients from the measurement (as defined in (7.3)) and Drude model (as defined in

(7.4)) are shown in Figure 7.5a. For comparison, the transmission coefficients of (7.4) evaluated by the traditional quasi-static model of conductivity is also given in Figure 7.5a. It can be clearly seen from the figure that the quasi-static model can not represent the behaviour of the material for high frequencies, which are frequencies higher than a few hundred GHz in the case of silicon. The square root of effective permittivity $\sqrt{\varepsilon_{r,eff}}$ of the fitted Drude model is shown in Figure 7.5b, compared with the effective permittivity directly extracted from the measurement data (detailed methods can be found in Appendix E). The oscillations of measurement data from both figures in Figure 7.5 and the transmission coefficient fitted by Drude model in Figure 7.5a represent the multi-reflect of the THz signal at the air-dielectric interface between SUT and its surrounding environment.

7.3. Detectors

Based on the predictions given in Section 7.1, we can calculate the sensitivity requirements of the detectors needed in this campaign. Consider a bandwidth of $BW = 100$ GHz and an average spectral power of $P(f) = 10^{-21}$ W/Hz for silicon with an electron density of $n = 10^{22}$ electrons/m^2, the estimated power over this frequency band $P_{BW} = P\left(f\right)BW = 10^{-10}$ W, which is too small to be detected by the normal broadband power detectors. To avoid complexity and make the measurements repeatable, cryogenic detectors are avoided during the selection process.

Schottky diodes have long been used as direct detectors for microwave bands [50]. It can operate in either room or cryogenic temperature and generally has a faster response time compared with traditional detectors like bolometers [51]. Schottky diodes have great sensitivity and frequency response with zero bias. For our measurement campaign, we select four different zero-bias Schottky diode detectors from VDI [48] operating in different frequency bands. These detectors are typically hosted in waveguide cavities and there is a detector for each of the standard rectangular waveguide. Each of the detectors is supposed to be sensitive only to signals in the spectral bandwidth and its corresponding waveguide is considered as single mode. Their parameters are shown in Table 7.1.

Table 7.1: Parameters of VDI zero-bias detectors.

Model	Frequency Band (GHz)	WG Dimension $(mm \times mm)$	NEP $(pW/\sqrt{Hz})$	Responsivity (V/W)
WR10ZBD	75 – 110	2.5 × 1.27	9.4	2800
WR5.1ZBD	140 – 220	1.2954 × 0.6477	11	2400
WR3.4ZBD	220 – 330	0.8636 × 0.4318	12	2200
WR2.2ZBD	330 - 500	0.5588 × 0.2794	12.7	1600

All these detectors have a rectangular waveguide RF input port and coaxial output, as shown in Figure 7.6. The parameter *responsivity* in Table 7.1 represents the ratio between the input RF power P_{rec} and output voltage V_{out} of the detector system. It is defined as:

$$R_{esp} = \frac{V_{out}}{P_{rec}}. \tag{7.5}$$

The responsivity is in the unit of V/W. The responsivity data given in Table 7.1 is the typical responsivity and is subject to change for different detectors. Each detector should be cal-

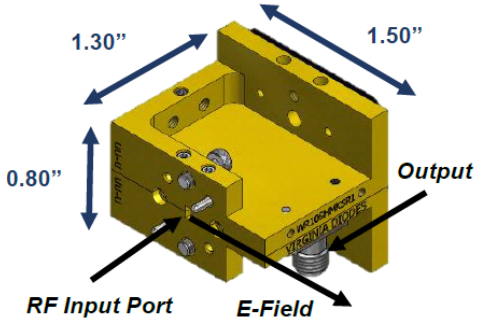

Figure 7.6: Schematic of WR10ZBD from [52]. (The dimensions are in inches).

ibrated in order to get the detailed responsivity curve with respect to frequency. Another parameter is *NEP*, which stands for Noise Equivalent Power. It represents the spectral density of noise divided by the responsivity and is in the unit of $W/\sqrt{Hz}$. It can be represented by Signal-to-Noise Ratio after detection (SNR_{AD}) as shown in Figure 7.7 by:

$$SNR_{AD} = \frac{P_{rec}}{NEP}\sqrt{2\tau_{int}}, \tag{7.6}$$

where P_{rec} represents the power received and τ_{int} stands for the integration time. NEP is defined as the power that makes SNR_{AD} equal to 1 in 1 Hz of output bandwidth. If τ_{int} is taken as 0.5 seconds, P_{rec} will be equal to NEP in this case. Generally, NEP is used as a metric to describe the sensitivity of the detector. As we can see from Table 7.1, VDI zero-bias detectors generally have NEP of several picowatts per square root of Hertz, which satisfy the requirements of our measurements.

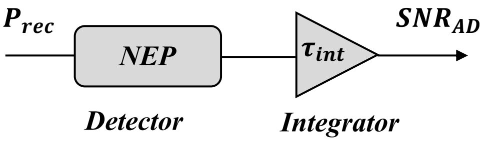

Figure 7.7: Definition of NEP.

7.4. Waveguide Short Cavity to Host Samples

Because operating at high frequencies, the waveguide input ports of the VDI zero-bias detectors are physically very small, as seen in Table 7.1. It is difficult to put measurement samples directly inside the waveguide. A cavity is designed on a waveguide short to host the silicon sample as shown in Figure 7.8. The waveguide short is commercially available from [53]. The silicon sample can be diced from a large silicon wafer. Then the waveguide short can be screwed to the RF input port of the detector, acting as the source of the measurement. The detailed drawing of the design of this cavity is shown in Appendix G. Figure 7.9 shows the cross-section of the structure when the waveguide short is connected to the RF input port. The silicon sample is placed at the centre of the cavity. Due to the fact that the aperture of the waveguide port A_p is much smaller than the size of the sample, only a part of the power fluxes will go into the waveguide. This structure is then equivalent to putting a silicon sample directly in the waveguide.

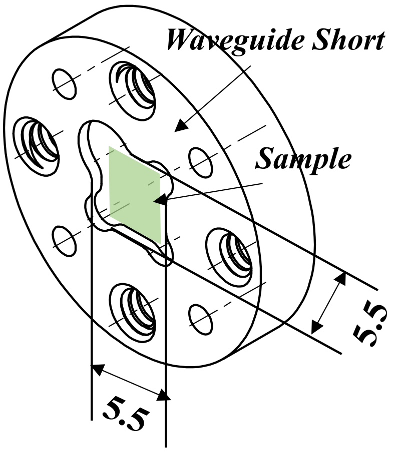

Figure 7.8: Cavity on the waveguide short for silicon sample. Dimensions are in mm.

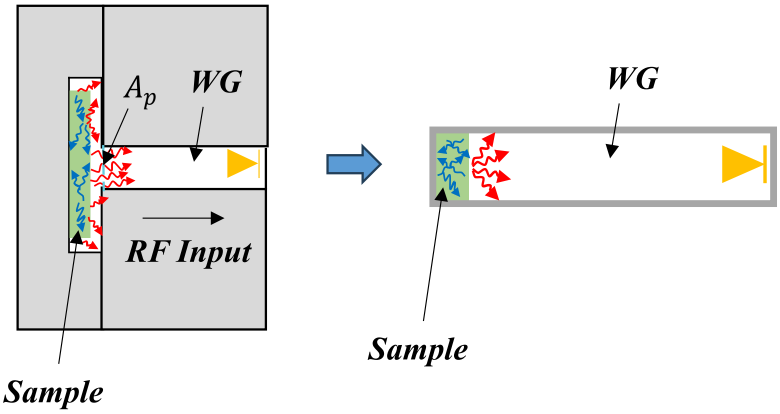

Figure 7.9: Cross-section of the waveguide short with sample placed in the cavity connected to the RF input port of the detector. Equivalent to sample directly put in waveguide.

7.5. Readout Mechanism

A digital multimeter HP 3458A [54] is used to read the voltage output of the detector. The smallest input resistance of this multimeter can be selected as $R_{in} = 10M\Omega$. In this case, the Johnson Noise of this input resistance can be calculated as:

$$v_n = \sqrt{4k_B T R_{in}} = 4 \times 10^{-7} V = 400nV. \tag{7.7}$$

However, the thermal RF signals are all expected to be around or lower than 10^{-9} W. Consider the example given in Section 7.1. As we can see from Figure 7.2b, the average spectral power for the sample with $n = 10^{22}$ electrons$/m^2$ over WR10 bandwidth $(BW = 35$ GHz$)$ is $P_{avg}(f) = 0.5 \times 10^{-21}$ W/Hz. The power detected over this bandwidth can be estimated as $P_{det} = P_{avg}(f)\, BW = 17.5$ pW. The typical responsivity of the corresponding detector is 2800 V/W (Table 7.1). Then we can calculate the expected output voltage of the detector using (7.5) as:

$$v_{out}^{ex} = R_{esp} P_{rec}^{ex} = 17.5 \times 10^{-12} \times 2800 = 4.9 \times 10^{-8} = 49nV. \tag{7.8}$$

which is lower than the Johnson noise of the input resistance. Accordingly, the multimeter cannot be used because the signal will entirely be submerged by the Johnson noise.

A low-noise operational amplifier can then be used to enhance the DC voltage level in the output of the detector, and the multimeter is then cascaded to the amplifier to perform the reading. If the voltage gain of the amplifier is set as $G = 1000$, the expected voltage after the amplifier v_{amp}^{ex} can be calculated as:

$$v_{amp}^{ex} = Gv_{out} = GR_{esp}P_{rec}^{ex} = 4.9 \times 10^{-5} V = 49 \mu V, \tag{7.9}$$

which should give at least two orders of magnitude of dynamic range for the voltage. The interpretation of the received power P_{rec} from the voltage readout can be simply obtained inverting (7.9) as:

$$P_{rec} = \frac{v_{amp}}{G\,R_{esp}}. \tag{7.10}$$

7.6. Measurement Set-ups

Three possible measurement set-ups are proposed in this section.

- A. Measurement of a large ingot in the far field.

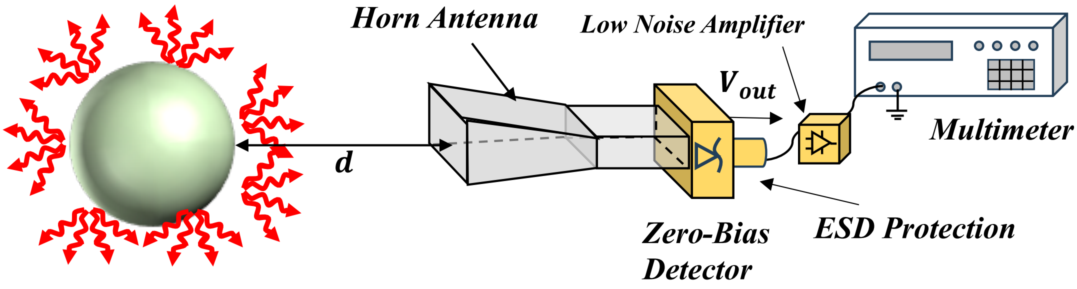

Figure 7.10: Measurement of a large ingot in the far field.

A set-up can be proposed as the measurement of a large ingot in the far field through a horn antenna. The detector is directly connected to the receiving antenna. Then, an ESD (Electrostatic Discharge) protection circuit is connected to the output port of the detector to protect its ESD-sensitive components. Then, because the output signal is small, a low noise amplifier is connected to amplify the output DC signal. Then the signal can be read by the multimeter.

Using our EM model given in (7.1) or the Planck-like curve given in (7.2), we can calculate the brightness of the radiating object by assuming it is uniform in free space as:

$$B_{fs}(f) = \frac{P_{rad}^{tot}(f)}{4\pi\, SA}, \tag{7.11}$$

where SA is the surface area of the radiating object. $P_{rad}^{tot}(f)$ is the spectral power radiated by the object.

Then the estimated received power by a horn antenna operating in a certain bandwidth BW can be calculated as:

$$P_{rec} = \int_{BW} \int_{\Omega_a} A_{eff}(\Omega, f)\, F(\Omega, f)\, B_{fs}(\Omega, f)\, d\Omega_a df\,, \tag{7.12}$$

where $A_{eff}\left(\Omega,f\right)$ is to the effective aperture of the receiving antenna, $F\left(\Omega,f\right)$ is the normalized radiation pattern of the antenna, and Ω_a is the beam solid angle of the receiving antenna. We can assume that the brightness is constant in the solid angle of the antenna. Then, (7.12) can be expressed as:

$$P_{rec} = \int_{BW} A_{eff}(f) B_{fs}\left(f\right) \int_{\Omega_a} F\left(\Omega\right) d\Omega_a \, df. \tag{7.13}$$

The efficiency of the antenna $\eta_{ant}\left(f\right)$ is defined as:

$$\eta_{ant}\left(f\right) = \frac{G_{ant}\left(f\right)}{D_{ant}\left(f\right)}. \tag{7.14}$$

where G_{ant} is the gain of the antenna and D_{ant} is the directivity of the antenna. Here, we can take the directivity as its maximum, $D_{ant}\left(f\right) = D_{max}$. It can then be represented by the normalized radiation pattern:

$$D_{max}\left(f\right) = \frac{4\pi}{\int_{\Omega_a} F\left(\Omega\right) d\Omega_a}. \tag{7.15}$$

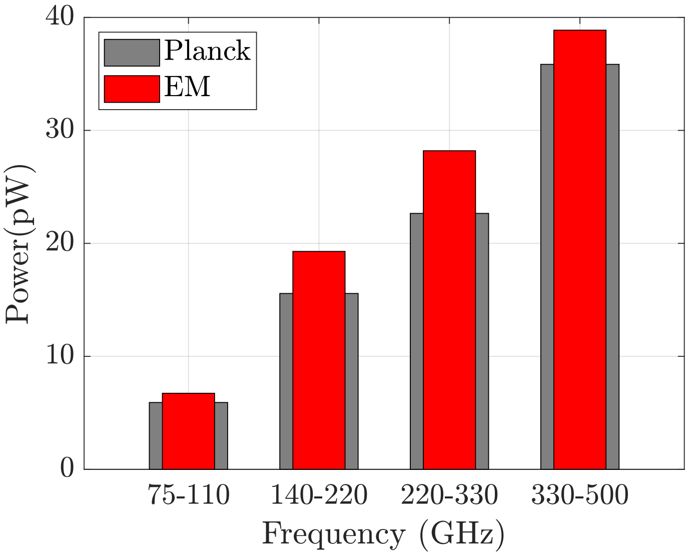

Figure 7.11: Estimated power detected for Set-up A for silicon ingots with an electron density of $n = 10^{22}$ electrons/m^2.

Table 7.2: Estimated power (pW) detected for Set-up A for silicon ingots with an electron density of $n = 10^{22}$ electrons/m^2.

	WR10 (75~110 GHz)	WR5.1 (140~220 GHz)	WR3.1 (220~330 GHz)	WR2.2 (330~500 GHz)
EM	6.7	19.3	28.2	38.9
Planck	6.0	15.6	22.6	35.8

The effective aperture A_{eff} can be represented as:

$$A_{eff}(f) = G_{ant}(f)\frac{\lambda_0^2}{4\pi}. \tag{7.16}$$

Substituting (7.14) ∼ (7.16), (7.13) can be represented as:

$$\begin{aligned}
P_{rec} &= \int_{BW} B_{fs}(f)\, G_{ant}(f)\frac{\lambda_0^2}{4\pi}\int_{\Omega_a} F(\Omega)\, d\Omega_a\, df \\
&= \int_{BW} B_{fs}(f)\, \eta_{ant}(f)\, D_{ant}(f)\frac{\lambda_0^2}{4\pi}\int_{\Omega_a} F(\Omega)\, d\Omega_a\, df \\
&= \int_{BW} B_{fs}(f)\, \eta_{ant}(f)\frac{4\pi}{\int_{\Omega_a} F(\Omega)\, d\Omega_a}\frac{\lambda_0^2}{4\pi}\int_{\Omega_a} F(\Omega)\, d\Omega_a\, df \\
&= \int_{BW} B_{fs}(f)\, \eta_{ant}(f)\lambda_0^2 df.
\end{aligned} \tag{7.17}$$

(7.17) tells us that for a thermal source distributed over a solid angle wider than the antenna beam, the received power by the antenna is proportional to antenna efficiency.

Consider a set of ideal horn antennas operating at the same frequency bands as the detectors. Their all have a constant efficiency over their bandwidth as $\eta_{ant} = 0.9$. Then we can estimate the received power over the frequency bands of the detectors given in Table 7.1 using (7.17) for silicon ingots with an electron density of $n = 10^{22}$ electrons$/m^2$. Comparisons are made for results using our EM model (7.1) and the Planck-like curve (7.2). The detailed numbers can be found in Table 7.2. The numbers are comparable to those that we expected to be able to measure based on the sensitivity of the detectors given in Table 7.1. It is not known how sensitive these detectors are outside their designated frequency band.

- B. Direct measurement through the waveguide.

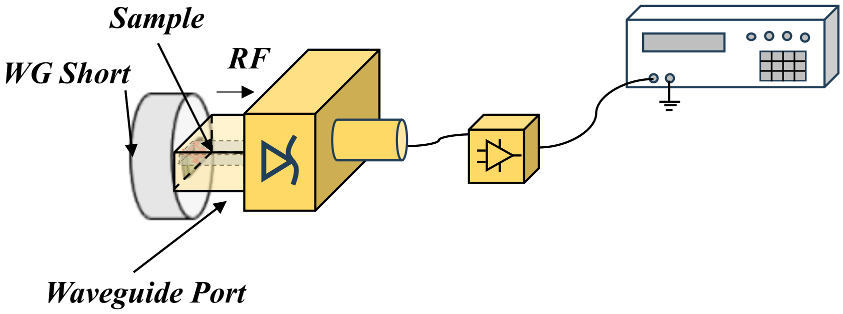

Figure 7.12: Direct measurement through waveguide.

The second set-up can then be proposed to provide a direct measurement through the waveguide. Silicon samples are placed in the cavity in the waveguide short introduced in Section 7.4. Then the waveguide short is directly connected to the RF input waveguide port of the detector. The readout mechanism is similar to the first set-up with a low-noise amplifier connected between the output port of the detector and the multimeter. We expect the power level of this set-up is comparable to the previous case.

- C. Measurement through two antennas in the near field.

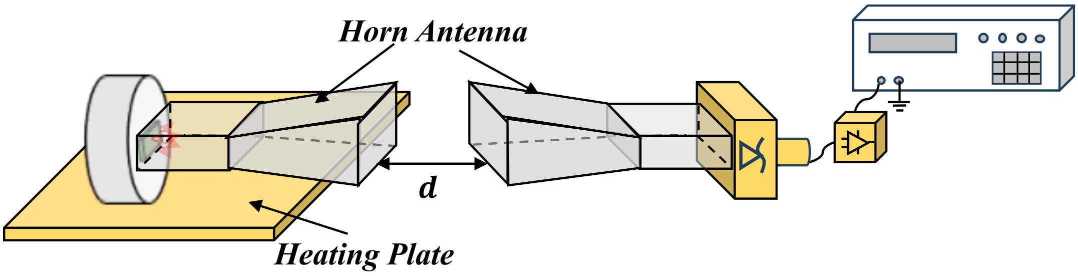

Figure 7.13: Measurement through two antennas in the near field.

The third set-up is measurement through two horn antennas placed at the near field. The waveguide short with the sample placed in the cavity is connected to the transmitting antenna. The detector is connected to the receiving antenna. The two antennas are aligned and the distance d between the two antennas is smaller than $2D^2/\lambda$ (D is the dimension of the horn antenna and λ is the wavelength) to ensure the near field transmission. The power per frequency received can be estimated by:

$$P_{rec}(T) = \int_{BW} P_{WG}\left(f,T\right)\ S_{21}(f,d)df, \tag{7.18}$$

where $P_{WG}\left(f,T\right)$ is the total spectral power radiated by the sample in the waveguide and can be estimated by our model and $S_{21}(f,d)$ is the power transmission coefficient from the input port of the transmitting antenna to the output port of the receiving antenna and can be obtained using full wave simulation tools like CST studio. A heating plate can be placed under the transmitting structure to achieve measurements at different temperatures T.

A possible matching layer design can be applied on the surface of the silicon samples to increase the radiated power. The detail of this design is discussed in Appendix H.

8

Conclusions and Future Work

A rigorous model based on classic EM to characterize the thermal radiation of real ohmic media is described in this thesis. Based on Johnson's theory of thermal noise in electric circuits, the model explains the available energy due to thermal agitation inside ohmic material. The field is expanded in a finite number of modes (degrees of freedom per unit of volume), which are all independent and orthogonal from each other and are eigenvectors of Maxwell's Equations.

The self-impedance of one eigenvector is given analytically in (5.10), based on which the energy available per degree of freedom could be calculated by a Johnson-like circuit. The mutual impedance of two eigenvectors is asymptotically approximated by (5.55). It turns out that the minimum distance for two eigenvectors to be independent is $\lambda_\beta/2$, where λ_β is the real effective wavelength in the medium. Then, the number of degrees of freedom in a finite volume is given by (5.53) and the total energy available by thermal agitation in the finite volume is given by (5.57).

Considering a real material body, the generating current of each of the modes is defined as volumetric, resulting in a discretization of the radiating object. Then, the directional generating currents are replaced by isotropic sources to simplify the calculation process. The Poynting vectors of sources over the entire object volume are integrated, resulting in an analytical expression (6.35) to estimate the total spectral power radiated out by a real ohmic material body as:

$$P_{EM}(f) = \frac{4}{\lambda_\beta^3} \frac{\pi}{\lambda_0^2} \frac{|I_0|^2 \zeta_0 \Delta^2}{k_\alpha Re\left\{\sqrt{\varepsilon_{r,eff}}\right\}} \left[1 - |\Gamma|^2\right] \left[1 - e^{-2k_\alpha L}\right] \cdot SA, \tag{8.1}$$

where $|I_0|$ is defined in (6.4), k_α is the imaginary part of the propagation constant, $\varepsilon_{r,eff}$ is the effective permittivity of the medium, $|\Gamma|^2$ is the power reflection coefficient at the medium-air surface, L is the path Poynting vectors have traversed and SA is the surface area of the radiating object.

This model is purely based on classic EM. The frequency dependence of the spectral thermal radiation power it predicted directly comes from the resistivity dispersion of the material that makes up the radiating body. As a result, Planck's law of black body radiation is no longer required as an intermediary.

A measurement campaign is proposed aiming at providing accurate measurements of the thermal radiation from silicon samples of small dimensions in the mm and sub-mm wave regime. The samples are characterised by a THz-TDS system to obtain their exact EM parameters. Four Schottky diode zero-bias detectors are selected and different possible measurement set-ups are described.

Future works of this project should focus on the measurement campaign. The radiation mechanism of silicon samples hosted in the cavity should be studied in order to estimate the power detected in Set-up B and C. The horn antenna in Set-up A and C should be selected and measured. The noise level of the measurement system should be characterized. After the successful measurement of silicon samples, the potential of measuring different kinds of materials should be studied.

A

Power Radiated by Material Objects Based on the Hybrid Model

Consider a large object made of lossy medium in which the internal reflections can be neglected. Using the reciprocity suggested by generalized Kirchhoff's law, the total power radiated per unit solid angle is given by Bekefi in Eq.(33) of [20] as:

$$P\left(f,\Omega\right)=\left[1-|\Gamma|^2\right]B_{Bkf}\left(f,T\right)S\left[1-\exp\left(-\alpha_\omega L\right)\right], \tag{A.1}$$

where α_ω represents the total absorption per unit length of path. It can be calculated as:

$$\alpha_\omega=\frac{4\pi}{\lambda}Imag\left\{\sqrt{1+\frac{\sigma}{j\omega\varepsilon_0\varepsilon_{r\infty}}}\right\}. \tag{A.2}$$

Using the definition of effective permittivity in (3.8), α_ω can be expressed by k_α, the imaginary part of propagation constant:

$$\alpha_\omega=\frac{4\pi}{\lambda_0}\sqrt{\varepsilon_{r\infty}}Imag\left\{\sqrt{1+\frac{\sigma}{j\omega\varepsilon_0\varepsilon_{r\infty}}}\right\}=2Imag\left\{\frac{2\pi}{\lambda_0}\sqrt{\varepsilon_{r,eff}}\right\}=2k_\alpha. \tag{A.3}$$

Notice that the absorption coefficient given in (A.2) is derived from the characteristics of the material being considered, rather than the absorption process suggested by the reciprocity of generalized Kirchhoff's law. In this way, (A.1) can be written as:

$$P\left(f,\Omega\right)=\left[1-|\Gamma|^2\right]B_{Bkf}\left(f,T\right)S\left[1-e^{-2k_\alpha L}\right]. \tag{A.4}$$

In (A.1) and (A.4); L represents the total path the Poynting vector traversed in the object; $|\Gamma|^2$ refers to power reflection coefficient; And S refers to the projection of the cross-section of the object onto a plane that is perpendicular to the observer, as shown in Figure A.1. The reason to choose the cross-section is that for an object of arbitrary shape, the projection of its cross-section is easy to identify. $B_{Bkf}\left(f,T\right)$ is given by Bekefi (Eq.(5) of [20]) for one polarization, using Rayleigh-Jeans law (2.3), as:

$$B_{Bkf}^{RJ}\left(f,T\right)=\frac{k_BTf^2}{2\pi c_0^2}. \tag{A.5}$$

Accordingly, using Planck's law of black body radiation (2.2), $B_{Bkf}(f,T)$ can be given as:

$$B_{Bkf}^{Plk}(f,T) = \frac{hf^3}{2\pi c_0^2}\frac{1}{e^{\frac{hf}{k_B T}}-1}. \tag{A.6}$$

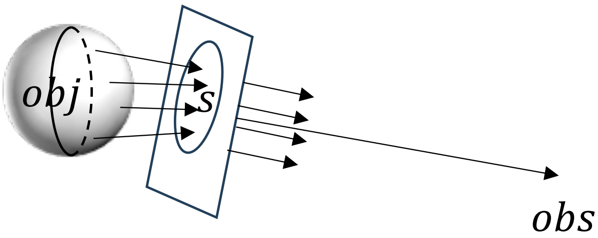

Figure A.1: Cross-section of the radiating object.

However, we can consider the object as a Lambertian surface. According to Lambert's cosine law [55], this kind of surface has the following identities, as shown in Figure A.2. For a unit of radiation surface dA, each wedge in Figure A.2 represents a unit of solid angle $d\Omega$. The intensity of radiation of each wedge corresponds to the area of the wedge. Using simple geometry, we know that the length of each wedge is the diameter of the circle times $\cos\theta$. Here, θ denotes the angle between the direction of radiation intensity (same as the direction of Poynting vector) and the normal of the radiation surface dA. So, when the observer is at broadside, it can receive the maximum radiation intensity $I_{max}d\Omega dA$. For the observer at θ, the intensity is reduced to $I_{max}\cos(\theta)d\Omega dA$.

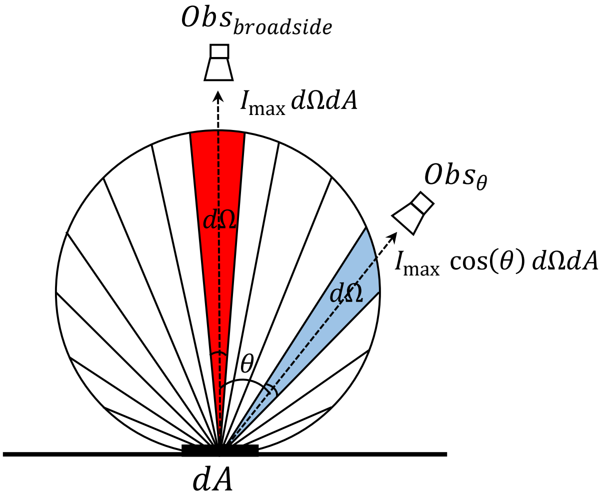

Figure A.2: Lambert's cosine law.

Using the Lambertian cosine law, power radiated per unit solid angle $d\Omega$ from per unit of surface dA can be represented as:

$$P(f,\Omega,A) = \left[1-|\Gamma|^2\right] B_{Bkf}(f,T)\left[1-e^{-2k_\alpha L}\right]\cos\theta. \tag{A.7}$$

Integrating (A.7) over all solid angle 4π and entire surface area SA, the total spectral power radiated by the bulk object per frequency can be written as:

$$P(f) = \iint_{SA}\int_0^{2\pi}\int_0^{\frac{\pi}{2}} \left[1-|\Gamma|^2\right] B_{Bkf}(f,T)\left[1-e^{-2k_\alpha L}\right]\cos\theta\sin\theta d\theta d\phi dA. \tag{A.8}$$

The integral regarding θ and ϕ can be closed as:

$$\int_0^{2\pi} d\phi = 2\pi, \tag{A.9a}$$

$$\int_0^{\pi/2} \cos\theta \sin\theta d\theta = \frac{1}{2} \sin^2\theta|_0^{\frac{\pi}{2}} = \frac{1}{2}. \tag{A.9b}$$

Then (A.8) can be written as:

$$P\left(f\right) = \left[1 - |\Gamma|^2\right] B_{Bkf}\left(f, T\right) \left[1 - e^{-2k_\alpha L}\right] \pi \cdot SA. \tag{A.10}$$

Here, SA represents the whole surface area of the Lambertian source. Considering two possible polarizations, the total spectral power radiated for low frequencies can be represented by replacing $B_{Bkf}\left(f, T\right)$ with (A.5):

$$P_{RJ}\left(f\right) = \frac{k_B T f^2}{c_0^2} \left[1 - |\Gamma|^2\right] \left[1 - e^{-2k_\alpha L}\right] \cdot SA. \tag{A.11}$$

Replacing $B_{Bkf}\left(f, T\right)$ with (A.6), (A.11) can be represented as:

$$P_{Plk}\left(f\right) = \frac{hf^3}{c_0^2} \frac{1}{e^{\frac{hf}{k_B T}} - 1} \left[1 - |\Gamma|^2\right] \left[1 - e^{-2k_\alpha L}\right] \cdot SA. \tag{A.12}$$

Then the total power radiated by the bulk object over certain bandwidth BW can be represented as:

$$P = \int_{BW} P\left(f\right) df = \left[1 - |\Gamma|^2\right] \left[1 - e^{-2k_\alpha L}\right] 2\pi \cdot SA \int_{BW} B_{Bkf}\left(f, T\right) df. \tag{A.13}$$

B

Derivation of Eigenvalues of Maxwell's Equations

The Maxwell's equations only with electric source $\vec{J}$, satisfying radiation condition, can be written as follows:

$$\nabla \times \vec{E} = -j\omega\mu\vec{H}, \tag{B.1a}$$

$$\nabla \times \vec{H} = j\omega\varepsilon\vec{E} + \vec{J}, \tag{B.1b}$$

$$\nabla \cdot \vec{H} = 0, \tag{B.1c}$$

$$\nabla \cdot \left(\vec{E} + \frac{\vec{J}}{j\omega\epsilon} \right) = 0. \tag{B.1d}$$

Take the curl of both sides of (B.1b). By substituting (B.1a) in, the wave equation can be arrived for magnetic field $\vec{H}$ as:

$$\nabla \times \nabla \times \vec{H} - k^2\vec{H} = \nabla \times \vec{J}, \tag{B.2a}$$

where $k^2 = \omega^2\mu\varepsilon$. For electric field $\vec{E}$, similarly, we can write the wave equation as:

$$\nabla \times \nabla \times \vec{E} - k^2\vec{E} = -j\omega\mu\vec{J}. \tag{B.2b}$$

We can make use of two vector identities:

$$\nabla \times \nabla \times \vec{A} = \nabla\left(\nabla \cdot \vec{A}\right) - \nabla^2\vec{A}, \tag{B.3a}$$

$$\nabla \cdot \left(\nabla \times \vec{A}\right) = 0. \tag{B.3b}$$

Then, (B.2a) can be written as:

$$\nabla\left(\nabla \cdot \vec{H}\right) - \nabla^2\vec{H} - k^2\vec{H} = \nabla \times \vec{J}. \tag{B.4}$$

Using (B.1c), we can write the Helmholtz equation for magnetic field $\vec{H}$ as:

$$\nabla^2\vec{H} + k^2\vec{H} = -\nabla \times \vec{J}. \tag{B.5}$$

Then, if we take curl of (B.2a), using (B.3a),we can arrive at:

$$\nabla \times \nabla \times \nabla \times \vec{H} - k^2\left(\nabla \times \vec{H}\right)\nabla\left(\nabla \cdot \left(\nabla \times \vec{H}\right)\right) - \nabla^2\left(\nabla \times \vec{H}\right) - k^2\left(\nabla \times \vec{H}\right) = \nabla \times \nabla \times \vec{J}. \tag{B.6}$$

Then use (B.3b):

$$\nabla^2\left(\nabla\times\vec{H}\right)+k^2\left(\nabla\times\vec{H}\right)=-\nabla\times\nabla\times\vec{J}. \tag{B.7}$$

Replace $\nabla\times\vec{H}$ with (B.1b):

$$\nabla^2\left(j\omega\varepsilon\vec{E}+\vec{J}\right)+k^2\left(j\omega\varepsilon\vec{E}+\vec{J}\right)=-\nabla\times\nabla\times\vec{J}. \tag{B.8}$$

Finally, we can write the Helmholtz equation for electric field $\vec{E}$ as:

$$\nabla^2\left(\vec{E}+\frac{\vec{J}}{j\omega\varepsilon}\right)+k^2\left(\vec{E}+\frac{\vec{J}}{j\omega\varepsilon}\right)=-\frac{\nabla\times\nabla\times\vec{J}}{j\omega\varepsilon}. \tag{B.9}$$

Notice that (B.5) and (B.9) are derived using only equations (B.1) and the vector identities. Consequently, (B.5) and (B.9) are essentially equivalent to the Maxwell equations (B.1), for any $\vec{E}$ and $\vec{H}$ that satisfies radiation conditions [56].

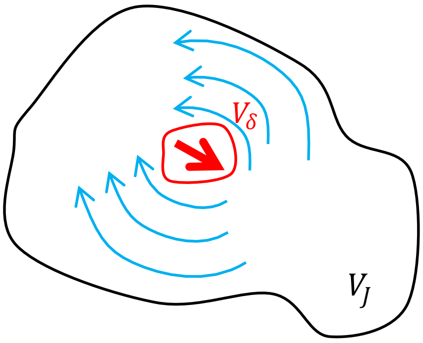

Figure B.1: The arbitrary region V_J where the source is presence and the source region V_δ

The unique solution of (B.9) is given by [44] as:

$$\vec{E}\left(\vec{r}\right)=\frac{j}{\omega\epsilon}\iiint_{V_J-V_\delta}\left[\nabla'\times\nabla'\times\vec{J}\left(\vec{r}'\right)\right]\frac{e^{-jk|\vec{r}-\vec{r}'|}}{4\pi|\vec{r}-\vec{r}'|}\,d\vec{r}'+\frac{-j\vec{J}\left(\vec{r}\right)}{\omega\varepsilon}, \tag{B.10}$$

where $\frac{e^{-jk|\vec{r}-\vec{r}'|}}{4\pi|\vec{r}-\vec{r}'|}$ is the scalar Green's function, V_J represents the volume in which the source is located, and V_δ represents the volume of the delta function of the source. So $Vol-V_\delta$, called "*principal value*" in [44], excludes the singularity of the Green's function at $\vec{r}=\vec{r}'$. If we introduce a current as:

$$\vec{J}=-j\omega\varepsilon\vec{E}, \tag{B.11}$$

we can then substitute it in to (B.9). We can write that:

$$\nabla^2\left(\vec{E}-\vec{E}\right)+k^2\left(\vec{E}-\vec{E}\right)=0=-\frac{\nabla\times\nabla\times\vec{J}}{j\omega\varepsilon}. \tag{B.12}$$

Consequently, we have:

$$\nabla\times\nabla\times\vec{J}=0. \tag{B.13}$$

Using (B.13), (B.10) is reduced to the term only proportional to the current itself:

$$\vec{E}\left(\vec{r}\right)=\frac{-j\vec{J}\left(\vec{r}\right)}{\omega\varepsilon}, \tag{B.14}$$

Replace ε by the definition in (3.8). After some algebraic steps, we can arrive at:

$$\vec{J}(\vec{r}) = \left(\sigma(\omega) + j\omega\varepsilon_0\varepsilon_{r\infty}\right)\vec{E}(\vec{r}), \tag{B.15}$$

which is the eigen-current given in (4.5). If we replace $\vec{J}(\vec{r})$ in (B.14) by (B.15), and equate (B.14) to (4.4), we can prove that:

$$\iiint_{-\infty}^{\infty} \bar{\bar{g}}^{ej}\left(\vec{r},\vec{r}'\right)\cdot\vec{E}\left(\vec{r}'\right)d\vec{r}' = \frac{\vec{E}(\vec{r})}{\left(\sigma + j\omega\varepsilon_0\varepsilon_{r\infty}\right)}. \tag{B.16}$$

C

Another Approximation for pol^2_{real}

As defined in (5.24):

$$pol^2_{real}(k_r) = \left(\bar{\bar{I}} - \frac{k_r^{2*}}{k^{2*}}\hat{k}\hat{k}\right) \cdot \hat{p} \left(\bar{\bar{I}} - \frac{k_r^2}{k^2}\hat{k}\hat{k}\right) \cdot \hat{q}. \tag{C.1}$$

One approximation is $k^2 \approx k_r^2$, thus $k^{2*} \approx k_r^*$. In this case, considering the most coupled case in which the two dipoles are polarized at the same direction, thus $\hat{p} = \hat{q}$, (C.1) is reduced to:

$$pol^2_{real} \approx pol^2_{fake} = \left(\bar{\bar{I}} - \hat{k}\hat{k}\right) \cdot \hat{p} \left(\bar{\bar{I}} - \hat{k}\hat{k}\right) \cdot \hat{p}. \tag{C.2}$$

Replace pol^2_{real} with pol^2_{fake} in (5.29), then the 3D integral can then be performed numerically.

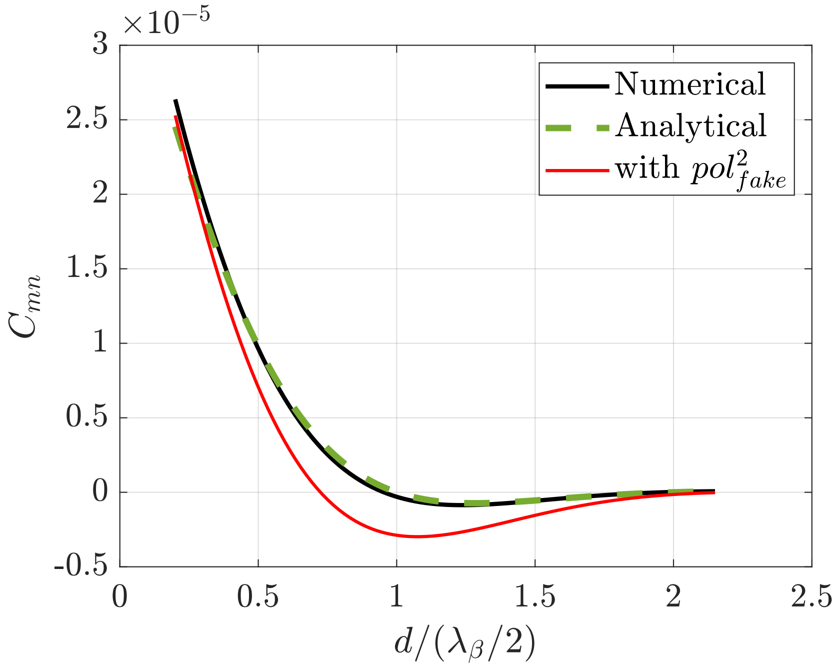

Figure C.1: Coupling coefficient with pol^2_{fake}

Figure C.1 shows the comparison between numerical results, analytical results of (5.49), which adopts the approximation of $pol_{real}^2 \approx 1/\sqrt{\pi}$, and the result with $pol_{real}^2 \approx pol_{fake}^2$. It is clear that pol_{fake}^2 proves to be a worse approximation than $pol_{real}^2 \approx 1/\sqrt{\pi}$.

D

Poynting Vectors of Directional and Isotropic Current Sources

The Poynting vectors of a directional current source and an isotropic current source are derived in this appendix, proving that the current of the isotropic dipoles should be set as $|I_{iso}|^2 = \frac{2}{3}\left|I_0\right|^2$ in order to get the same power as the directional sources.

Similar to (4.3), the electric and magnetic field of a $\hat{z}$ oriented volumetric generating electric current placed at the origin are:

$$\vec{E}(\vec{r}) = j\zeta\frac{k^2 I_0 \Delta \sin\theta}{4\pi}e^{-jkr}\left[\frac{1}{kr}+\frac{1}{j(kr)^2}-\frac{1}{(kr)^3}\right]\hat{\boldsymbol{\theta}} + \zeta\frac{I_0\Delta\cos\theta}{2\pi}e^{-jkr}\left(\frac{1}{(kr)^2}-\frac{j}{(kr)^3}\right)\hat{\boldsymbol{r}}, \tag{D.1a}$$

$$\vec{H}(\vec{r}) = k^2\frac{I_0\Delta\sin\theta}{4\pi}e^{-jkr}\left[j\frac{1}{kr}+\frac{1}{(kr)^2}\right]\hat{\boldsymbol{\varphi}}. \tag{D.1b}$$

The reactive part of the field can be ignored. Since we are interested in the propagating part of the power, we can focus on the visible part of the field as:

$$\vec{E}_{vis}(\vec{r}) = e_\theta\hat{\boldsymbol{\theta}} = j\zeta\frac{kI_0\Delta\sin\theta}{4\pi r}e^{-jkr}\,\hat{\boldsymbol{\theta}}, \tag{D.2a}$$

$$\vec{H}_{vis}(\vec{r}) = e_\varphi\hat{\boldsymbol{\varphi}} = j\frac{kI_0\Delta\sin\theta}{4\pi r}e^{-jkr}\,\hat{\boldsymbol{\varphi}}. \tag{D.2b}$$

Then, the Poynting vector of the source can be expressed as:

$$\begin{aligned}\vec{S} = \vec{E}\times\vec{H}^* = E_\theta H_\varphi^*\hat{\boldsymbol{r}} &= j\zeta\frac{kI_0\Delta sin\theta}{4\pi r}e^{-jkr}\left(\frac{jkI_0\Delta\sin\theta}{4\pi r}e^{-jkr}\right)^*\hat{\boldsymbol{r}}\\ &= j\zeta\frac{kI_0\Delta sin\theta}{4\pi r}e^{-jkr}\frac{-jk^*I_0^*\Delta\sin\theta}{4\pi r}e^{jk^*r}\hat{\boldsymbol{r}}\\ &= \zeta I_0I_0^*\Delta^2kk^*\sin^2\theta\frac{e^{-jkr}e^{jk^*r}}{16\pi^2r^2}\hat{\boldsymbol{r}}.\end{aligned} \tag{D.3}$$

Acknowledging that $I_0I_0^* = |I_0|^2$, $kk^* = |k|^2$ and $e^{-jkr}e^{jk^*r} = e^{-2k_\alpha r}$, (D.3) can be written as:

$$\vec{S} = |kI_0|^2\zeta\frac{\Delta^2\sin^2\theta}{16\pi^2r^2}e^{-2k_\alpha r}\hat{\boldsymbol{r}}. \tag{D.4}$$

Substitute the following expressions for impedance and propagation constant in the medium:

$$\zeta = \frac{\zeta_0}{\sqrt{\varepsilon_{r,eff}}} = \frac{\zeta_d}{\sqrt{1-\frac{j\sigma}{\omega\varepsilon_d}}}, \tag{D.5a}$$

$$|k|^2 = kk^* = k_0^2\sqrt{\varepsilon_{r,eff}}\sqrt{\varepsilon_{r,eff}}^* = k_d^2\sqrt{1-\frac{j\sigma}{\omega\varepsilon_d}}\sqrt{1-\frac{j\sigma}{\omega\varepsilon_d}}^* . \tag{D.5b}$$

Then, the Poynting vector can be expressed as:

$$\begin{aligned}\vec{S} &= |I_0|^2\frac{\zeta_0}{\sqrt{\varepsilon_{r,eff}}}\Delta^2\frac{4\pi^2}{\lambda_0^2}\sqrt{\varepsilon_{r,eff}}\sqrt{\varepsilon_{r,eff}}^*\frac{\sin^2\theta}{16\pi^2 r^2}e^{-2k_\alpha r}\hat{\boldsymbol{r}}\\ &= \frac{|I_0|^2\Delta^2\zeta_0}{\lambda_0^2}\sqrt{\varepsilon_{r,eff}}^*\frac{\sin^2\theta}{4r^2}e^{-2k_\alpha r}\hat{\boldsymbol{r}}.\end{aligned} \tag{D.6}$$

Calculate the spectral power radiating over a sphere with radius r, where r is very large in terms of wavelength:

$$P_0(f) = \iint_{4\pi}\frac{|I_0|^2\Delta^2\zeta_0}{\lambda_0^2}\sqrt{\varepsilon_{r,eff}}^*\frac{\sin^2\theta}{4r^2}e^{-2k_\alpha r}\hat{r}\cdot\hat{r}\ r^2\sin\theta d\theta d\phi. \tag{D.7}$$

The integral in (D.7) can be closed respectively as:

$$\int_0^{2\pi} d\phi = 2\pi, \tag{D.8a}$$

$$\int_0^{\pi}\sin^3\theta d\theta = \left(\frac{1}{3}\cos^3\theta - \cos\theta\right)|_0^{\pi} = \frac{4}{3}. \tag{D.8b}$$

Then, the integral can be closed as:

$$P_0(f) = \frac{2|I_0|^2\Delta^2\zeta_0\pi}{3\lambda_0^2}\sqrt{\varepsilon_{r,eff}}^*e^{-2k_\alpha r}. \tag{D.9}$$

Consider an isotropic current source whose field does not have angular dependence. The electric and magnetic field of the source can be represented as:

$$E_{vis}^{iso}(r) = E_\theta^{iso}\hat{\boldsymbol{\theta}} = j\zeta\frac{kI_{iso}\Delta}{4\pi r}e^{-jkr}\ \hat{\boldsymbol{\theta}}, \tag{D.10a}$$

$$H_{vis}^{iso}(r) = H_\varphi^{iso}\hat{\boldsymbol{\varphi}} = j\frac{kI_{iso}\Delta}{4\pi r}e^{-jkr}\ \hat{\boldsymbol{\varphi}}\ . \tag{D.10b}$$

Then, the Poynting vector of this source can be expressed as:

$$\begin{aligned}\vec{S}^{iso} = \vec{E}^{iso}\times\vec{H}^{iso*} = E_\theta^{iso}H_\varphi^{iso*}\hat{\boldsymbol{r}} &= j\zeta\frac{kI_{iso}\Delta}{4\pi r}e^{-jkr}\left(j\frac{kI_{iso}\Delta}{4\pi r}e^{-jkr}\right)^*\hat{\boldsymbol{r}}\\ &= j\zeta\frac{kI_{iso}\Delta}{4\pi r}e^{-jkr}\frac{-jk^*I_{iso}^*\Delta}{4\pi r}e^{jk^*r}\hat{\boldsymbol{r}}\\ &= \zeta|I_{iso}|^2|k|^2\Delta^2\frac{e^{-2k_\alpha r}}{16\pi^2 r^2}\hat{\boldsymbol{r}}\\ &= \frac{|I_{iso}|^2\Delta^2\zeta_0}{\lambda_0^2}\sqrt{\varepsilon_{r,eff}}^*\frac{e^{-2k_\alpha r}}{4r^2}\hat{\boldsymbol{r}}.\end{aligned} \tag{D.11}$$

Same as before, we can calculate the power radiating over a sphere with radius r:

$$P_{iso}(f) = \iint_{4\pi} \frac{|I_{iso}|^2 \Delta^2 \zeta_0}{\lambda_0^2} \sqrt{\varepsilon_{r,eff}}^* \frac{e^{-2k_\alpha r}}{4r^2} \hat{r}\cdot\hat{r}\ r^2 \sin\theta d\theta d\phi. \tag{D.12}$$

The integral in ϕ is the same as (D.8). The integral in θ can be closed as:

$$\int_0^\pi \sin\theta d\theta = -\cos\theta|_0^\pi = 2. \tag{D.13}$$

The integral can be closed as:

$$P_{iso}(f) = \frac{|I_{iso}|^2 \Delta^2 \zeta_0 \pi}{\lambda_0^2} \sqrt{\varepsilon_{r,eff}}^* e^{-2k_\alpha r}. \tag{D.14}$$

If we would like the isotropic source to radiate the same power as the normal directional dipole, we can equate the right-hand side of both (D.9) and (D.14):

$$\frac{|I_{iso}|^2 \Delta^2 \zeta_0 \pi}{\lambda_0^2} \sqrt{\varepsilon_{r,eff}}^* e^{-2k_\alpha r} = \frac{2|I_0|^2 \Delta^2 \zeta_0 \pi}{3\lambda_0^2} \sqrt{\varepsilon_{r,eff}}^* e^{-2k_\alpha r}. \tag{D.15}$$

After a few simple algebraic steps, we can have:

$$|I_{iso}|^2 = \frac{2}{3} |I_0|^2. \tag{D.16}$$

E

Material Characterization using THz-TDS

TERA K15 from Menlo System [49] is shown in Figure E.1. The system consists of two Photoconductive antennas (PCA) and four plano-convex lenses. The two PCA are coupled via the quasi-optical paths as shown in Figure E.2.

The sample under test (SUT) is placed in the centre as shown in the figure. In order to extract the characteristics of SUT, two measurements, one without SUT and one with SUT, should be done. From these two measurements, we are able to extract the complex permittivity of the sample material at high frequencies. The received time domain signal can be transformed into frequency domain signal using Fourier Transform, resulting in $\tilde{S}_r(f)$ for measurement without SUT and $\tilde{S}_s\left(f\right)$ for measurement with SUT. The transmission coefficient T of the SUT can then be represented with a magnitude term $\rho\left(\omega\right)$ and a phase term $\phi\left(\omega\right)$ as:

$$T = \frac{\tilde{S}_s\left(f\right)}{\tilde{S}_r\left(f\right)} = \rho\left(f\right) \cdot e^{-j\phi(f)}. \tag{E.1}$$

Using the transmission line model analysed in Appendix F, we are able to fit our measured transmission data with the Drude model to determine the exact parameters of the material (e.g. the density of electrons n and scattering time τ).

The relative permittivity saturation $\varepsilon_{r,\infty}$ of Drude model can be extracted from the measured transmission data. Some optical parameters can be easily derived using the repre-

Figure E.1: TERA K15 from Menlo System.

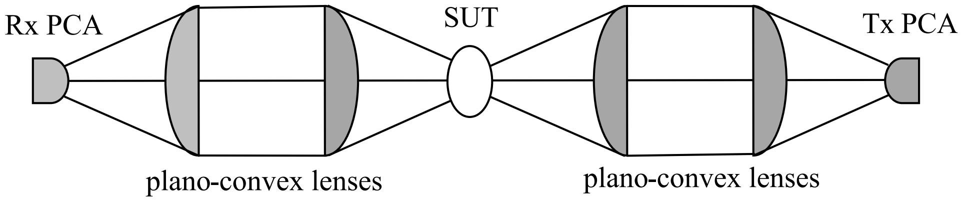

Figure E.2: Geometry of the Lens.

sentation of (E.1) [57], [58]. The complex refractive index can be represented as:

$$\tilde{n}\left(f\right) = n\left(f\right) - i\kappa(f), \tag{E.2}$$

where the real refractive index $n\left(f\right)$ can be derived from the phase alterations induced by the SUT:

$$n\left(f\right) = \phi\left(f\right)\frac{c_0}{2\pi f d} + 1, \tag{E.3}$$

where d is the thickness of the SUT, and c_0 is the speed of propagation in free space. And the imaginary part of the complex refractive index is known as extinction coefficient $\kappa\left(f\right)$, which corresponds to the absorption of the SUT:

$$\kappa\left(f\right) = \frac{c_0}{2\pi f d}\ln\left(\frac{4n\left(f\right)}{\rho\left(f\right)\left(n\left(f\right)+1\right)^2}\right). \tag{E.4}$$

Thus the absorption coefficient can be written as:

$$\alpha\left(f\right) = \frac{4\pi f}{c_0}\kappa\left(f\right). \tag{E.5}$$

Then, the complex permittivity $\varepsilon = \varepsilon' - j\varepsilon''$ can be expressed as:

$$\varepsilon'(f) = n^2\left(f\right) - \kappa^2\left(f\right), \tag{E.6a}$$

$$\varepsilon''(f) = 2n(f)\kappa\left(f\right). \tag{E.6b}$$

Here we can take the saturation of the real part $\varepsilon'(f)$ at high frequencies as $\varepsilon_{r\infty}$ when we fit the measurement data with Drude model.

F

Transmission Line Model of the THz-TDS System

The equivalent transmission line model [59] of the measurement configuration of the THz-TDS system is shown in Figure F.1. The THz pulse is transmitted from the side of medium 1 and received at the side of medium 3. Medium 1 and medium 3 represent the host material of the sample under test (SUT). They are free space in our case. Thus, their impedance and propagation constant are all equal to the free space case:

$$Z_3 = Z_1 = Z_0, \tag{F.1a}$$

$$k_{z1} = k_{z3} = k_0. \tag{F.1b}$$

Medium 2 represents the SUT. The THz beam of incidence can be considered as a plane wave:

$$\vec{E}_t(\vec{r}) = V(z)\,\hat{e}_t. \tag{F.2}$$

The voltage in the transmission line model is expressed as:

$$V_i(z) = V_i^+ e^{-jk_i z} + V_i^- e^{jk_i z}. \tag{F.3}$$

We can obtain the reflection and transmission coefficient by solving the transmission line model. For medium 3 the voltage can be written as:

$$V_3(z) = V_3^+ e^{-jk_0 z}. \tag{F.4}$$

And for medium 2 and 1 as:

$$V_2(z) = V_2^+ e^{-jk_{z2} z} + V_2^- e^{jk_{z2} z}. \tag{F.5}$$

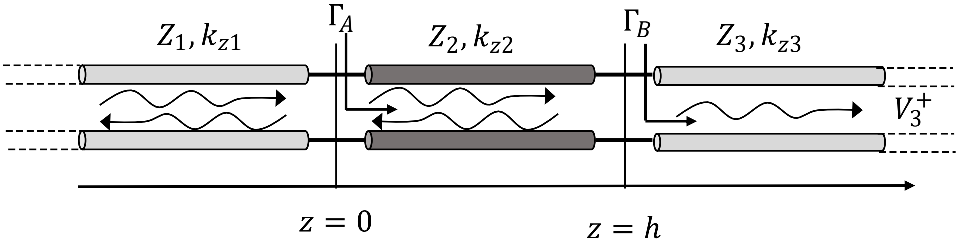

Figure F.1: Transmission line model for the THz-TDS sample measurement.

$$V_1(z) = V_1^+ e^{-jk_0 z} + V_1^- e^{jk_0 z}. \tag{F.6}$$

At $z = d$, the reflection coefficient Γ_B can be represented as:

$$\Gamma_B = \frac{V_2^- e^{jk_{z2}d}}{V_2^+ e^{-jk_{z2}d}} = \frac{Z_0 - Z_2}{Z_0 + Z_2}. \tag{F.7}$$

Then $V_2(z)$ can be represented as:

$$V_2(z) = V_2^+ e^{-jk_{z2}z} + \Gamma_B V_2^+ e^{jk_{z2}(z-2d)}. \tag{F.8}$$

At $z = d$, $V_3(z = d)$ and $V_2(z = d)$ should be the same. In this way, we can have:

$$\frac{V_3(z = d)}{V_2(z = d)} = \frac{V_3^+ e^{-jk_0 d}}{V_2^+ e^{-jk_{z2}d} + \Gamma_B V_2^+ e^{-jk_{z2}d}} = 1. \tag{F.9}$$

After some algebraic steps, we can have:

$$\frac{V_3^+}{V_2^+} = \frac{e^{-jk_{z2}d}(1 + \Gamma_B)}{e^{-jk_0 d}}. \tag{F.10}$$

At $z = 0$, the input impedance Z_{in_A} and reflection coefficient can be represented as:

$$Z_{in_A} = Z_2 \frac{Z_0 + jZ_2 \tan(k_{z2}d)}{Z_2 + jZ_0 \tan(k_{z2}d)}. \tag{F.11}$$

$$\Gamma_A = \frac{V_1^-}{V_1^+} = \frac{Z_2 - Z_{in_A}}{Z_2 + Z_{in_A}}. \tag{F.12}$$

Using the similar procedure as before, $V_1(z)$ can be represented as:

$$V_1(z) = V_1^+ e^{-jk_0 z} + V_1^+ \Gamma_A e^{jk_0 z}. \tag{F.13}$$

At $z = 0$, $V_1(z = 0)$ and $V_2(z = 0)$ should be the same. In this way, we can have:

$$\frac{V_2(z = 0)}{V_1(z = 0)} = \frac{V_2^+ + \Gamma_B V_2^+ e^{-jk_{z2}2d}}{V_1^+(1 + \Gamma_A)} = 1. \tag{F.14}$$

After some algebraic steps, we can have:

$$\frac{V_2^+}{V_1^+} = \frac{(1 + \Gamma_A)}{1 + \Gamma_B e^{-jk_{z2}2d}}. \tag{F.15}$$

Then we can represent the transmission coefficient from medium 1 to 3 as:

$$T = \frac{(1 + \Gamma_B)(1 + \Gamma_A)}{e^{jk_{z2}d} e^{-jk_0 d}(1 + \Gamma_B e^{-jk_{z2}2d})}. \tag{F.16}$$

G

Drawing of a Cavity on Waveguide Short

The drawing of a cavity for silicon samples on the waveguide short is shown in Figure G.3 on the next page. The roundings with a radius of 1 mm are designed for the milling process due to the limitations of the available milling cutter.

A picture of the finished product is shown in Figure G.1. Figure G.2 shows the picture of the product in use.

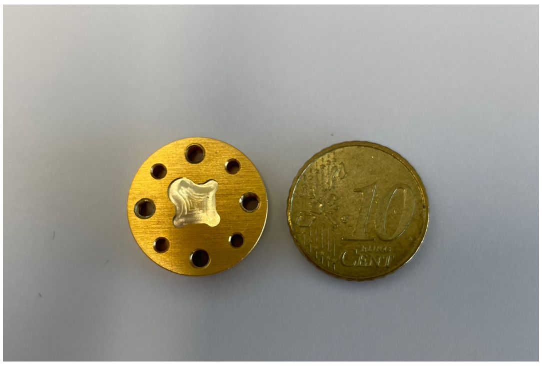

Figure G.1: A picture of the finished product.

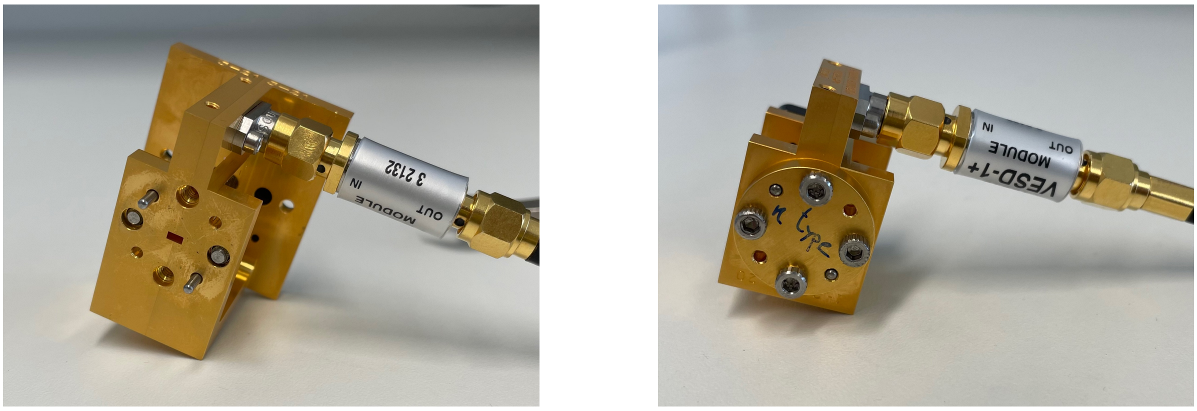

(a) Waveguide port of the detector.

(b) Waveguide short applied on.

Figure G.2: Pictures of the product in use.

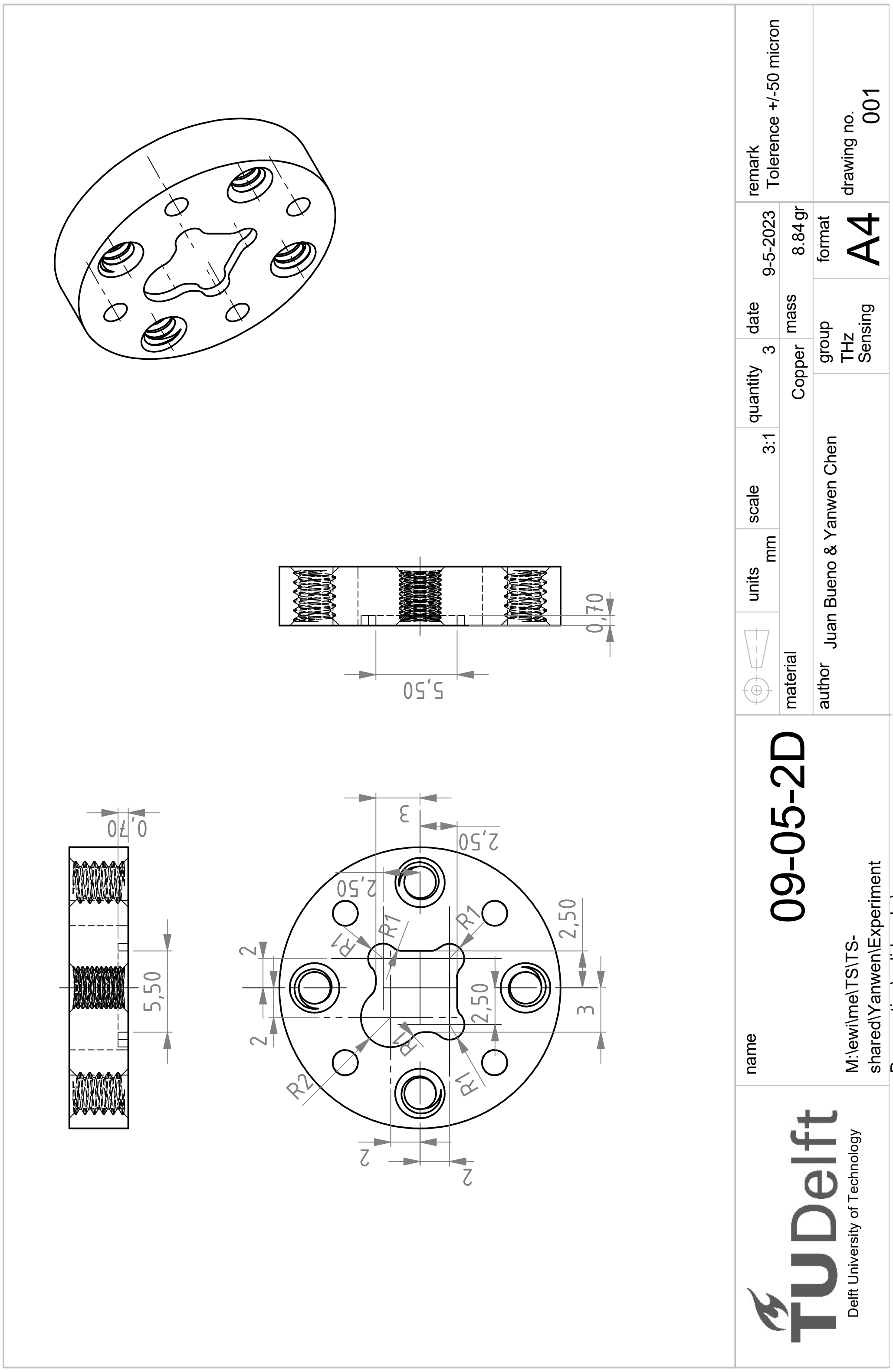

Figure G.3: The drawing of the chamber on waveguide short.

H

A possible Matching Layer Design for Silicon Ingot

Paper [60] presents a Matching Layer (ML) design for silicon lens array at 500 GHz using laser-ablated structures. The design uses a periodic sub-wavelength structure shown in Figure H.1.

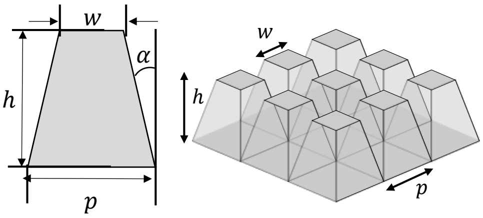

Figure H.1: Schematic of the truncated pyramid ML design.

The design in [60] is then scaled to meet the frequency requirement of the detectors, from 75 to 500 GHz. The design parameters are given in Table H.1. According to [60] the minimum angle α (see Figure H.1) that can be obtained for this truncated pyramid design is 13°. To give some redundancy for the laser ablation process, the angle α is designed as 15°.

Table H.1: Parameters of ML design.

$d(\mu m)$	$p(\mu m)$	$h(\mu m)$	$\alpha(\mu m)$
73	196	231	15

The structure is then simulated in CST for a unit cell of the truncated pyramid structure made of ideal lossless silicon ($\varepsilon_r = 11.7$, due to the limitation of the CST solver) to obtain the effective transmission coefficient between the silicon and free space. The effective transmission coefficient is defined the same as (6.52) by taking an average between TE and TM polarization:

$$T_{eff} = \frac{1}{2}\left(T^{\parallel} + T^{\perp}\right). \tag{H.1}$$

The result is given in Figure H.2. For comparison, the effective transmission coefficient without this ML at broadside is calculated using Fresnel equations (6.50) as $T_{eff}^{w/o} = 0.7 = -3.6$ dB. As we can see from the figure, for the broadside case, the transmission coefficient improves by at least 1.5 dB.

For the case without ML, power fluxes with an angle of incidence larger than the critical angle $\theta_c = 17°$ will not propagate through the dielectric-air surface. The ML allows fluxes with angles of incidence larger than θ_c to propagate through, although there are some glitches for transmission coefficients in higher frequencies. Also, for larger angles of incidence, the transmission coefficient is lower.

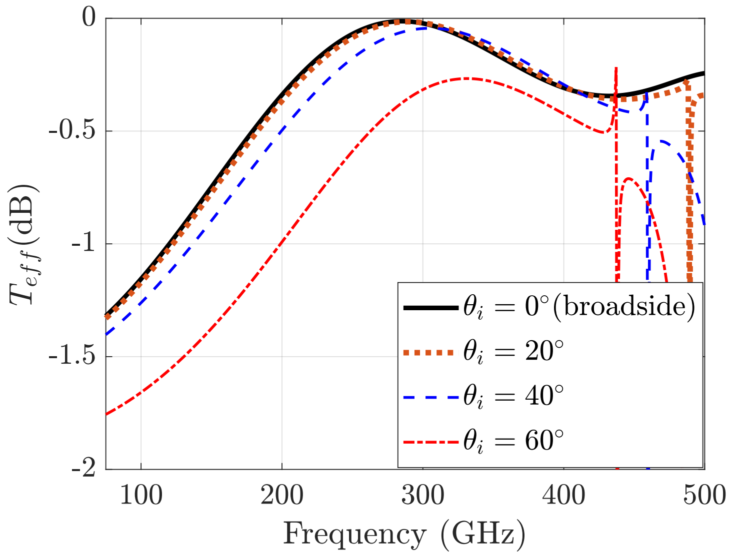

Figure H.2: Effective transmission coefficient for the ML design with different angle of incidence θ_i.

Bibliography

[1] F. Ulaby, R. Moore, and A. Fung, *Microwave Remote Sensing: Active and Passive* (Artech House microwave library). Artech House, 1981, ISBN: 9780890061909.

[2] G. Kirchhoff, "Ueber das verhältniss zwischen dem emissionsvermögen und dem absorptionsvermögen der körper für wärme und licht," *Annalen der Physik*, vol. 185, no. 2, pp. 275–301, 1860.

[3] Rayleigh, "The dynamical theory of gases and of radiation," *Nature*, pp. 54–55, 1905.

[4] J. H. Jeans, "The dynamical theory of gases and of radiation," *Nature*, vol. 72, pp. 1476–4687, 1905.

[5] M. Planck, *The theory of heat radiation.* Blakiston, 1914.

[6] A. Einstein, "Über einen die Erzeugung und Verwandlung des Lichtes betreffenden heuristischen Gesichttspunkt," *Annalen der Physik*, 1905.

[7] J. B. Johnson, "Thermal agitation of electricity in conductors," *Phys. Rev.*, vol. 32, pp. 97–109, 1928.

[8] H. Nyquist, "Thermal agitation of electric charge in conductors," *Phys. Rev.*, vol. 32, pp. 110–113, 1928.

[9] S. M. Rytov, *Theory of electric fluctuations and thermal radiation.* Moscow: USSR Academy of Science, 1953.

[10] S. M. Rytov, Y. A. Kravtsov, and V. I. Tatarskii, *Principles of Statistical Radiophysics 3: Elements of Random Fields.* Berlin: Springer Berlin, Heidelberg, 1989.

[11] L. Crovini and L. Galgani, "On the accuracy of the experimental proof of planck's radiation law," *Lettere Al Nuovo Cimento Series 2*, vol. 39, no. 10, pp. 210–214, Mar. 1984.

[12] A. G. Polimeridis, M. T. H. Reid, W. Jin, S. G. Johnson, J. K. White, and A. W. Rodriguez, "Fluctuating volume-current formulation of electromagnetic fluctuations in inhomogeneous media: Incandescence and luminescence in arbitrary geometries," *Phys. Rev. B*, vol. 92, p. 134 202, 13 Oct. 2015.

[13] M. Hoogelander, S. v. Berkel, S. Malotaux, *et al.*, "Chessboard focal plane array for a cmos-integrated terahertz camera," *IEEE Transactions on Terahertz Science and Technology*, pp. 1–13, 2023.

[14] S. van Berkel, E. S. Malotaux, C. De Martino, *et al.*, "Wideband double leaky slot lens antennas in cmos technology at submillimeter wavelengths," *IEEE Transactions on Terahertz Science and Technology*, vol. 10, no. 5, pp. 540–553, 2020.

[15] P. Hillger, J. Grzyb, R. Jain, and U. R. Pfeiffer, "Terahertz imaging and sensing applications with silicon-based technologies," *IEEE Transactions on Terahertz Science and Technology*, vol. 9, no. 1, pp. 1–19, 2019.

[16] J. C. Mather, E. S. Cheng, J. E. R. E., *et al.*, “A preliminary measurement of the cosmic microwave background spectrum by the cosmic background explorer (COBE) satellite,” *The Astrophysical Journal*, vol. 354, p. L37, May 1990.

[17] R. M. van Schelven, A. F. Bernardis, P. Sberna, and A. Neto, “Drude dispersion in the transmission line modeling of bulk absorbers at sub-mm wave frequencies: A tool for absorber optimization,” *IEEE Antennas and Propagation Magazine*, vol. 64, pp. 50–60, 2022.

[18] L. Landau and E. Lifshitz, “Chapter xiii - electromagnetic fluctuations,” in *Electrodynamics of Continuous Media*, ser. Course of Theoretical Physics, 1st ed., vol. 8, Amsterdam: Pergamon, 1960, pp. 360–365.

[19] J.-J. Greffet, P. Bouchon, G. Brucoli, E. Sakat, and F. Marquier, “Generalized kirchhoff law,” *arXiv: Optics*, 2016.

[20] G. Bekefi and S. C. Brown, “Emission of radio-frequency waves from plasmas,” *American Journal of Physics*, vol. 29, pp. 404–428, 1961.

[21] J.-J. Greffet, P. Bouchon, G. Brucoli, and F. Marquier, “Light emission by nonequilibrium bodies: Local kirchhoff law,” *Phys. Rev. X*, vol. 8, p. 021 008, 2 Apr. 2018.

[22] A. Stogryn, “The brightness temperature of a vertically structured medium,” *Radio Science*, vol. 5, no. 12, pp. 1397–1406, 1970.

[23] L. Tsang, E. Njoku, and J. A. Kong, “Microwave thermal emission from a stratified medium with nonuniform temperature distribution,” *Journal of Applied Physics*, vol. 46, no. 12, pp. 5127–5133, Sep. 2008.

[24] J. Geng, “Volumetric method of moments,” Available at `http://resolver.tudelft.nl/uuid:c8e8482c-901b-498d-8d13-15c3c2e7b611`, Master’s thesis, Delft University of Technology, Delft, The Netherlands, Sep. 2022.

[25] R. Ozzola, J. Geng, A. Freni, and A. Neto, “Full-wave solver for radiation from thermal sources,” in *2022 47th International Conference on Infrared, Millimeter and Terahertz Waves (IRMMW-THz)*, 2022, pp. 1–2.

[26] A. Neto, “A classical electromagnetic model for thermal emission from ohmic materials,” in *17th European Conference on Antennas and Propagation*, Florence, Italy, Mar. 2023.

[27] E. Wolf, “Coherence and radiometry,” *J. Opt. Soc. Am.*, vol. 68, no. 1, pp. 6–17, Jan. 1978.

[28] E. Wolf, “New theory of radiative energy transfer in free electromagnetic fields,” *Phys. Rev. D*, vol. 13, pp. 869–886, 4 Feb. 1976.

[29] D. Hill and J. Ladbury, “Spatial-correlation functions of fields and energy density in a reverberation chamber,” *IEEE Transactions on Electromagnetic Compatibility*, vol. 44, no. 1, pp. 95–101, 2002.

[30] D. A. Hill, “Reverberation chambers,” in *Electromagnetic Fields in Cavities: Deterministic and Statistical Theories.* 2009, pp. 91–150.

[31] P. Drude, “Zur elektronentheorie der metalle,” *Annalen der Physik*, vol. 306, pp. 566–613, 1900.

[32] D. M. Pozar, “Electromagnetic theory,” in *Microwave Engineering*, 4th. Hoboken, NJ: John Wiley & Sons, Inc., 2012, pp. 6–11.

[33] M. A. Leontovich, “On the approximate boundary conditions for the electromagnetic field on the surface of well conducting bodies,” *Radio Wave Propagation Studies*, pp. 5–12, 1948.

[34] H. H. Eichhorn, J. C. Mather, and W. L., “Submillimeter and millimeter wave characterization of absorbing materials,” *Appl. Opt.*, vol. 24, pp. 4489–4492, 1985.

[35] K. Champlin and G. Eisenstein, “Cutoff frequency of submillimeter schottky-barrier diodes,” *IEEE Transactions on Microwave Theory and Techniques*, vol. 26, pp. 31–34, 1978.

[36] L. Dickens, “Spreading resistance as a function of frequency,” *IEEE Transactions on Microwave Theory and Techniques*, vol. 15, pp. 101–109, 1967.

[37] M. van Exter and D. Grischkowsky, “Carrier dynamics of electrons and holes in moderately doped silicon,” *Phys. Rev. B*, vol. 41, pp. 12 140–12 149, 1990.

[38] T.-I. Jeon and D. Grischkowsky, “Characterization of optically dense, doped semiconductors by reflection thz time domain spectroscopy,” *Applied Physics Letters*, vol. 72, pp. 3032–3034, 1998.

[39] D. Klaassen, “A unified mobility model for device simulation—i. model equations and concentration dependence,” *Solid-State Electronics*, vol. 35, pp. 953–959, 1992.

[40] J. Weber, “Fluctuation dissipation theorem,” *Phys. Rev.*, vol. 101, pp. 1620–1626, 6 Mar. 1956.

[41] A. Neto, “A classical description of the electromagnetic energy available due to thermal agitation in ohmic media,” Manuscript submitted for publication, 2023.

[42] R. F. Harrington, “Spherical wave functions,” in *Time-Harmonic Electromagnetic Fields*. IEEE, 2001, pp. 264–316.

[43] J. A. Stratton, “Spherical waves,” in *Electromagnetic Theory*. IEEE, 2006, pp. 392–423.

[44] A. Yaghjian, “Electric dyadic green’s functions in the source region,” *Proceedings of the IEEE*, vol. 68, pp. 248–263, 1980.

[45] C. Tai, *Dyadic Green Functions in Electromagnetic Theory* (IEEE Press series on electromagnetic waves). IEEE Press, 1994.

[46] M. Abramowitz and I. A. Stegun, *Handbook of Mathematical Functions : with Formulas, Graphs, and Mathematical Tables*. New York: Dover Publications, 1965.

[47] L. B. Felsen and N. Marcuvitz, “Radiation and scattering of waves,” in *Asymptotic Evaluation of Integrals*. IEEE, 1994, pp. 370–441.

[48] *Virginia Diodes, Inc - Detectors*, `https://www.vadiodes.com/en/products/detectors`.

[49] *All fiber-coupled Terahertz Spectrometer | Menlo Systems*, `https://www.menlosystems.com/products/thz-time-domain-solutions/terak15-terahertz-spectrometer/`.

[50] J. L. Hesler and T. W. Crowe, “Responsivity and noise measurements of zero-bias schottky diode detectors,” *Proc. ISSTT*, pp. 89–92, 2007.

[51] P. Griffiths and J. M. Chalmers, "Theory and instrumentation," in *Handbook of vibrational spectroscopy*. Wiley, 2006.

[52] I. Virginia Diodes, *Zero-Bias Detector Operational Manual*. [Online]. Available: `https://www.vadiodes.com/images/Products/Detectors/VDI-734_ZBD_Product_Manual.pdf`.

[53] F. Microwave. "Wr-10 waveguide short plate with 4mm copper and ug-cover round flange." (2019), [Online]. Available: `https://www.fairviewmicrowave.com/images/productPDF/FMW10SP4.pdf`.

[54] Keysight, *3458a multimeter user's guide*. [Online]. Available: `https://www.keysight.com/us/en/assets/9018-01343/user-manuals/9018-01343.pdf`.

[55] J. H. Lambert, *Photometria sive de mensura et gradibus luminis, colorum et umbrae*. Augsburg: sumptibus vidvae Eberhardi Klet, 1760.

[56] A. D. Yaghjian, *A direct approach to the derivation of electric dyadic green's functions*, 1978.

[57] M. Afsar, "Dielectric measurements of millimeter-wave materials," *IEEE Transactions on Microwave Theory and Techniques*, vol. 32, no. 12, pp. 1598–1609, 1984.

[58] Y.-S. Jin, G.-J. Kim, and S.-G. Jeon, "Terahertz dielectric properties of polymers," *Journal of the Korean Physical Society*, vol. 49, no. 2, p. 513, 2006.

[59] A. Fiorellini Bernardis, "On the modelling and characterisation of photoconducting antennas," Available at `https://doi.org/10.4233/uuid:469e35d4-7aa8-4301-94a0-17baceb3af1c`, Doctoral thesis, Delft University of Technology, Delft, The Netherlands, May 2022.

[60] J. Bueno, S. Bosma, T. Bußkamp-Alda, M. Alonso-delPino, and N. Llombart, "Lossless matching layer for silicon lens arrays at 500 ghz using laser ablated structures," *IEEE Transactions on Terahertz Science and Technology*, vol. 12, no. 6, pp. 667–672, 2022.